Enhanced electroweak radiative corrections in SUSY: gluon-free observables

I. V. Gaidaenko, A. V. Novikov, and V. A. Novikov
Institute of Theoretical and Experimental Physics, 117259 Moscow, Russia

A. N. Rozanov
Institute of Theoretical and Experimental Physics, 117259 Moscow, Russia; CPPM, IN2P3, CNRS, 13288 Marseille, France

M. I. Vysotsky
Institute of Theoretical and Experimental Physics, 117259 Moscow, Russia; INFN, 4410 Sezione di Ferrara, Italy

(21 April 1998)
Pis'ma Zh. Éksp. Teor. Fiz. **67**, No. 10, 723–726 (25 May 1998)

The large top-quark mass is responsible for the enhancement of the oblique radiative corrections in SUSY models. We present analytical formulas for these corrections to the W-boson mass m_W and to the $Z l^+ l^-$-coupling constants. A comparison with the result of the standard model fit is made. © *1998 American Institute of Physics.* [S0021-3640(98)00110-8]

PACS numbers: 12.60.Jv, 12.15.Lk, 14.65.Ha, 14.70.Fm

Precision measurements of the Z-boson parameters, W-boson mass, and top-quark mass have demonstrated that the standard model perfectly describes this part of physics.[1] There is no hope of improving the standard model fit by introducing new physics, since it is already perfect. For the data set announced at the HEP97 Conference we obtained $\chi^2/d.o.f. = 18/14$ (Ref. 2).

Nevertheless, people still believe that there should be physics beyond the standard model, and the most popular candidate is supersymmetry. In SUSY models there is a natural reason for the success of the standard model in describing the data at energy scales of the order of the intermediate boson masses. This reason is decoupling: the contribution of SUSY particles to the ''low energy'' observables is suppressed by a factor of $(m_{W,Z}/m_{\mathrm{SUSY}})^2$. That is why a comparison of the results of the SUSY model calculations with experimental data gives the lower bounds on superpartner masses. To perform such a program the one-loop electroweak radiative corrections in the SUSY models should be calculated, and this has been done (see, e.g., Refs. 3–5). However, since there are a lot of one-loop diagrams and a large number of parameters even in the simplest MSSM, a qualitative picture of the electroweak radiative corrections did not emerge. The aim of our investigation is twofold. First, we will present simple analytical formulas which describe the main part of the radiative corrections in a wide class of SUSY models; second, we will include SUSY particles in the description of the electroweak radiative corrections developed and reviewed in Ref. 6.

In the present paper we will deal with observables which are less sensitive to the strong interactions, i.e., with the mass of the W boson and with the $Z\,l^+l^-$-coupling constants g_A and g_V. In the future we plan to incorporate Z-boson decays to hadrons, which will enable us to perform a general fit of the data and to get lower bounds on the masses of superpartners.

In order to calculate the radiative corrections to m_W, g_A and g_V one starts with the corrections to G_μ, m_Z, and $\overline{\alpha}\equiv\alpha(m_Z)$. The corrections to G_μ are described in SUSY theories by box and vertex diagrams and by a correction to the W-boson propagator. The corrections to m_Z and $\overline{\alpha}$ are described by self-energy insertions. Having calculated all the terms one comes to the corrections to m_W, g_A, and g_V. The corrections to m_W contain self-energy insertions, and the corrections to the coupling constants contain the vertices as well. In general all the above corrections are of order $(m_{W,Z}/m_{\rm SUSY})^2$ and there are a lot of contributions from a large number of diagrams. However, the breaking of $SU(2)_V$ symmetry by the large top-quark mass penetrates into the SUSY sector of the theory and leads to huge enhancement of the corresponding oblique corrections for any value of $m_{\rm SUSY}$. To begin with, let us neglect $\tilde{t}_L\tilde{t}_R$ mixing. In this case we have to good accuracy: $m^2_{\tilde{t}_L}-m^2_{\tilde{b}_L}=m_t^2$ (in what follows we will often designate $\tilde{b}_L$ as $\tilde{b}$). For $(\tilde{t}_L,\tilde{b}_L)$ loop insertion into the W-boson propagator we get a result proportional to $(m^2_{\tilde{t}_L}-m^2_{\tilde{b}_L})^2/m_W^2m^2_{\rm SUSY}\approx 16(m_W/m_{\rm SUSY})^2$, since $m_t\approx 2m_W$. That is why the $(\tilde{t},\tilde{b})$ oblique corrections are responsible for the main part of SUSY corrections to gluon-free observables. (We note that the existence of terms $\sim(m_t)^4$ in the SUSY radiative corrections was observed long ago.[7] Now that we know that the top quark is very heavy and that it follows from the direct searches that most of the SUSY partners should be much heavier than $M_Z/2$, we can claim that the stop–sbottom contribution to the oblique corrections dominates over the other SUSY contributions to the gluon-free observables.) The term $\sim m_t^4/m_W^2m^2_{\rm SUSY}$ comes from $\Sigma_W(0)$, while the terms proportional to $\Sigma'(0)$ produce corrections of order $m_t^2/m^2_{\rm SUSY}$. Higher-order derivatives of the self-energies are suppressed by a factor of $(m_{W,Z}/m_{\rm SUSY})^2$ and should be omitted. Calculating the vector boson self-energies and keeping the first two terms in the k^2 expansion, we get the following expressions for the SUSY contributions to the quantities V_i, which are directly related to the physical observables (V_m to m_W, V_A to g_A and V_R to the ratio g_V/g_A; see Ref. 6):

$$\delta_{\rm SUSY}V_A=\frac{1}{m_Z^2}g(m_{\tilde{t}_L},m_{\tilde{b}}), \tag{1}$$

$$\delta_{\rm SUSY}V_R=\delta_{\rm SUSY}V_A+\frac{1}{3}Y_L\,\ln\left(\frac{m^2_{\tilde{t}_L}}{m^2_{\tilde{b}}}\right), \tag{2}$$

$$\delta_{\rm SUSY}V_m=\delta_{\rm SUSY}V_A+\frac{2}{3}Y_Ls^2\,\ln\left(\frac{m^2_{\tilde{t}_L}}{m^2_{\tilde{b}}}\right)+\left(\frac{c^2-s^2}{3}\right)h(m_{\tilde{t}_L},m_{\tilde{b}}), \tag{3}$$

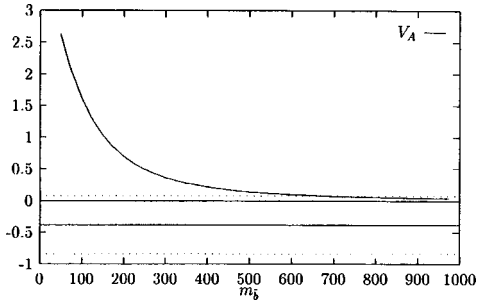

FIG. 1. The dependence of the function $\delta_{\rm SUSY}V_A$ on $m_{\tilde{b}}$. The horizontal lines show the difference between the experimental value of V_A and its fit in the standard model, $V_A^{\rm exp}-V_A^{\rm theor}=-0.38(46)$. The solid line corresponds to the central value, while the dotted lines show a one standard deviation corridor.

where Y_L is the left doublet hypercharge, $Y_L=Q_t+Q_b$, $s\equiv\sin\theta$, $c\equiv\cos\theta$, $\sin^2\theta\cos^2\theta=\pi\overline{\alpha}(m_Z)/(\sqrt{2}G_\mu m_Z^2)$ (θ is the electroweak mixing angle), and the functions g and h are standard functions which describe the scalar particle contributions to the vector boson self-energies at one loop:

$$g(m_1,m_2)=m_1^2+m_2^2-2\frac{m_1^2m_2^2}{m_1^2-m_2^2}\ln\left(\frac{m_1^2}{m_2^2}\right), \tag{4}$$

$$h(m_1,m_2)=-\frac{5}{3}+\frac{4m_1^2m_2^2}{(m_1^2-m_2^2)^2}+\frac{(m_1^2+m_2^2)(m_1^4-4m_1^2m_2^2+m_2^4)}{(m_1^2-m_2^2)^3}\ln\left(\frac{m_1^2}{m_2^2}\right). \tag{5}$$

For SUSY partners with masses larger than m_t, $m_{\tilde{b}}\gg m_t$, the leading term in (1)–(5) is universal; it originates from $\Sigma_W(0)$ and is given by the function g:

$$\delta_{\rm SUSY}V_i=\frac{1}{3}\,\frac{(m_{\tilde{t}_L}^2-m_{\tilde{b}}^2)^2}{m_Z^2m_{\tilde{b}}^2}. \tag{6}$$

For light SUSY partners $m_{\tilde{b}}\sim m_t$ we should not expand $\delta_{\rm SUSY}V_i$ in powers of $(m_{\tilde{t}_L}^2-m_{\tilde{b}}^2)/m_{\tilde{b}}^2$ but use expressions (1)–(5) to describe the electroweak corrections. In Figs. 1, 2, and 3 the dependences of the functions $\delta_{\rm SUSY}V_i$ on $m_{\tilde{b}}$ are shown. For the top-quark mass we use $m_t=175$ GeV. The horizontal lines show the difference of the experimental values of V_i and their standard model fit. The solid lines correspond to the central values while the dotted ones correspond to the one standard deviation corridor. We see from the figures that for $m_{\tilde{b}}\geqslant 200$ GeV the SUSY corrections are not essential, and the inclusion of SUSY partners will not spoil the standard model fit of the data.

Now let us take into account the $\tilde{t}_L\tilde{t}_R$ mixing, which in general is not small, being of the order of the t-quark mass times the superpartner mass scale, $m_{LR}^2\sim m_t m_{\rm SUSY}$. As a result of mixing, two states with masses m_1 and m_2 are formed, $\tilde{t}_1=c_u\tilde{t}_L+s_u\tilde{t}_R$ and $\tilde{t}_2=-s_u\tilde{t}_L+c_u\tilde{t}_R$, where $c_u\equiv\cos\theta_{LR}$, $s_u\equiv\sin\theta_{LR}$, and our functions $\delta_{\rm SUSY}^{LR}V_i$ depend on 4 parameters: m_1, m_2, θ_{LR}, and $m_{\tilde{b}}$, three of which are independent (the difference of

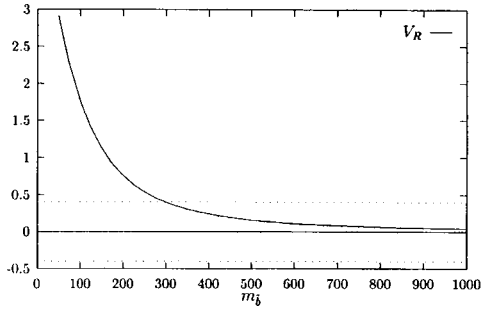

FIG. 2. The same as Fig. 1 for V_R. A difference $V_R^{\rm exp}-V_R^{\rm theor}=-0.0(4)$ was used.

$m^2_{\tilde{t}_L\tilde{t}_L}$ and $m^2_{\tilde{b}_L\tilde{b}_L}$ is determined by the top-quark mass). The numerical values of these parameters depend on the SUSY model. Let us present the formulas for the electroweak radiative corrections which take $\tilde{t}_L\tilde{t}_R$ mixing into account:

$$\delta^{LR}_{\rm SUSY}V_A=\frac{1}{m_Z^2}[c_u^2 g(m_1,m_{\tilde{b}})+s_u^2 g(m_2,m_{\tilde{b}})-c_u^2 s_u^2 g(m_1,m_2)], \tag{7}$$

$$\delta^{LR}_{\rm SUSY}V_R=\delta^{LR}_{\rm SUSY}V_A+\frac{1}{3}Y_L\left[c_u^2\ln\left(\frac{m_1^2}{m_{\tilde{b}}^2}\right)+s_u^2\ln\left(\frac{m_2^2}{m_{\tilde{b}}^2}\right)\right]-\frac{1}{3}c_u^2 s_u^2 h(m_1,m_2), \tag{8}$$

$$\delta^{LR}_{\rm SUSY}V_m=\delta^{LR}_{\rm SUSY}V_A+\frac{2}{3}Y_L s^2\left[c_u^2\ln\left(\frac{m_1^2}{m_{\tilde{b}}^2}\right)+s_u^2\ln\left(\frac{m_2^2}{m_{\tilde{b}}^2}\right)\right]+\frac{c^2-s^2}{3}[c_u^2 h(m_1,m_{\tilde{b}})$$
$$+s_u^2 h(m_2,m_{\tilde{b}})]-\frac{c_u^2 s_u^2}{3}h(m_1,m_2). \tag{9}$$

Our approximation should be good for the case when all superpartners have more or less equal masses. When some spartners are considerably lighter than sbottom, their contribution can dominate and our approximation can fail.

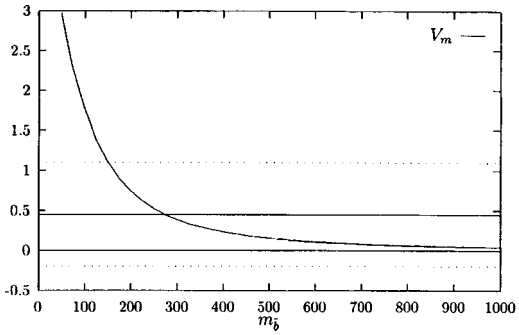

FIG. 3. The same as Fig. 1 for V_M. A difference $V_m^{\rm exp}-V_m^{\rm theor}=0.45(65)$ was used.

It is desirable to compare numerically the formulas for the enhanced radiative corrections with the results of full one loop calculations in SUSY models in order to check how good our approximation is.

We are grateful to Z. Berezhiani for discussions on SUSY models. The research of I. G., A. N., V. N., and M. V. was supported by RFBR Grants 96-02-18010 and 96-15-96578, and that of A. N., V. N., and M. V. by INTAS Grants 93-3316 and 94-2352 and by INTAS-RFBR Grant 95-05678. V. A. Novikov is grateful to G. Fiorentini and L. Piemontese for hospitality in Ferrara, where this work was completed.

[1] J. Timmermans, in *Proceedings of LP 97*, Hamburg (1997); D. Ward, in *Proceedings of HEP 97*, Jerusalem (1997); G. Quast, *ibid.*
[2] M. I. Vysotsky, V. A. Novikov, L. B. Okun and A. N. Rozanov, ''Standard Model and the progress of LEP I'' [in Russian], submitted to Yad. Fiz.
[3] P. Chankowski, A. Dabelstein, W. Hollik *et al.*, Nucl. Phys. B **417**, 101 (1994).
[4] D. Garcia, R. J. Jimenez and J. Sola, Phys. Lett. B **347**, 309, 321 (1995).
[5] W. de Boer, A. Dabelstein, W. Hollik *et al.*, Z. Phys. C **75**, 627 (1997).
[6] V. A. Novikov, L. B. Okun, and M. I. Vysotsky, Nucl. Phys. B **397**, 35 (1993); V. Novikov, L. Okun, A. Rozanov, and M. Vysotsky, LEPTOP, preprint ITEP 19-95/CPPM-95-1; Usp. Fiz. Nauk **166**, 539 (1996).
[7] L. Alvarez-Gaume, J. Polchinski and M. Wise, Nucl. Phys. B **211**, 495 (1983); R. Barbieri and L. Maiani, Nucl. Phys. B **224**, 32 (1983).

Published in English in the original Russian journal. Edited by Steve Torstveit.

Phenomenology of $SU(3)\otimes SU(2)\otimes U(1)$ supersymmetric model with Dirac neutrino masses

N. V. Krasnikov[a)]
Institute for Nuclear Research, Russian Academy of Sciences, 117312 Moscow, Russia

(Submitted 23 March 1998)
Pis'ma Zh. Éksp. Teor. Fiz. **67**, No. 10, 727–729 (25 May 1998)

We consider a minimal supersymmetric extension of the standard electroweak model with Dirac neutrino masses. In such a model for a significant region of the parameters the right-handed tau sneutrino is the lightest superparticle and the right-handed charged tau slepton is the next-to-lightest superparticle. Due to the smallness of the neutrino masses the right-handed tau slepton is a long-lived particle that alters the standard signatures used in the search for supersymmetry at supercolliders. The most striking signatures of such a scenario is the existence of highly ionized tracks and an excess of multilepton events that is similar to the phenomenology of gauge-mediated supersymmetry-breaking models. © *1998 American Institute of Physics.*
[S0021-3640(98)00210-2]

PACS numbers: 12.60.Jv, 14.60.Pq

Supersymmetric electroweak models offer the simplest solution of the gauge hierarchy problem.[1–4] In real life supersymmetry has to be broken, and the masses of the superparticles have to be lighter than $O(1)$ TeV, provided that the supersymmetry solves the gauge hierarchy problem.[4] Supergravity gives a natural explanation for the supersymmetry breaking, namely, taking the supergravity breaking into account in the hidden sector leads to soft supersymmetry-breaking in the observable sector.[4] For the supersymmetric extension of the Weinberg–Salam model, soft supersymmetry breaking terms usually consist of the gaugino mass terms, squark and slepton mass terms with the same mass at the Planck scale, and trilinear soft scalar terms proportional to the superpotential. Another standard assumption is that the ''minimal supersymmetric standard model'' (MSSM) conserves R-parity. As a consequence of R-parity conservation, supersymmetric particles can only be produced in pairs and supersymmetric particles can't decay into ordinary particles, so the lightest superparticle (LSP) is stable. The typical SUSY signature for supercolliders involves missing E_T transverse energy as a sign of SUSY particle production.[5]

In this paper we consider a supersymmetric extension of the Weinberg–Salam model with nonzero Dirac neutrino masses (the MSSM model with Dirac neutrino masses). We show that in such a model for a significant range of the parameters the right-handed sneutrino is the LSP and the charged right-handed tau slepton is the next-to-lightest superparticle. Due to the smallness of the neutrino masses the right-handed tau

slepton is a long-lived particle, and it decays outside the detector, thus drastically altering the standard signatures used in the search for supersymmetry at supercolliders. Namely, the most striking signatures for the SUSY search in the model under discussion include highly ionized tracks from long-lived right-handed tau sleptons and an excess of multimuon signals.[b)]

Consider supersymmetric $SU(3)\otimes SU(2)\otimes U(1)$ model with Dirac neutrino masses. The superpotential of the model has the form

$$W=h_{u_i}Q_iH_1\overline{u_i}+h_{d_i}Q_iH_2\overline{d_i}+h_{\nu_i}L_iH_1\overline{\nu_i}+h_{e_i}L_iH_2\overline{e_i}+\mu H_1H_2. \tag{1}$$

Here $Q_i=(u_i,d_i)_L$, $L_i=(\nu_i,e_i)_L$, $H_1=(H_{11},H_{12})$, $H_2=(H_{21},H_{22})$, $\overline{u_i}=u^c_{R,i}$, $\overline{d_i}=d^c_{R,i}$, $\overline{\nu_i}=\nu^c_{R,i}$, $\overline{e_i}=e^c_{R,i}$, $H_1H_2=\epsilon^{ij}H_{1i}H_{2j}$. The model under consideration is a minimal generalization of the MSSM, the single difference is that neutrinos are massive and Dirac particles. The standard assumption of the MSSM is that at the GUT scale, $M_{\rm GUT}\approx 2\times 10^{16}$ GeV, the soft supersymmetry-breaking parameters are universal. For the gaugino masses, an account of the evolution from the GUT scale to the observable electroweak scale leads to the formula[8]

$$M_i=\frac{\overline{\alpha_i}(M_Z)}{\alpha_{\rm GUT}}m_{1/2}. \tag{2}$$

The gaugino associated with the $U(1)$ gauge group is the lightest among the gauginos, and numerically its mass is given by the formula

$$M_1\approx 0.43m_{1/2}. \tag{3}$$

Here $m_{1/2}$ is the common gaugino mass at the GUT scale. In the MSSM the right-handed sleptons usually are the next-to-lightest superparticles, and in neglect of the Yukawa interactions their masses are determined by the formula[8]

$$m^2_{\tilde{E}_R}\approx m_0^2+0.14m_{1/2}^2-0.22\cos 2\beta M_Z^2. \tag{4}$$

Here m_0 is the common squark and slepton mass at the GUT scale, and $\tan(\beta)=\langle H_1\rangle/\langle H_2\rangle$. In neglect of the Yukawa interactions the right-handed sneutrino masses coincide with m_0. It follows from formulas (2) and (3) that for $m_{1/2}\geqslant 2.3m_0$ the right-handed sneutrinos are the lightest superparticles. Especially interesting is the particular case when $m_0\leqslant 0.17m_{1/2}$. In this case the charged right-handed sleptons are the next-to-lightest superparticles. The case $m_0\ll m_{1/2}$ is theoretically very attractive, since it allows one to solve the SUSY flavor changing problem. For the scenario when the lightest superparticle is the right-handed sneutrino[c)] and the right-handed sleptons are the next-to-lightest superparticles (to be precise, allowance for nonzero Yukawa interactions makes the right-handed tau slepton the lightest of the right-handed sleptons), the right-handed tau slepton is a long-lived particle due to the smallness of the neutrino masses. After integration over the superfields H_1,H_2 one can find the effective superpotential describing the decay of right-handed sleptons into right-handed sneutrino:

$$W_{\rm eff}=h_{\nu_i}h_{e_j}L_i^kL_j^l\epsilon_{kl}\overline{\nu_i}\overline{e_j}\frac{1}{\mu}. \tag{5}$$

For $m_{\nu_\mu} \gg m_{\nu_e}$ and $m_{\tilde{\tau}_R} \gg m_{\tilde{\nu}_i}$ the decay width of the tau slepton in the reaction $\tilde{\tau}_R \to \tilde{\nu}_{\mu,R} \nu_\tau \mu, \tilde{\nu}_{\mu,R} \nu_\mu \tau$ is determined by the formula

$$\Gamma(\tilde{\tau}_R) \approx \frac{1}{192\pi^3} \frac{m^3_{\tilde{\tau}_R}}{\mu^2} \frac{m^2_\tau m^2_{\nu_\mu}}{v^2 (\sin(2\beta))^2}, \tag{6}$$

where $v = 174$ GeV, and $m_{\tilde{\tau}_R}$ is the tau right-handed slepton mass. It follows from formula (5) that due to the smallness of the muon neutrino mass the right-handed tau slepton is a long-lived particle. For instance, for $m_{\tilde{\tau}_R} = 100$ GeV, $\mu = 500$ GeV, $\sin(2\beta) = 0.1$, and $m_{\nu_\mu} = 100$ eV the stau lifetime is $\tau(\tilde{\tau}_R) \sim 0.3$ s. For $m_{\nu\mu} = 10$ eV the stau lifetime is $\tau(\tilde{\tau}_R) \sim 30$ s. Such a charged particle is long-lived (it decays outside the detector), and that changes completely the signatures in the search for supersymmetry at supercolliders. Remember that the standard signatures used for the search for supersymmetric particles at supercolliders, on the assumption that the LSP is neutral and escapes detection, are events with hadronic jets + missing E_T + $(n \geqslant 0)$ isolated leptons. The missing E_T arises from nonobservation of the electrically neutral LSP. In our case one will not have missing transverse energy E_T, but instead, as a result of the decay of the right-handed sleptons, there will be two long-lived charged sleptons of opposite sign in the SUSY event. If these sleptons are nonrelativistic, one can distinguish them from muons by their highly ionized tracks. For relativistic sleptons it is difficult to distinguish them from muons, so one will have an excess of multimuon events in the final states with 5 or more isolated muons and very little hadronic activity. The standard background with 5 or more isolated muons is extremely small, and the predicted signature is very clean. It should be noted that in gauge-mediated supersymmetry-breaking models charged sleptons could be the next-to-lightest superparticles and decay outside the detector for a large region of parameter space.[6] A similar situation takes place in a model with superweak explicit R-parity violation.[7] The phenomenology of these models is very similar to the phenomenology of the model considered and has been discussed in Refs. 6 and 10.

In conclusion let us formulate our main results. We have considered the simplest generalization of the MSSM model — the MSSM with nonzero Dirac neutrino masses. We have shown that for large and theoretically very attractive regions of parameter space the lightest superparticle is the right-handed sneutrino and the next-to-lightest superparticle is the right-handed tau slepton. Due to the smallness of the tau neutrino mass the right-handed tau slepton is a long-lived particle and decays outside the detector, thus altering completely the MSSM signatures used in the search for supersymmetry at supercolliders.

I am indebted to V. A. Rubakov for discussions and critical comments. The research described in this paper was made possible in part by Award No RPI-187 of the U. S. Civilian Research and Development Foundation for the Independent States of the Former Soviet Union (CRDF).

[a)]e-mail: krasniko@ms2.inr.ac.ru
[b)]The phenomenology of the model considered is similar to the phenomenology of some gauge-mediated supersymmetry-breaking models[6] and a model[7] with superweak R-parity violation.
[c)]It has been shown[9] that the right-handed sneutrino with a mass ~ 2 GeV is a natural candidate for dark matter.

[1] S. Dimopoulos and S. Raby, Nucl. Phys. B **192**, 353 (1981).
[2] E. Witten, Nucl. Phys. B **185**, 513 (1981).
[3] S. Dimopoulos, S. Raby and F. Wilczek, Phys. Rev. D **24**, 1681 (1981).
[4] For review and references, see: H. P. Nilles, Phys. Rep. **110**, 3 (1984).
[5] For review and references, see: H. Baer *et al.*, Mod. Phys. A **4**, 4111 (1989); H. Baer *et al.*, ''Low energy supersymmetry phenomenology,'' CERN-PPE/95-45; N. V. Krasnikov and V. A. Matveev, Phys. Part. Nucl. **28**, 441 (1997).
[6] D. R. Stump, M. Wiest and C. P. Yuan, Phys. Rev. D **54**, 1936 (1996); S. Dimopoulos, M. Dine, S. Raby, and S. Thomas, Phys. Rev. Lett. **76**, 3494 (1996); S. Ambrosanio, G. L. Kane, G. D. Kribs *et al.*, Phys. Rev. Lett. **76**, 3498 (1996).
[7] N. V. Krasnikov, Phys. Lett. B **386**, 161 (1996); N. V. Krasnikov, JETP Lett. **63**, 503 (1996).
[8] Reviews and original references can be found in: R. Barbieri, Riv. Nuovo. Cim. **11**, 1 (1988); A. B. Lahanus and D. V. Nanopoulos, Phys. Rep. **145**, 1 (1987); H. E. Haber and G. L. Lane, Phys. Rep. **117**, 75 (1985); H. P. Nilles, Phys. Rep. **110**, 1 (1984).
[9] V. A. Kuzmin, http://xxx.lanl.gov/abs/hep-ph/9701269.
[10] J. L. Feng and T. Moroi, LBNL-preprint-41133 (1997); http://xxx.lanl.gov/abs/hep-ph/9712499.

Published in English in the original Russian journal. Edited by Steve Torstveit.

Investigation of the reaction $D(e,pp)e'\pi^-$ on a tensor-polarized deuterium target at high proton momenta

A. Yu. Loginov, A. V. Osipov, A. A. Sidorov, and V. N. Stibunov[a)]
Scientific-Research Institute of Nuclear Physics, Tomsk Polytechnical University, 634050 Tomsk, Russia

B. B. Voĭtsekhovskiĭ, D. M. Nikolenko, S. G. Popov,[b)] I. A. Rachek, D. K. Toporkov, and E. P. Tsentalovich
Institute of Nuclear Physics, Siberian Branch of the Russian Academy of Sciences, 630099 Novosibirsk, Russia

(Submitted 26 March 1998)
Pis'ma Zh. Éksp. Teor. Fiz. **67**, No. 10, 730–736 (25 May 1998)

The differential cross section of the reaction $D(e,pp)e'\pi^-$ is measured in the range of proton momenta 300–720 MeV/c and proton emergence angles 64–83° for invariant masses of the pp system ranging from $2m_p$ to 2220 MeV/c^2. The measured values of the cross section are found to differ substantially from single-particle model calculations. The components of the analyzing power for this reaction are measured. © *1998 American Institute of Physics.*
[S0021-3640(98)00310-7]

PACS numbers: 25.30.Rw, 27.10.+h

There are few experimental results so far on exclusive electro- and photoproduction of π^- mesons on deuterons, especially for values of the two proton momenta above 250 MeV/c, where reaction mechanisms which have still not been investigated could appear. In an experiment performed at the Bonn electron synchrotron, an estimated upper bound on the cross section for the production of a narrow dibaryon resonance (with mass 2230 MeV/c^2) observed in the distribution over the invariant mass of the $pp\pi^-$ system, was obtained, and a narrow peak was observed at 2014 MeV/c^2 in the mass distribution of the pp system.[1,2] In experiments on the DESY synchrotron manifestations of $\Delta\Delta$ states in the deuteron were observed in the angular and energy distributions of the $p\pi^-$ pairs produced in a γD reaction.[3] The photoyields of π^- mesons in an exclusive reaction, measured at Saclay, differed appreciably from theoretical estimates.[4]

The investigations described in the present letter were conducted in a range of larger proton emergence angles and masses of the pp system than in previous experiments. This kinematic range is of interest because there is a possibility of obtaining new information about the dynamics of the NN interaction at short distances and about the role of exchange currents and isobaric configurations. Moreover, we have measured the components of the analyzing power, which are highly sensitive to different dynamical effects and to the details of the deuteron structure.

The experiment was performed at 2 GeV on the internal target of the VÉPP-3

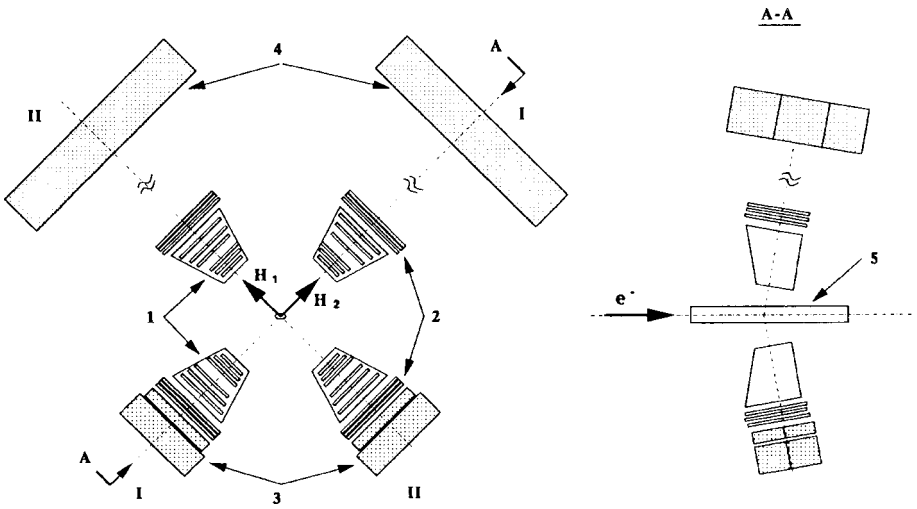

FIG. 1. Diagram of the detection system: *1* — Drift chambers, *2* — thin plastic scintillation counters, *3* — NaI(Tl) scintillation counters, *4* — thick plastic scintillation counters, 5 — storage cell–target, $\mathbf{H}_1$ and $\mathbf{H}_2$ are the directions of the magnetic guide field.

electron storage ring simultaneously with measurements of the components of the tensor analyzing power for elastic *ed* scattering[5] and electrosplitting of the deuteron.[6] An internal polarized deuterium gas target was used.[7] The deuterium target thickness visible by the detector was $(3.0\pm 0.12)\times 10^{11}$ atoms/cm^2, and its degree of tensor polarization was determined from elastic *ed* scattering measurements as $|P_{zz}|=0.572\pm 0.053$.[5]

The measurements were performed by the method of detecting two protons in coincidence using a detection system consisting of two identical two-arm detectors. The arrangement of the detectors is shown in Fig. 1. All four arms of the two proton detectors were also hadron detectors in an elastic *ed*-scattering experiment.[5,8] The angle between the median planes of the detectors was equal to 90°. The arms of the detectors, positioned symmetrically with respect to the axis of the electron beam, each included six drift chambers and three plastic scintillation counters with thicknesses of 4, 10, and 10 mm. The spatial resolution of the drift chambers was equal to 1 mm. Two ''thick'' (5 and 11 cm thick) 22 × 30 and 22 × 45 cm NaI(Tl) scintillation layers were placed one after the other behind the thin counters in the two lower arms of the detectors. In the upper proton telescopes the ''thick'' layer ($60\times 100\times 20$ cm) consisted of three polystyrene scintillation blocks 20×100 cm in area and 20 cm thick, placed 1.7 m from target center behind the thin counters. Two photomultipliers viewed the scintillation blocks from the ends.

Each proton telescope provided for the detection of particles emerging from the target in the range of polar angles θ from 64 to 84°. The interval $\Delta\varphi$ of azimuthal angles was equal to 36°. Only events in which both protons remained in the detector were used. The range of measured proton kinetic energies was 46–264 MeV and 55–180 MeV for the lower and upper proton telescopes, respectively. The energy of the protons was determined from the ratios of the energy losses in the scintillation layers. The particle energy losses in the telescope components and the amplitude and energy distributions in the scintillation layers were calculated by the Monte Carlo method using the UNIMOD-2

code.[9] Absolute calibration of the telescope counters was performed periodically by measuring in the scintillation layers the energy losses of cosmic rays and protons with known energy from the reaction $D(e,pn)e'$. The energy resolution of the telescopes depended on the energy of the protons and was no worse than 8% for protons with energy $E_p<145$ MeV and 10% for $E_p<264$ MeV. The simulated detector resolution with respect to the effective mass of the *pp* system has the following form:

M_{pp}, MeV/c^2	2000	2030	2160	2090	2120	2150
$\sigma_{M_{pp}}$, MeV/c^2	4.2	5.4	5.8	6.9	7.7	8.1

For each detected event, information from the drift chambers, the pulse heights of the scintillation counters, the temporal positions of the pulses of all the plastic scintillation counters, the accelerator current, and the sign of the tensor polarization of the target were recorded on tape. The data files collected were subjected to initial programmed processing, during which the counters were calibrated, the data were corrected and filtered, and the geometric, temporal, and amplitude characteristics of the events were reconstructed. At the next stage of processing the protons were identified, the momentum vectors of both protons were determined, and the coordinates of the event vertex were reconstructed. The pion momentum and the photon energy were calculated in the approximation of zero electron scattering angle. Events were selected for which the polar emergence angles of the protons fall into the interval $\theta_{1,2}=64$–$84°$, the coordinates of the vertex lie in the electron-beam–target interaction region, and the undetected mass is not less than the rest mass of a charged pion.

For the selected events, the reaction yields Y^i_{jk} in each detector i were determined for two signs j of P_{zz} and two directions k of the magnetic guide field. The yield Y of the reaction $D(e,pp)e'\pi^-$, summed over i, j, and k, in the six-dimensional phase volume V_6 of the momentum space $(\mathbf{p}_1, \mathbf{p}_2)$ and the differential cross section of the reaction are related as

$$Y(V_6)=\int_{V_6}\frac{\epsilon L}{K_t}\frac{d^6\sigma}{d^3p_1d^3p_2}d^3p_1d^3p_2, \tag{1}$$

where ϵ is the efficiency of detection and selection of *pp* events, K_t is the total coefficient of correction for the nuclear interaction of the protons in the telescope materials and the dead time of the detector, and L is the integrated luminosity, obtained from elastic *ed*-scattering measurements. The reaction phase volume V_6 captured by the detector was calculated by the Monte Carlo method.

The volume V_6 can be divided into elements δV_6 whose number is chosen according to the amount of statistical data collected. Representing an element of phase volume as $\delta V_6(x)=V_5(x)\delta x$, where δx denotes the partitioning interval for any of the six independent variables, we obtain on the basis of expression (1) the experimental differential cross section averaged over δV_6:

$$\frac{d^6\sigma}{dxdV_5}(x)=\frac{\Delta Y(\delta V_6(x))K_t}{\delta x V_5\epsilon L}. \tag{2}$$

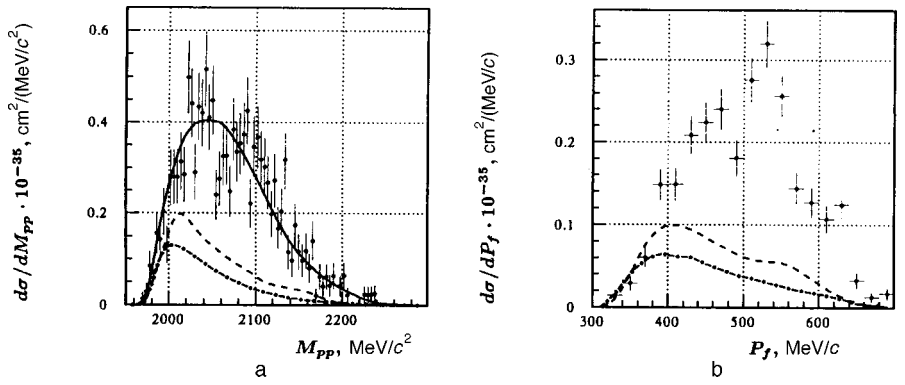

FIG. 2. Cross section of the reaction D$(e,pp)e'\pi^-$ as a function of: a) the effective mass of the *pp* system, and b) the momentum of the ''fast'' proton. Solid line — phase distribution, dashed line — ENIGMA, dot-dash line — NEWGAM.

Here $\Delta Y(\delta V_6)$ is the reaction yield in the volume $\delta V_6(x)$. Relation (2) can be integrated over $dV_5(x)$ and the quantity $d\sigma(V_5(x))/dx$ obtained can be defined as the differential cross section with respect to the chosen variable. In this manner one can obtain the distribution of a quantity that depends on all six parameters, for example, the effective mass of the proton–proton system. For any value of M_{pp} and interval δM_{pp} the events for which $\mathbf{p}_1$ and $\mathbf{p}_2$ satisfy the condition $M_{pp} < \sqrt{(E_1+E_2)^2-(\mathbf{p}_1+\mathbf{p}_2)^2} < (M_{pp} + \delta M_{pp})$ are selected. In this manner one can find the reaction yield, which depends on M_{pp} and the magnitude of the interval δM_{pp}, in an element of volume $\delta V_6(M_{pp})$ and then the desired distribution

$$\frac{d\sigma(\delta V_6(M_{pp}))}{dM_{pp}} = \frac{\Delta Y(\delta V_6(M_{pp}))K_t}{\epsilon L\, \delta M_{pp}}. \tag{3}$$

The dependence of the cross section (2) integrated over dV_5 on the momentum of the ''fast'' proton, i.e., the proton with the highest energy in each event, and the dependence of the cross section (3) on the effective mass of the *pp* system are presented in Fig. 2. The statistical errors of the measurements are shown in the figure, and the systematic errors in the measurements do not exceed 5%.

The experimental results were analyzed in the single-photon approximation. The cross section of the process initiated by electrons can be expressed in terms of the cross section of a reaction induced by virtual photons:

$$\frac{d^6\sigma_e}{d^3p_1 d^3p_2} = \int_0^{\varepsilon_i - m_e} d\omega \int_{\Omega_e} d\Omega_e \frac{n(\varepsilon_i, \omega, \theta_e, \varphi_e)}{\omega} \frac{d^6\sigma_{\gamma^*}(\omega)}{d^3p_1 d^3p_2}. \tag{4}$$

Here $n(\varepsilon_i, \omega, \theta_e, \varphi_e)$ determines the energy and angular distributions of the virtual photons. The cross section of the photoprocess can be taken out from under the integral over $d\Omega_e$ for $\theta_e = 0$ (forward-scattering approximation). The energy spectrum $N(\varepsilon_i, \omega)$ of the virtual photons, which is obtained by integrating $n(\varepsilon_i, \omega, \theta_e, \varphi_e)$, has the form presented in Ref. 10. In the forward-scattering approximation a virtual photon on the right-hand side of Eq. (4) can be replaced by a real photon. If the production of two protons is

accompanied by the production of only single π^- mesons, then the right-hand side of Eq. (4) contains the cross section for the photoproduction of π^- on a deuteron in the case when the proton momenta $\mathbf{p}_1$ and $\mathbf{p}_2$ are determined:

$$\frac{d^6\sigma_\gamma}{d^3p_1 d^3p_2} = K(\omega, \mathbf{p}_1, \mathbf{p}_2)\overline{|M_\gamma|^2}\delta(\omega + M_d - E_1 - E_2 - E_\pi). \tag{5}$$

Here $K(\omega, \mathbf{p}_1, \mathbf{p}_2)$ is a kinematic factor, and M_γ is the amplitude of the π^- photoproduction reaction on a deuteron.

Substituting expression (5) into Eq. (4), we obtain

$$\frac{d^6\sigma_e}{d^3p_1 d^3p_2} = \frac{N(\varepsilon_i, \omega_r)}{\omega_r} K(\omega_r, \mathbf{p}_1, \mathbf{p}_2)\overline{|M_\gamma|^2}, \tag{6}$$

where ω_r is found from the conservation laws for the reaction $\mathrm{D}(e,pp)e'\pi^-$ with $\theta_{e'} = 0$. The amplitude M_γ was calculated on the basis of the plane-wave impulse approximation. The single-nucleon operator for the production of π^- on a neutron was taken from a phenomenological analysis.[11] The Pauli principle was taken into account in describing the proton-proton state. The calculations performed for different types of deuteron wave functions (DWFs) are essentially identical. The curves presented in the figures were obtained with DWFs based on the Paris potential.[12]

The reaction yields and distributions which we analyzed were also calculated with the ENIGMA code,[13] used for simulating exclusive pion electro- and photoproduction reactions on nuclei. This code employs a model in which an electron interacts with one nucleon in the target. The process of absorption of a virtual photon by a bound nucleon followed by emission of a pion is described by an operator describing the creation of a pion by a real photon on a free neutron.[14] The model of Ref. 15 is used for the momentum distribution of the nucleons in a deuteron. The figures show the computational results for the total reaction yield for all possible electron scattering angles obtained with ENIGMA. The reaction yield with electrons scattered in the interval of polar angles $\theta_{e'} = 0\text{–}5°$ accounts for 97% of the total yield.

The differential cross section of the reaction $\mathrm{D}(e,pp)e'\pi^-$ on a polarized deuteron, integrated over all independent variables except for the solid angle Ω_p of the ''slow'' proton, can be expressed as[16]

$$\frac{d\sigma}{d\Omega_p} = \frac{d\sigma_0}{d\Omega_p}\left\{1 - \frac{\sqrt{3}}{2}P_z \sin\theta_d \sin\varphi_d T_{11} + \frac{P_{zz}}{\sqrt{2}}\left[\frac{3\cos^2\theta_d - 1}{2}T_{20} + \sqrt{\frac{3}{8}}\sin 2\theta_d \cos\varphi_d T_{21} + \sqrt{\frac{3}{8}}\sin^2\theta_d \cos 2\varphi_d T_{22}\right]\right\}, \tag{7}$$

where $d\sigma_0/d\Omega_p$ is the cross section of the reaction on an unpolarized target; T_{11}, T_{20}, T_{21}, and T_{22} are the components of the vector and tensor analyzing powers; P_z and P_{zz} are the degrees of vector and tensor polarizations of the target; the angles θ_d and φ_d determine the direction of the magnetic guide field in a coordinate system where the z

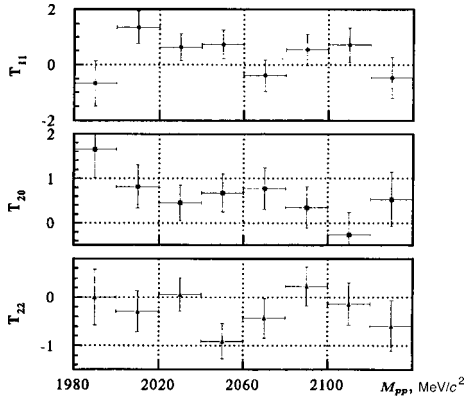

FIG. 3. Experimental results for the components of the analyzing power as a function of the effective mass of the *pp* system.

axis is directed along the axis of the electron beam and the *xz* plane is the emergence plane of the ''slow'' proton. Using expression (7) and given the experimental yields Y^i_{jk}, one can obtain the components of the analyzing power:

$$T_{11}=\frac{k_\phi 3\sqrt{2}}{|P_z|}\,\frac{\Sigma_{i=1,2}(-1)^{\delta_{i1}}[Y^i_{1+}+Y^i_{2-}]}{Y},\quad T_{20}=-\frac{\sqrt{8}}{|P_{zz}|}\,\frac{[\Sigma Y^i_{j+}-\Sigma Y^i_{j-}]}{Y},$$

$$T_{22}=-\frac{4k_\phi}{\sqrt{3}|P_{zz}|}\,\frac{\sum\limits_{i,j=1,2}(-1)^{\delta_{ij}}[Y^i_{j-}-Y^i_{j+}]}{Y}, \tag{8}$$

where k_ϕ is a correction which takes into account the detection interval for the azimuthal angle and Y is the reaction yield summed over all states. As we noted earlier,[6] these combinations make it possible to reduce the systematic errors of the measurements to a minimum.

Analyzing the experimental data obtained, one notices that there are no reliably observed resonances in the experimental mass interval of the *pp* system (Fig. 2a) and that the experimental *pp* mass distribution, in contrast to the phase distribution, has the following structure: diffuse peaks, which are wide compared with the detector resolution, near the masses 2036 MeV/c^2 and 2100 MeV/c^2 and a narrow peak near 2041 MeV/c^2. However, additional measurements and careful analysis are required in order to determine the nature of this structure. It is evident from the same figure that the experimental cross sections are much larger than the computed cross sections and that this discrepancy increases with the mass of the *pp* system. The experimental and computed cross sections also differ appreciably in shape.

An increase in the disagreement with the theoretical calculations for momenta 400–500 MeV/*c* can be seen in the behavior of the measured cross section as a function of the momentum of the ''fast'' proton (Fig. 2b). Here, just as in Fig. 2a, the calculations do not describe the shape of the experimentally observed dependences of the cross sections. The cross section as a function of the momentum of the ''slow'' proton also behaves simi-

larly. This shows that the single-particle models selected, which describe satisfactorily the behavior of the cross sections for the electro- and photoproduction of π^- mesons on deuterium in the region of comparatively small momenta of the spectator proton,[17] do not give agreement with the results of our experiment. The dependence of the measured polarization observables on M_{pp} is shown in Fig. 3. One can see that the character of the behavior of analyzing power components is different, while T_{22} is observed to increase substantially near the mass 2050 MeV/c^2. The large value of the component T_{20} of the analyzing power is interesting. Irrespective of the interpretation of the polarization data, the experimentally observed large values of the analyzing power components of the reaction are of practical interest for deuteron polarimetry.

The above analysis of the distributions does not exhaust all possibilities for experiment. In future investigations the set of distributions which are analyzed will be enlarged and additional reaction mechanisms, taking into account the contribution of meson exchange currents and excitation and decay of nucleon resonances, will be considered.

This work was supported by the Russian Fund for Fundamental Research (No. 93-02-3514).

[a)]e-mail: stib@npi.tpu.ru
[b)]Deceased.

[1] B. Bock, W. Ruhm, K. H. Althoff *et al.*, Nucl. Phys. A **459**, 573 (1986).
[2] W. Ruhm, B. Bock, K. H. Althoff *et al.*, Nucl. Phys. A **459**, 557 (1986).
[3] P. Benz and P. Soding, Phys. Lett. B **52**, 367 (1974).
[4] P. E. Argan, G. Audit, A. Bloch *et al.*, Phys. Rev. Lett. **41**, 86 (1978).
[5] R. Gilman, R. J. Holt, E. Kinney *et al.*, Phys. Rev. Lett. **65**, 1733 (1990).
[6] S. I. Mishnev, D. M. Nikolenko, S. G. Popov *et al.*, Phys. Lett. B **302**, 23 (1993).
[7] R. Gilman, R. J. Holt, E. Kinney *et al.*, Nucl. Instrum. Methods A **327**, 277 (1993).
[8] L. G. Isaeva, B. A. Lazarenko, D. M. Nikolenko *et al.*, Nucl. Instrum. Methods A **325**, 16 (1993).
[9] A. D. Bukin, N. A. Grozina, M. S. Dubrovin *et al.*, ''UNIMOD-2,'' Preprint 94-20, Institute of Nuclear Physics, Siberian Branch of the Russian Academy of Sciences, Novosibirsk (1994).
[10] R. H. Dalitz and D. R. Yennie, Phys. Rev. **105**, 1598 (1957).
[11] W. J. Metcalf and R. L. Walker, Nucl. Phys. B **76**, 253 (1974).
[12] M. Lacombe, B. Loiseau, J. M. Richard *et al.*, Phys. Rev. C **21**, 861 (1980).
[13] J. L. Visschers, in *Proceedings of MC93 International Conference on Monte Carlo Simulation in High Energy and Nuclear Physics*, edited by P. Dragovitsch, WSP (1994), p. 350.
[14] I. Blomqvist and J. M. Laget, Nucl. Phys. A **280**, 405 (1977).
[15] I. E. Lagaris and V. R. Pandharipane, Nucl. Phys. A **359**, 331 (1981).
[16] Yu. P. Melnik and A. V. Shebeko, Phys. Rev. C **48**, 1259 (1993).
[17] P. E. Scheffler and P. L. Walden, Nucl. Phys. B **75**, 125 (1974).

Translated by M. E. Alferieff

Study of $\Delta(1232)$ isobar electroproduction at the VEPP-2M e^+e^- collider

M. N. Achasov,[a] A. V. Bozhenok, A. D. Bukin, D. A. Bukin, S. V. Burdin, T. V. Dimova, S. I. Dolinsky, V. P. Druzhinin, M. S. Dubrovin, I. A. Gaponenko, V. B. Golubev, V. N. Ivanchenko, A. A. Korol, S. V. Koshuba, A. P. Lysenko, E. V. Pakhtusova, V. V. Shary, Yu. M. Shatunov, V. A. Sidorov, Z. K. Silagadze, S. I. Serednyakov, A. A. Valishev, and Yu. V. Usov

G. I. Budker Institute of Nuclear Physics, Siberian Branch of the Russian Academy of Sciences, 630090 Novosibirsk, Russia

(Submitted 6 April 1998)
Pis'ma Zh. Éksp. Teor. Fiz. **67**, No. 10, 737–740 (25 May 1998)

Results from the Spherical Nonmagnetic Detector (SND) on $\Delta(1232)$ isobar electroproduction in the collisions of beam electrons (positrons) and residual gas nuclei in the VEPP-2M e^+e^- collider are presented. On the basis of the data obtained the expected counting rate of this process in future high-luminosity e^+e^- colliders (ϕ, $c-\tau$, and b factories) is estimated. © *1998 American Institute of Physics.* [S0021-3640(98)00410-1]

PACS numbers: 25.30.Rw, 14.20.Gk, 13.65.+i

Electron or positron beams propagating along a collider beam pipe can produce pions on nuclei of residual gas atoms. At a beam energy of $E_0 \approx 500$ MeV (ϕ-factory region) the main source of such pions is the electroproduction of the $\Delta(1232)$ $I(J^P) = 3/2(3/2^+)$ isobar state.[1] In an electron–nucleus collision a nucleon can convert into either Δ^+ ($ep \to e\Delta^+$) or Δ^0 ($en \to e\Delta^0$) with a subsequent decay of $\Delta(1232)$ into nucleon and pion: $\Delta^+ \to p\pi^0, n\pi^+$; $\Delta^0 \to p\pi^-, n\pi^0$. The total number of π^0 produced is twice as high as that of π^+ or π^-. At an electron energy of about 500 MeV the cross section of the isobar electroproduction is proportional to A, the atomic weight of the target. But only those Δ-isobars which are produced on the surface of the nucleus will actually decay by $\Delta \to N\pi$. For Δ-isobars produced inside the nucleus the reaction $\Delta N \to NN$ dominates. This means that the $eN \to e\Delta$, $\Delta \to \pi N$ cross section must be proportional to $A^{2/3}$.

The total cross section of the isobar electroproduction on a nucleon at an electron energy of 510 MeV is about 3 μb. This reaction is a possible source of background at ϕ factories.[2] It can be also an actual background in experiments at higher energies (its total cross section is about 8 μb in the $c-\tau$- and 12 μb in the b-factory energy region). This paper presents results of experimental study of $\Delta(1232)$ electroproduction with the SND detector at the VEPP-2M e^+e^- collider in Novosibirsk. The SND detector[3] consists of a drift chamber tracking system with an angular resolution $\sigma_\theta = 2.2°$, $\sigma_\phi = 0.7°$ and dE/dx resolution of about 30%, a three layer NaI(Tl) spherical electromagnetic calorimeter[4]

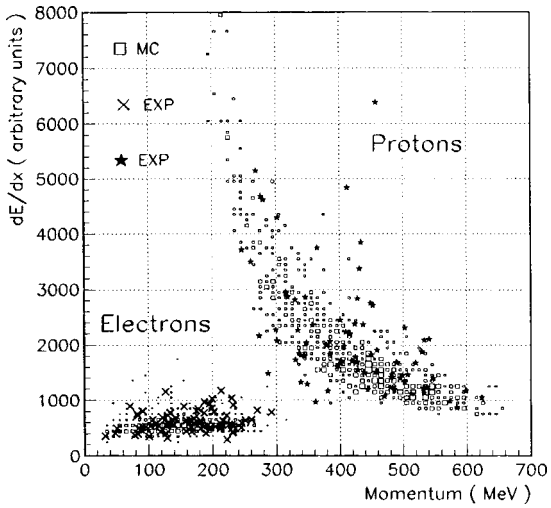

FIG. 1. dE/dx, specific ionization losses of electrons and protons, produced in $\Delta(1232)$ decays. Crosses — electrons, stars — protons.

with an angular resolution $\sigma_\theta = \sigma_\phi = 1.5°$ and energy resolution $\sigma_E/E = 4.2\%/\sqrt[4]{E(\mathrm{GeV})}$ for photons, and a muon identification system. The Δ-isobar electroproduction process was studied in the $ep \to e\Delta^+$, $\Delta^+ \to p\pi^0$ channel because of its very distinct signature: two photons from π^0-meson decay and two tracks from electron and proton. It is important that in this case the photon energies and invariant masses are known, and electron/proton separation based on dE/dx measurements in the drift chambers is possible. Monte Carlo simulation of the Δ-isobar electroproduction on a single proton, based on formulas from Ref. 2, was used for studying selection criteria and detection efficiency. The passage of particles through the detector was simulated using the UNIMOD-2 code.[5]

Experimental data collected in 1996 in the energy range $2E_0 = 1.00–1.04$ GeV,[6] with an integrated luminosity of $L = 0.5$ pb^{-1} were processed. Events with two charge particles and two photons were selected for further analysis. To suppress the background from decays of copiously produced ϕ mesons ($\phi \to 3\pi, K_S K_L, K^+K^-$, etc.) the following selection criteria were applied: the total energy deposition in the calorimeter had to be less than the beam energy E_0, the angle between charged particles had to be smaller than 150 degrees, which greatly reduces K^+K^- and $K_S K_L$ background, and dE/dx for one of the charged particles had to be at least twice that of a minimum ionizing particle. The coordinate of a Δ-isobar production point along the beam was reconstructed from the charged-particle tracks. Then a kinematic fit was performed under following constraints: the particle with the larger dE/dx is considered to be a proton; the total transverse momentum $p_\perp = 0$; the longitudinal momentum $p_\parallel = E_0/c$; the photons originate from $\pi^0 \to \gamma\gamma$ decay; and the total energy $E = E_0 + m_p c^2$, where m_p is the mass of a proton. Eighty events consistent with these assumptions were found. Their production points are uniformly distributed along the beam direction of a 20-cm fiducial length, in contrast with the background, which is peaked at the point of collision of the beams. The dependence of dE/dx on the reconstructed charged-particle momentum is shown in Fig. 1. Electrons

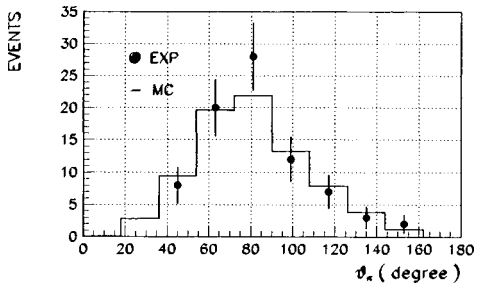

FIG. 2. The π^0 polar angle distribution in $\Delta(1232)$ decay.

and protons are well separated, and the momentum dependence of the proton specific ionization losses is clearly seen. The characteristic feature of the $\Delta \to \pi N$ decay is that π-mesons are emitted at large angles with respect to the beam direction.[2] The experimental and simulated distributions shown in Fig. 2 are in good agreement. The proton–pion invariant mass spectra (Fig. 3) are peaked between 1200 and 1250 MeV. The peaks are located at 1218 ± 6 MeV and 1235 ± 2 MeV in the experimental and simulated distributions, respectively. The expected number of selected experimental events can be written as:

$$N = \frac{I}{e} t \sigma N_p l \epsilon,$$

where $I = 30$ mA is the average beam current, e is the electron charge, $t = 7 \times 10^5$ s is the total data acquisition time, $l = 20$ cm is the fiducial length, $\sigma = 2\,\mu$b, N_p is the effective density of protons, and $\epsilon = 0.026$ is the detection efficiency. The number of observed experimental events is $N = 80 \pm 9(\text{statistical}) \pm 10(\text{systematic})$. This corresponds to $N_p = 6 \times 10^{14}/\text{m}^3$. The residual gas pressure is $P = nkT$, where k is Boltzmann's constant, $T = 300$ K, and n is the density of residual gas molecules. The expected composition of the residual gas is H_2 — 30%, CH_4 — 10%, CO — 20% and CO_2 — 40%. In this case $N_p = 6n$, and P, calculated using the above expression, is equal to 3 ± 0.4(statistical) ± 2(systematic) nTorr. This value agrees with direct pressure measurements: $P = 3 \pm 2$ nTorr. The large systematic error in the former value is due to uncertainty in the residual gas composition. At the DAΦNE ϕ factory[7] ($I = 5$ A, $P = 1$ nTorr) the rate of the $ep \to e\Delta^+$, $\Delta^+ \to p\pi^0$ reaction is ~ 1.2 Hz/m. Taking into account $\Delta^+ \to n\pi^+$ decay and Δ^0 electroproduction on the neutrons the counting rate raises up to 4 Hz/m. This value agrees with estimate in Ref. 2. The ϕ-factory experimental program includes CP violation in kaon decays, rare decays of ϕ mesons, two-photon processes, and $e^+e^- \to$hadrons annihilation at low energies.[8] The $\Delta(1232)$ electroproduction process could be a considerable source of background, for instance, for two-photon processes (the counting rate for $\gamma\gamma \to \pi^0$ is expected to be 0.2 Hz).[9] Its counting rate is also comparable with the rate of the rare ϕ-meson decays $\phi \to \gamma\eta', \gamma f_0(980), \gamma a_0(980)$ ($\leqslant 0.5$ Hz), or with $K_L \to \pi\pi$ decays ($\leqslant 2$ Hz). On the other hand $\sim 4 \times 10^7$ $\Delta(1232)$ decay events would be produced at the ϕ factory per effective year (10^7 s) per meter of fiducial length.

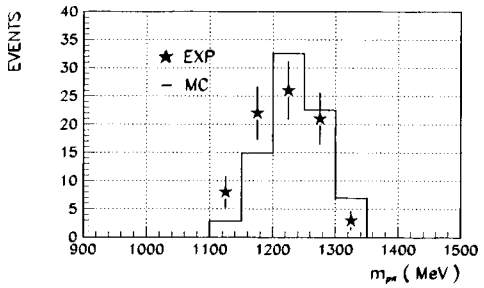

FIG. 3. The $p\pi^0$ invariant mass distribution in the process of $\Delta(1232)$ electroproduction.

This means that, in addition to e^+e^- physics, experiments in the field of nuclear physics, e.g., studies of collective effects in nuclei (so-called $\Delta-h$ states[10]), are possible. This work was supported in part by the Russian Fund for Fundamental Research under Grants 96-15-96327 and 97-02-18561 and by the International Science Foundation under Grants RPX000 and RPX300.

[a)]e-mail: achasov@inp.nsk.su, FAX: +7(383-2)35-21-63

[1] K. N. Mukhin and O. O. Patarakin, Usp. Fiz. Nauk **165**, 843 (1995).
[2] M. N. Achasov, V. B. Golubev, S. I. Serednyakov, and N. N. Achasov, JETP Lett. **65**, 313 (1997); M. N. Achasov, N. N. Achasov, V. B. Golubev *et al.*, Phys. Lett. B **404**, 173 (1997).
[3] V. M. Aulchenko *et al.*, in *Proceedings of Workshop on Physics and Detectors for DAΦNE,* Frascati, April 1991, p. 605.
[4] M. N. Achasov, A. D. Bukin, D. A. Bukin *et al.*, Nucl. Instrum. Methods Phys. Res. A **401**, 179 (1997).
[5] A. D. Bukin, *et al.*, in *Proceedings of Workshop on Detector and Event Simulation in High Energy Physics*, Amsterdam, 8–12 April 1991, NIKHEF, p. 79.
[6] M. N. Achasov *et al.*, in *Proceedings of the 7th International Conference on Hadron Spectroscopy*, Brookhaven National Laboratory, US, August 25–30, 1997.
[7] G. Vignola, in *Proceedings of Workshop on Physics and Detectors for DAΦNE,* edited by L. Maiani, G. Pancheri, and N. Paver, LNF, Frascati, Italy, April 7–14, 1995, p. 19.
[8] L. Maiani, G. Pancheri, and N. Paver (eds.), *The Second DAΦNE Physics Handbook*, Vols. I and II, dei Laboratory Nazionali di Frascati, Frascati, Italy, May 1995.
[9] F. Anulli *et al.*, in *The Second DAΦNE Physics Handbook,* Vol. II, edited by L. Maiani, G. Pancheri, and N. Paver, dei Laboratory Nazionali di Frascati, Frascati, Italy, May 1995, p. 607.
[10] E. A. Strokovsky, F. A. Gareev, and Yu. L. Ratis, Fiz. Elem. Chastits At. Yadra **24**, 603 (1993) [Phys. Part. Nucl. **24**, 255 (1993)].

Published in English in the original Russian journal. Edited by Steve Torstveit.

First results of experiments on high-efficiency single-crystal extraction of protons from the U-70 accelerator

A. G. Afonin, V. M. Biryukov, V. A. Gavrilushkin, V. N. Gres',
B. A. Zelenov, V. I. Kotov, V. A. Maisheev, A. V. Minchenko,
V. N. Terekhov, E. F. Troyanov, and Yu. A. Chesnokov[a)]
Institute of High-Energy Physics, Russian Academy of Sciences, 142284 Protvino, Russia

M. G. Gordeeva, A. S. Denisov, Yu. M. Ivanov, A. A. Petrunin,
V. V. Skorobogatov, and B. A. Chunin
St. Petersburg Institute of Nuclear Physics, Russian Academy of Sciences, 188350 St. Petersburg, Russia

(Submitted 13 April 1998)
Pis'ma Zh. Éksp. Teor. Fiz. **67**, No. 10, 741–745 (25 May 1998)

A radical increase in the efficiency of beam extraction from an accelerator is achieved with a short (7 mm long) crystal bent by a small angle (1.7 mrad) by increasing the number of times particles pass through the crystal. A particle extraction efficiency of $\sim 20\%$, in agreement with the prediction of the theory, was achieved experimentally. A record high intensity of the extracted beam 1.9×10^{11} protons per cycle, which is four orders of magnitude higher than previous results, is obtained. © *1998 American Institute of Physics.*
[S0021-3640(98)00510-6]

PACS numbers: 29.27.Ac

Bent single crystals have been used successfully for a quite a long time now for extracting beams from accelerators, including the large modern colliders.[1–3] The use of single crystals for extracting portions of a 70 GeV proton beam into negative-particle channels is now standard practice at the Institute of High-Energy Physics.[4,5] The experimental data collected and a theoretical analysis[6] show that the decisive factor determining the extraction efficiency is the number of times a beam passes through the crystal. The reason is that when the beam is steered slowly, the depth at which the particles are ''kicked'' in the first orbit is small and equals a fraction of a micron, while the surface layer damaged during treatment is several microns thick.[7] To overcome the layer which is ineffective for channeling and radically increase the extraction efficiency, it is necessary to increase the number of times the particles pass through the crystal.[8,9] To investigate such an extraction regime a short (7 mm long) silicon crystal with a 1.7 mrad bending angle was used in the accelerator at the IHEP. The first experimental results are reported below.

Bending a short crystal while satisfying a number of conditions associated with the insertion of the crystal into an accelerator presents a definite problem. We employed a

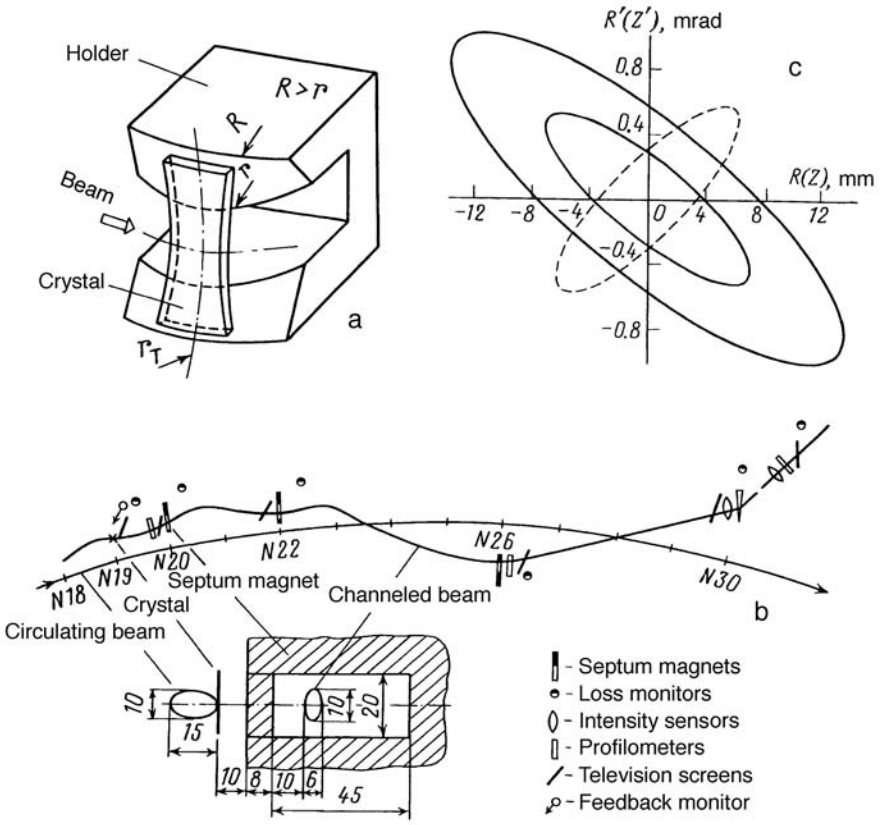

FIG. 1. a — Diagram of the crystal bending. b — Experimental arrangement. The dimensions are in mm. c — Phase portrait of the circulating beam in the U-70 at the location of the crystal: the two solid curves (denoting the core and the halo) are in the horizontal plane, the dashed curve is in the vertical plane.

Si(111) crystal in the form of a $0.5\times 40\times 7$ mm (thickness, height, and length along the beam) wafer. The crystal was bent with the aid of a metal holder containing a 20 mm slit at the center for passing the beam (Fig. 1a). To decrease the unavoidable angular deformation (twist) along the height in such a structure a crystal holder in the form of a parabolic hyperboloid was used to bend the wafer in the transverse direction. A crystal bent in this manner was pretested on an extracted 70 GeV proton beam. The experimentally measured twist can be expressed by the formula $\alpha(\mu\text{rad})=5y^2(\text{mm})$, where y is the distance from the center of the crystal along the height, and was used in calculations of the efficiency of beam extraction from the U-70 accelerator.

The crystal beam extraction scheme is displayed in Fig. 1b. In planning the experiment we proceeded from the fact that a bending angle of 1.7 mrad is insufficient for direct beam extraction. For this reason, it was decided to test the crystal in the existing slow-extraction scheme. The crystal deflector station is placed in the free rectilinear segment No. 19 of the U-70 accelerator between a thin magnet and an OM-20 slow-extraction septum magnet with an ~ 8 mm thick barrier (see Fig. 1b). The beam is steered to the crystal, which is located in the working position 60–65 mm from the equilibrium

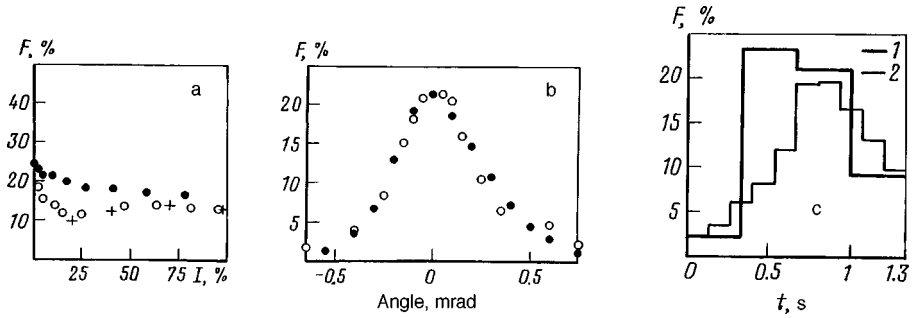

FIG. 2. a — Measured dependence (+) of the crystal beam extraction efficiency F versus the intensity I of the beam steered onto the crystal (as a percent of the beam circulating in the U-70). The results of a simulation without a halo (●) and with a 10% halo (○) are also shown. b — Crystal beam extraction efficiency F versus the crystal orientation: theory (●) and experiment (○). c — Curve *1* — measured time dependence of the extraction efficiency during steering of the beam, *2* — simulated time dependence of the extraction efficiency obtained assuming a constant steering rate.

orbit, by means of a specially produced local distortion of the orbit, which at the same time maintains an adequate distance between the beam steered to the crystal and the two septum magnets.

The crystal splitter station possesses horizontal and angular displacement mechanisms. The crystal is positioned at a prescribed coordinate with an accuracy of 0.1 mm; the angle is set with an accuracy of 45 μrad. A complex beam diagnostics system, including a television observation system, loss monitors, profilometers, and intensity meters, was used to monitor the kicking of the beam into the OM-20 aperture and the guiding of the beam along the extraction path. All the diagnostic instruments were pretested in a fast-extraction regime and calibrated over a wide intensity range. To obtain uniform steering of the beam onto the crystal in the feedback mode a feedback monitor based on an FÉU-93 photomultiplier with a scintillator was used. The monitor was placed $\sim$10 m behind the crystal at the level of the beam orbit. The total frequency band of the entire feedback loop was equal to $\sim$10 kHz.

The intensity of the accelerator varied from 1×10^{12} to 1.5×10^{12} protons per cycle in the course of the experiment. The intensity dumped onto the crystal was varied in the course of the experiment from 20% to 100%. To begin with, the radial intensity distribution in the beam was measured. Approximately 90% of the intensity was contained in an $\sim$15 mm core. The dense core is surrounded by a halo where the intensity drops off slowly. Figure 1c shows phase ellipses of the beam, which were constructed from measurements of the beam dimensions, at the entrance into the crystal.

The so-called orientation curve — the intensity of the extracted beam versus the angular orientation of the crystal — serves as a direct proof of channeling of the extracted beam. In Fig. 2b it is compared with the simulation results.

The main problem of the experiment was to determine the extraction efficiency (ratio of the extracted-beam intensity to the intensity of the beam kicked out of the accelerator). Measurements of both the integrated efficiency, i.e., over the entire extraction time, and the differential efficiency — over specific extraction time intervals — were performed. Figure 2a shows the experimental data from measurements of the extraction

efficiency for different intensities of the steered beam and the corresponding simulation results obtained with and without the 10% halo of the real beam. The decrease in efficiency for a beam with a halo is explained by the large mismatch between the orientation angle of the crystal and the angle of incidence of the beam on the crystal in the presence of an appreciable variation of the current in the system of local distortion of the orbit (Fig. 1c).

The maximum integrated extraction efficiency, which was recorded when the fraction of the beam kicked out of the accelerator was 75%, equalled $(14\pm 1.5)\%$. The differential efficiency varied during the extraction process as result of the drift of the angle of incidence of the beam on the crystal (see Fig. 1c). The results of measurements of the differential efficiency over four time intervals are shown in Fig. 2c. The absolute maximum of the efficiency was $(23.4\pm 2.5)\%$ and was recorded in a 325 ms time interval in the middle part of an extraction lasting ~ 1.3 s. The asymmetry of the curve is explained by the intensity distribution in the beam. The simulation results confirm this character of the time dependence.

The maximum intensity of the beam extracted by the crystal with the full beam circulating in the accelerator steered onto the crystal was equal to 1.9×10^{11} protons/cycle, which is four orders of magnitude higher than results obtained earlier.[1–5] The crystal successfully withstood the radiation and heat loads, heating up, according to estimates, to several hundreds of degrees.

Computer modeling of the experiment[10] was conducted beforehand in order to select the optimal crystal size, assess the influence of different parameters on the efficiency, and check the theory. The simulation took into account the real geometry of the crystal, with longitudinal and transverse bending as well as the construction of the holder. The crystal lattice was assumed to be ideal, but an amorphous layer several tens of microns thick was simulated on the surface of the crystal.[7] The initial kick depth <1 μm precluded channeling during the first pass of a particle through the crystal. The simulation included multiple passes of particles through the crystal and the multiorbital motion in the accelerator.[11]

As a result of the simulations, we found that the average number of passes through the crystal for particles of the extracted beam is much greater than 1: $\langle N\rangle \simeq 12$, while the average number of passes before a nuclear interaction occurs is ~ 40. The importance of this factor in our experiment can also be characterized as follows. The beam extraction efficiencies attained with crystals in the largest accelerators in the world are now of the same order of magnitude: approximately 20% at CERN and IHEP and about 30% at Fermilab. However, at CERN this efficiency was achieved with a divergence of the beam incident on the crystal less than the Lindhard angle. Under our conditions the beam divergence was ~ 20 times greater than the Lindhard angle ($\simeq 20$ μrad at 70 GeV), so that only a few percent of the beam could be channeled in a single pass.

The calculations show that extraction efficiencies up to 30% can be obtained by using a short crystal with no twist (such a construction is under investigation). For the U-70 accelerator, the regime in which a crystal operates simultaneously with internal targets is of practical interest. This is also part of the program of our further investigations. Our first experimental results are in good agreement with the theory, according to which extraction efficiencies of 70–90% can be obtained in high-energy accelerators and

colliders by using short crystals. Such an efficiency makes the application of short crystals very promising for beam collimation and extraction problems.

In closing, we wish to express our deep appreciation to A. A. Logunov and N. E. Tyurin for their support of this work. This work was sponsored by the Russian Fund for Fundamental Research under Grant 98-02-16941.

[a)]e-mail: chesnokov@mx.inep.su

[1]H. Akbari *et al.*, Phys. Lett. B **313**, 491 (1993).
[2]C. T. Murphy *et al.*, Nucl. Instrum. Methods Phys. Res. B **119**, 231 (1996).
[3]G. Arduini, K. Elsener, G. Fidecaro *et al.*, in *Proceedings of the Particle Accelerator Conference PAC-97*, Vancouver (1997).
[4]A. A. Asseev *et al.*, Nucl. Instrum. Methods Phys. Res. A **309**, 1 (1991).
[5]V. M. Biryukov, V. N. Chepegin, Yu. A. Chesnokov *et al.*, in *Proceedings of the Particle Accelerator Conference PAC-97*, Vancouver (1997).
[6]V. Biryukov and C. T. Murphy, Fermilab TM-2026, Batavia, Illinois (1997).
[7]V. M. Biryukov, Yu. A. Chesnokov, and V. I. Kotov, *Crystal Channeling and Its Application at High-Energy Accelerators*, Springer, Berlin, 1997.
[8]V. M. Biryukov, Nucl. Instrum. Methods Phys. Res. B **53**, 202 (1991).
[9]A. M. Taratin *et al.*, Nucl. Instrum. Methods Phys. Res. B **58**, 103 (1991).
[10]V. Biryukov, Invited talk at the''Near Beam Physics'' Symposium, Fermilab, Batavia, Illinois (1997), in press.
[11]V. M. Biryukov, Phys. Rev. E **51**, 3522 (1995); **52**, 2045 (1995); **52**, 6818 (1995); Phys. Rev. Lett. **74**, 2471 (1995).

Translated by M. E. Alferieff

Experimental check of the dispersion law for ultracold neutrons

I. V. Bondarenko, A. V. Krasnoperov, and A. I. Frank[a)]
Joint Institute of Nuclear Research, 141980 Dubna, Moscow Region, Russia

S. N. Balashov, S. V. Masalovich, and V. G. Nosov
Kurchatov Institute Russian Science Center, 123182 Moscow, Russia

P. Geltenbort and P. Hoghoj
Institut Laue-Langevin, Grenoble, France

A. G. Klein and A. Cimmino
School of Physics, The University of Melbourne, Melbourne, Australia

(Submitted 13 April 1998)
Pis'ma Zh. Éksp. Teor. Fiz. **67**, No. 10, 746–751 (25 May 1998)

An experiment to check the standard dispersion law for ultracold neutrons is described. The experiment is based on searching for a shift of the resonance line of a neutron interference filter as the neutron velocity component parallel to the filter surface is varied. The first results attest to a statistically significant effect. No mimicking effects were found in a control experiment, but their possible existence cannot be completely ruled out at present. © *1998 American Institute of Physics.* [S0021-3640(98)00610-0]

PACS numbers: 28.20.Cz, 11.55.Fv

INTRODUCTION

It is well known that the dispersion law for slow neutrons in matter can be described to a high degree of accuracy by the relation[1]

$$k^2 = k_0^2 - 4\pi\rho b, \tag{1}$$

where k is the neutron wave number in the medium, k_0 is the wave number in vacuum, ρ is the number of nuclei per unit volume, and b is the coherent-scattering length. This relation corresponds to an effective potential

$$U = \frac{2\pi\hbar^2}{m}\rho b, \tag{2}$$

where m is the neutron mass.

The question of the validity of relations (1) and (2) is of great interest, since they are widely used both in the practice of neutron optics[2] and in the physics of ultracold neutrons (UCNs).[3,4] The ''potential'' dispersion law (1) is probably not entirely accurate. In the case of thermal and cold neutrons, small corrections to this law should exist on

account of the presence of correlations in the arrangement of the scatterers.[5,6] The accuracy of present-day experiments is still too low to observe such corrections.[7] The derivation of Eq. (1) is based on the Fermi quasipotential,[8] which describes well the scattering of a neutron by a single nucleus in the Born approximation. In Ref. 9 it was shown that as the wavelength approaches infinity, the effective number of nuclei participating in coherent scattering of waves increases to such an extent that repeated scatterings by the same nucleus become important. This precludes the use of a point-like quasipotential at extremely low energies and limits the range of applicability of the dispersion law (1). For practical applications the important question is: At what wavelengths do small deviations from the potential dispersion law become evident? The present letter describes the preliminary results of an experiment designed to answer this question.

IDEA OF THE EXPERIMENT

The idea was proposed in Ref. 10 and is based on the specific properties of the potential dispersion law which were noted in Refs. 11 and 12. Let a neutron wave be refracted at the boundary of a medium, and let the dispersion law include a ''nonpotential'' correction term $\epsilon(k_0^2)$:

$$k^2 = k_0^2 - \chi_0^2 + \epsilon(k_0^2), \quad \chi_0^2 = 4\pi\rho b. \tag{3}$$

If the material is uniform along its surface, then the wave-number component k_{0t} parallel to the plane of the interface does not change on refraction. Subtracting from both sides of Eq. (3) the quantity $k_{0t}^2 = k_t^2$, we obtain

$$k_\perp^2 = k_{0\perp}^2 - \chi_0^2 + \epsilon(k_0^2). \tag{4}$$

Therefore the presence of a nonpotential term $\epsilon(k_0^2)$ causes the normal component $k_\perp$ of the wave number in the medium to depend on the magnitude k_0 of the wave number in vacuum. The objective of the present experiment is to search for such a dependence.

The main component of the apparatus is an interference filter[13,14] — the neutron analog of an optical Fabry–Perot interferometer. In the simplest case it consists of a three-layer structure deposited on a substrate (Fig. 1). The scattering-amplitude density ρb and the corresponding effective potential (2) for the outer layers are greater than for the inner layer and the substrate. For this reason, the potential structure of the filter consists of two barriers and a well between them. When the inner layer is sufficiently thick, the width of the well is sufficient for quasibound states to form. Near these levels the structure becomes penetrable by subbarrier neutrons, and the transmission function of the filter acquires a strongly resonance character.

The width of the resonance is determined by the penetrability of the outer layers, while the position of the resonance is determined by the result of matching the wave functions at the boundaries of the films. Since the problem is one-dimensional, all important characteristics of the resonance are determined only by the normal components of the real or imaginary wave vectors.

The neutron velocity relative to the filter can vary if the filter is moving in a direction parallel to its surface. It is obvious that the normal component $k_{0\perp}$ of the wave number of the incident wave remains unchanged. However, for the potential dispersion law (4), motion of the filter does result in a change in the normal component $k_\perp$ of the

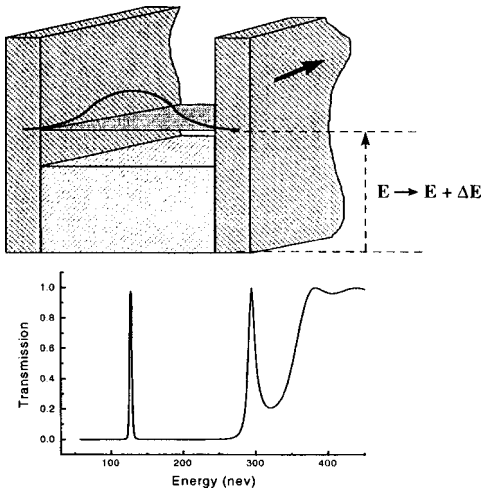

FIG. 1. Potential structure of the interference filter and energy levels of a quasibound state. In the case of a nonpotential dispersion law, setting the filter in motion gives rise to a shift of the position of the resonance. The transmission function of one filter employed in the experiment is shown in the bottom half of the figure.

wave vector in the medium and therefore in a shift of the resonance. Such a shift can be detected by measuring the energy $E_n=(\hbar^2/2m)\,k_{0\perp}^2$ of the neutrons which have passed through the filter.

EXPERIMENTAL CHECK OF THE DISPERSION LAW FOR ULTRACOLD NEUTRONS

The experiment was performed on the UCN source at the Institut Laue-Langevin (Grenoble, France).[15] The experimental apparatus is displayed in Fig. 2. Ultracold neutrons from the feed neutron guide enter the entrance chamber, and after undergoing a number of reflections they enter a cylindrical corridor which delivers the neutrons to the filter — a monochromator 150 mm in diameter. The inner and outer diameters of the corridor equal 110 and 130 mm, respectively, so that the UCNs irradiate only an annular region of the filter. The filter can be made to rotate around the vertical axis by means of a motor. The UCNs which have passed through the filter and have a sufficiently narrow energy spectrum with a maximum at 107 neV and a half-width of the order of 4 neV enter the hexahedral reflecting neutron guide with vertical glass walls 50 cm high. The UCNs accelerate as they move along the neutron guide in the Earth's gravitational field. The change in energy equals 1.026 neV/cm. The second filter — an analyzer with a transmission maximum near 127 neV — is located approximately 20 cm below the first one. For such a relative arrangement of the filters the neutrons with an initial energy of 107 neV are also transmitted by the second filter after they are accelerated in the gravitational field. The position of the analyzer filter can be varied along the vertical direction, making it possible to perform scanning over the energy and to measure the transmission of the system in a quite wide range of energies. The neutrons which have passed through the spectrometer are detected with a He^3proportional detector.

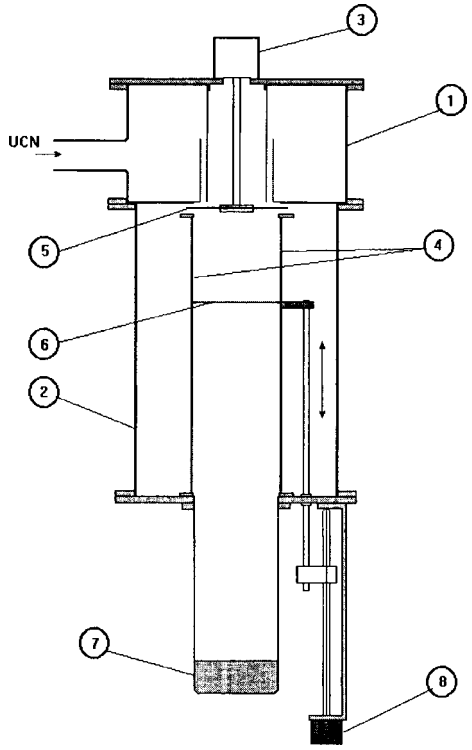

FIG. 2. Experimental arrangement: *1* — Entrance chamber, *2* — vacuum chamber, *3* — motor for rotating the filter, *4* — reflecting neutron guide, *5* — rotating filter-monochromator, *6* — analyzer filter, *7* — detector, *8* — stepping motor.

The interference filters were prepared by magnetron sputtering on silicon substrates 150 mm in diameter and 0.6 mm thick. A pair of materials was used to prepare the structure: the paramagnetic compound Ni(N) with a high scattering-amplitude density, and the alloy Ti/Zr with a virtually zero average value of ρb.

A special multilayer structure (more than 100 layers) located below the analyzer was used to suppress the background. This multilayer filter (superwindow) transmits UCNs but efficiently reflects neutrons with energies ranging from 200 to 700 neV.

The experimentally obtained scan curve had a half-width of the order of 6.6 neV. The count rate at the maximum was equal to 1.4 counts/s with a 0.12 counts/s background. When the filter was rotated, the background increased by approximately 0.02 counts/s, apparently because of scattering of the neutrons by the moving interlayer irregularities. Moreover, when the filter rotated, a small (2–5%) decrease of the area under the scan curve was observed.

For each position of the analyzer repeat measurements of the count rate were performed for the monochromator at rest and rotating, after which the analyzer was moved to the next point. The linear velocity of the region of the filter through which the UCNs passed was approximately 35 m/s. After scanning was completed, the shift of the average

position of the transmission function of the two filters with the monochromator rotating was calculated as

$$\delta\langle x\rangle = \frac{\sum_i x_i n_i'}{\sum_i n_i'} - \frac{\sum_i x_i n_i}{\sum_i n_i}, \tag{5}$$

where n_i' and n_i are the count rates in the position x_i for filters rotating and at rest, respectively. The data obtained for the shift in separate measurements (scans) were averaged over the entire series of measurements. The direction of rotation was changed periodically. In two series differing by the position of the superwindow, five and twelve separate measurements, respectively, were performed.

The measured shift was equal to -0.100 ± 0.031 cm $(+)$ and -0.158 ± 0.046 cm $(-)$ for the first series and -0.060 ± 0.019 cm $(+)$ and -0.084 ± 0.025 cm $(-)$ for the second series. The symbols in parentheses denote the two rotation directions. A negative shift corresponds to an increase in neutron energy. Averaging over the rotation direction gives the values -0.118 ± 0.024 cm and -0.069 ± 0.014 cm for the two series. A sufficient number of measurements performed in the second series made it possible to analyze how well the individual data corresponded to a normal distribution, with the result $\chi^2=1.11$ for one degree of freedom.

To switch from the shift of the average experimental curve to the shift of the spectrum itself it is necessary to take account of the background fraction under the scan curve. The energy shifts obtained in this manner are $\Delta E_1=+0.150\pm0.032$ and $\Delta E_2=+0.090\pm0.018$ neV; only the statistical error was taken into account in determining the background.

Figure 3 shows the area-normalized scan curves for the second series. The background was subtracted out beforehand.

The experimental conditions were somewhat different for the two series. In the first series the superwindow was in a fixed position at the bottom of the neutron guide. In the second series the superwindow was connected to the analyzer filter and moved together with the filter during scanning. Subsequent analysis showed that a small spurious effect due to broadening of the line accompanying rotation of the filter was possible in the first case. This effect was taken into account as a methodological error. Ultimately it was found that for the two series the shifts of the average neutron energy occurring when the filter was put into rotation were $\Delta E_1=+0.150\pm0.032$ (stat) ±0.025 (meth) and $\Delta E_2=+0.090\pm0.018$ (stat) neV, while the average is $\Delta E=+0.100\pm0.016$ neV.

CONTROL EXPERIMENT AND SPURIOUS EFFECTS

A special control experiment was performed to rule out the hypothesis that the neutron energy can change as a result of an interaction with the rotating multilayer structure. In this experiment the monochromator was stationary and was placed directly above a rotating filter. The filter was specially prepared for the control experiment. The transmission line of this filter coincided with the transmission line of the monochromator filter but it was two times wider. The experimental and analysis procedures were the same as in the main experiment. The data from individual measurements correspond to a

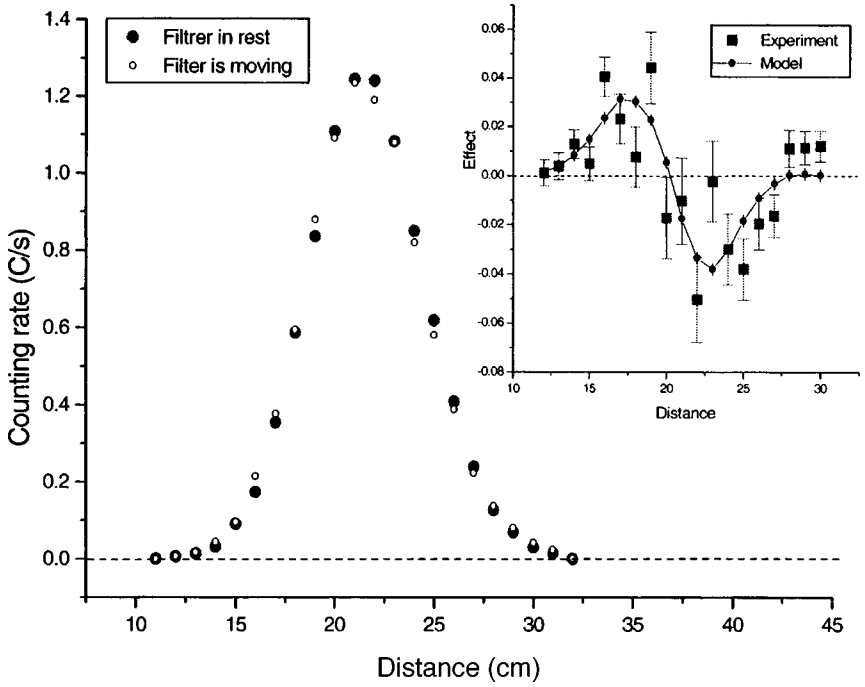

FIG. 3. Normalized scan curves for the second series. The errors are not indicated because when plotted they are less than the size of a dot. Inset: Differential effect, the difference of the scan curves.

normal distribution ($\chi^2 = 1.40$). No changes in energy were found when the filter was put in motion: $\Delta E = +0.009 \pm 0.024$ neV . However, subsequent analysis showed that spurious effects can in principle exist, and their presence is not ruled out by the control experiment. Only further experiments can clarify the situation.

POSSIBLE INTERPRETATION OF THE RESULTS

It is interesting to estimate the correction to the dispersion law under the assumption that the observed effect is indeed due to a shift of the resonance. Since the potential of the inner Ti/Zr film is close to zero, it is natural to expect that the effect is due to a change in $k_\perp$ in the outer Ni(N) layers. It was found from the solution of the quantum problem of the transmission of a filter that to explain the observed effect this change must constitute $(\Delta k_\perp)_{\text{exp}} \approx -i \cdot 1.2 \times 10^3$ cm^{-1} ($\Delta k_\perp / k_\perp \approx 1.5 \times 10^{-3}$) when the filter is put in motion. This is close to the estimates following from Ref. 9.

CONCLUSIONS

An experiment to search for a shift in the resonance line in an interference filter as a result of the motion of the filter parallel to its surface showed an effect that can be interpreted as a change in the energy of the neutrons which have passed through the filter. The statistical reliability of the result is quite high. We did not find any spurious effects capable of explaining the result, though such a possibility cannot be completely ruled out at the present time.

This experiment was supported by the Russian Fund for Fundamental Research under Grant 96-02-16469.

We thank B. G. Erozolimskiĭ for assistance and helpful discussions during the experiment in Grenoble and A. V. Kozlov for completing the analytical solution of the problem of the transmission of complex interference filters. We thank all our colleagues for helpful discussions and their interest in this work.

[a)]e-mail: frank@nf.jinr.ru

---

[1] L. I. Foldy, Phys. Rev. **67**, 107 (1950).
[2] L. Koester, Springer Tracts of Modern Phys. **80**, 1 (1977).
[3] V. K. Ignatovich, *The Physics of Ultracold Neutrons* [in Russian], Nauka, Moscow, 1986.
[4] R. Golub, D. Richardson, and S. K. Lamoreux, *Ultra-Cold Neutrons*, Adam Hilger, Bristol.
[5] V. F. Sears, Phys. Rep. **82**, 1 (1982).
[6] M. Warner and J. E. Gubernatis, Phys. Rev. B **32**, 6347 (1985).
[7] M. Arif, H. Kaiser, S. A. Werner *et al.*, Phys. Rev. A **31**, 1203 (1985).
[8] E. Fermi, Nuovo Cimento **11**, 157 (1934).
[9] V. G. Nosov and A. I. Frank, Phys. Rev. A **55**, 1129 (1997).
[10] A. I. Frank and V. G. Nosov, Yad. Fiz. **58,** 453 (1995) [Phys. At. Nucl. **58**, 402 (1995)].
[11] I. M. Frank, Usp. Fiz. Nauk **161,** 109 (1991) [Sov. Phys. Usp. **34**, 988 (1991)].
[12] V. A. Horn, A. Zeilinger, A. G. Klein, and G. I. Opat, Phys. Rev. A **28**, 1 (1983).
[13] A. A. Seregin, Zh. Éksp. Teor. Fiz. **73,** 1634 (1977) [Sov. Phys. JETP **46**, 859 (1977)].
[14] K.-A. Steinhauser, A. Steyerl, H. Scheckenhofer, and S. S. Malik, Phys. Rev. Lett. **44**, 130 (1980).
[15] A. Steyerl, H. Nagel, F. Schriber *et al.*, Phys. Lett. A **116**, 347 (1986).

Translated by M. E. Alferieff

Observation of truly cold fragmentation of a heavy nucleus

A. A. Goverdovskiĭ,[a)] V. V. Ketlerov, V. F. Mitrofanov, Yu. B. Ostapenko, and V. A. Khryachkov

Russian State Science Center ''Physics and Power Engineering Institute,'' 249020 Obninsk, Russia

(Submitted 20 April 1998)
Pis'ma Zh. Éksp. Teor. Fiz. **67**, No. 10, 752–754 (25 May 1998)

The results of a careful investigation of the mass-energy-charge correlations of the fragments produced by fission of thorium-232 by 5 MeV neutrons are presented. The phenomenon of truly cold fragmentation of a thorium nucleus into tellurium-134 and strontium-99 in the quantum ground states is observed. It is shown that the reaction energy is completely exhausted by the kinetic energy of the fragments in their mutual field. © *1998 American Institute of Physics.*
[S0021-3640(98)00710-5]

PACS numbers: 25.85.Ec, 25.70.Mn, 27.90.+b

During nuclear fission, excited deformed fragments are produced which emit a large number of neutrons and gamma rays. The portion δQ of the reaction energy expended on the accompanying emissions is quite high, reaching on the average 30 MeV per fission event. The ''boiling'' fragments fly apart in their mutual Coulomb field with relativistic velocities, acquiring momenta up to 3 GeV/c. The experimentally observed kinetic energy E_k of the fragments is determined, first and foremost, by their deformation β at the moment of scission of the system. In principle, E_k is limited from above by the total reaction energy Q. The boundary condition $E_k=Q$ or $\delta Q=0$ is of special interest, since the corresponding scission configuration consists of two nuclei in quantum ground states. Fissioning with $E_k=Q$ has been termed truly cold fragmentation (TCF).[1] All known attempts to observe TCF experimentally have been unsuccessful so far, primarily because of the extremely low probability of scission in the compact configurations realized on the initial part of the descent of the system to the scission point. For example, in the case of the fissioning of ^{233}U or ^{235}U by thermal neutrons[2,3] the values of E_k corresponding to free energies $\delta Q=2-3$ MeV can be attained only with relative yields of less than 10^{-7}. No TCF events were detected, even at a level of 10^{-9}, over a period of one year of continuous spectrometric investigations of fragments of spontaneous fission of ^{252}Cf (Ref. 4). As a result, on the one hand (technically), it was no longer reasonable to collect more statistical samples, since on account of target activity limitations this could be done only by increasing the exposure time. On the other hand (conceptually), it becomes questionable whether it is possible in principle to obtain sufficiently compact scission figures in a cold nucleus.

The present experiment was based on the following basic assumptions. First, the

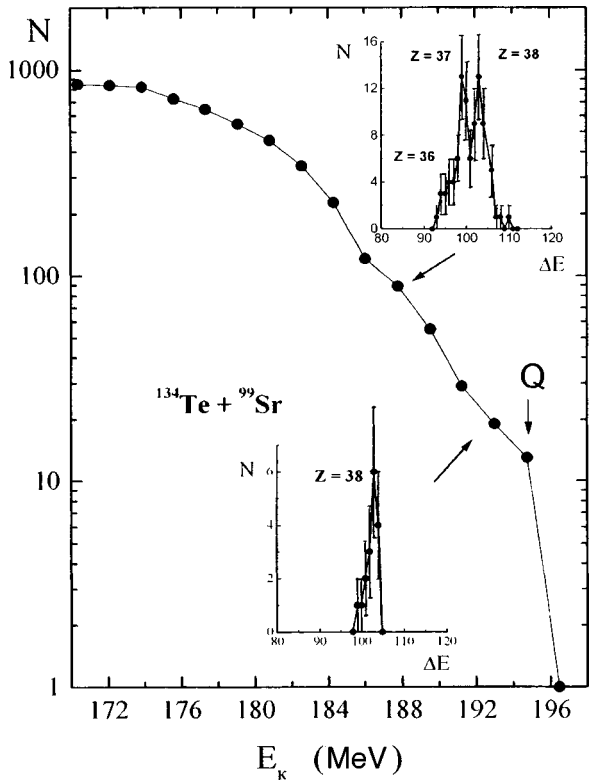

FIG. 1. Distribution over the total kinetic energy E_k of thorium fission fragment pairs with masses of 134 and 99 amu. Insets: Distribution of light fragments over the parameter ΔE — the specific ionization power of a fragment near the Bragg peak. Q is the reaction energy.

products of TCF must be sought among pairs of nuclei which possess a high stiffness with respect to shape variations, which in turn is provided by nucleon-shell effects. Second, after overcoming the outer saddle point the fissioning system must possess sufficient free energy for formation of the required compact configuration. Accordingly, the fragments produced during fissioning of ^{232}Th by 5 MeV neutrons were chosen as the object of investigations. The fragment pair ^{134}Te + ^{99}Sr, belonging to the first standard Brosa channel,[5] possesses the maximum kinetic energy. The theory of Ref. 6 predicts a spherical shape for tellurium on account of the extremely strong spherical shells — the neutron shell $N=82$ and the close-to-tellurium proton shell $P=50$. At the same time the light fragment ^{99}Sr of the pair should be quite stiff on account of the deformed shells $N=60$, $P=38$.[6] The predicted deformation of strontium equals 0.38 (in units of β). An elementary calculation of the Coulomb interaction between the indicated spheroids shows that in order for the condition $E_k=Q$ to be satisfied the distance between their surfaces at the moment just before they start to fly apart should equal about 2 fm, which is quite realistic.[7]

This work was performed in the neutron beam of the KG-2.5 accelerator at the Physics and Power Engineering Institute. Neutrons were generated in the reaction

$D(d,n)^3He$ in a solid titanium–deuterium target. The thorium fission product spectrometer was constructed on the basis of a double ionization chamber with Frisch grids[8] and was equipped with a pulse-shape digitizer. The spectrometric target, consisting of thorium tetrafluoride on a substrate transparent to the fragments, was secured on the chamber cathode. The fragment masses and energies were determined by the pair energy method, which is absolutely correct for neutron-free binary fission. The nuclear charges of the fragments were extracted by Bragg-spectrometry methods.[9] The computer system for acquisition, storage, and processing of the experimental data made it possible to analyze the data for one event after another using a series of criteria of correctness. The irradiation duration was equal to approximately five calendar months, during which approximately two million digital oscillograms of pulses from thorium fission products (approximately 10 GB of memory) were accumulated.

The most significant and important result of this work is presented in Fig. 1. For the pair of fragments with mass ratio 134/99 the kinetic energy distribution cuts off at a point corresponding exactly to the maximum admissible energy for the pair $^{134}Te + {}^{99}Sr$ ($E_k = Q$). The distributions of the events over the so-called Bragg parameter (ΔE), which show an unique correspondence to the nuclear charge of the heavy ion — light fragment, are shown in the insets. Leaving aside the details of the calibrations performed, we note that the character of the charge spectrum changes fundamentally 6–7 MeV from the limit $E_k = Q$. Production channels not only for strontium but also rubidium and krypton with the corresponding heavy fragment pairs, open up. Apparently, we do indeed observe at the cutoff point of the energy spectrum the only possible pair of fragments $^{134}Te + {}^{99}Sr$ with the full kinetic energy, equal to the reaction energy. Therefore it is obvious that they are products of truly cold fragmentation of the thorium nucleus.

The observation of TCF was found to be possible only when the fissioning system was preheated by a fast neutron.

This work was supported by the President's Fund of the Russian Federation under Grant 96-15-96938.

[a)]e-mail: gaa@ippe.rssi.ru

[1] F. Gonnenwein, in *The Nuclear Fission Process*, edited by C. Wagemans, CRC Press, London, 1992, Ch. 8, p. 287.
[2] U. Quade, K. Rudolph, S. Skorka *et al.*, Nucl. Phys. A **487**, 1 (1988).
[3] V. A. Khryachkov, A. A. Goverdovskiĭ, B. D. Kuz'minov *et al.*, Yad. Fiz. **53,** 621 (1991) [Sov. J. Nucl. Phys. **53**, 387 (1991)].
[4] A. Moller, M. Croni, F. Gonnenwein *et al.*, in *Proceedings of the International Conference on Large-Scale Collective Motion of Atomic Nuclei*, Brolo, Italy, October 1996, World Scientific, p. 203.
[5] U. Brosa, S. Grossmann, and A. Muller, Phys. Rep. **197**, 167 (1990).
[6] B. D. Wilkins, E. P. Steinberg, and R. R. Chasman, Phys. Rev. C **14**, 1831 (1976).
[7] F. Gonnenwein and B. Borsig, Nucl. Phys. A **530**, 27 (1991).
[8] V. A. Khriachkov, A. A. Goverdovski, V. V. Ketlerov *et al.*, Nucl. Instrum. Methods Phys. A **394**, 261 (1997).
[9] A. Oed, P. Geltenbort, and F. Gonnenwein, Nucl. Instrum. Methods **205,** 451 (1983).

Translated by M. E. Alferieff

Generation of sub-Poisson light by a single-mode two-level laser with incoherent pumping

A. V. Kozlovskiĭ and A. N. Oraevskiĭ
P. N. Lebedev Physics Institute, Russian Academy of Sciences, 117924 Moscow, Russia

(Submitted 11 March 1998)
Pis'ma Zh. Éksp. Teor. Fiz. **67**, No. 10, 755–759 (25 May 1998)

It is found that the steady-state radiation of a single-mode two-level laser with incoherent pumping can be in a nonclassical (sub-Poisson) state if the spontaneous decay rate is less than the cavity loss rate and the pumping rate. The optimal conditions of squeezing are found. Multiple squeezing of the radiation intensity is possible in a transient lasing regime. © *1998 American Institute of Physics.*
[S0021-3640(98)00810-X]

PACS numbers: 42.50.Dv

Several methods have now been found for producing a state of the electromagnetic field for which the photon number fluctuations are below the shot-noise level (sub-Poisson light). In Refs. 1–3 it was proposed that a single-mode laser with regularized pumping be used for this purpose. In Refs. 4 and 5 the atomic coherence of the active medium is used to obtain photon-number-squeezed light. As was shown in Refs. 6–13, multilevel schemes of a single-mode laser can also be a source of squeezed light in the case of both coherent and incoherent pumping. In Refs. 14 and 15 it is pointed out that sub-Poisson light can be generated with a multimode laser. In Ref. 16 the conditions for producing a transient squeezed state of the generated radiation were found for a single-mode two-level laser with incoherent pumping.

Squeezing of radiation under steady-state conditions is absent in the single-mode two-level lasers studied in Refs. 12, 17, and 16.

In the present letter an analysis is made of the dynamics of the quantum-statistical properties of laser radiation using the reduced density operator of the system atom + field in a basis consisting of the Fock states of the field. The analysis is valid for any possible ratios of the values of the parameters characterizing the incoherent-pumping and dissipation processes.

To analyze the quantum stochastic dynamics of a two-level one-atom laser we shall use a reduced density operator of the system atom + single-mode field in a basis consisting of the Fock states

$$\rho(t)=\sum_{i,j=\uparrow,\downarrow}\sum_{n,m=0}^{\infty}\rho_{n,i;m,j}(t)\ |i\rangle|n\rangle\langle m|\langle j|. \tag{1}$$

In the interaction representation and the Born–Markov approximation[18,19] the reduced density operator (1) of the system atom + field interacting with a reservoir satisfies the Liouville equation

$$\frac{\partial\rho}{\partial t}=-i\Delta\left[\frac{\sigma^z}{2},\rho\right]-ig[(a^+\sigma^-+\sigma^+a),\rho]+\frac{\gamma}{2}(n_T+1)(2a\rho a^+-a^+a\rho-\rho a^+a)$$
$$+\frac{\gamma}{2}n_T(2a^+\rho a-aa^+\rho-\rho aa^+)+\frac{\Gamma}{2}(N_T+1)(2\sigma^-\rho\sigma^+-\sigma^+\sigma^-\rho-\rho\sigma^+\sigma^-)$$
$$+\frac{\Gamma}{2}N_T(2\sigma^+\rho\sigma^--\sigma^-\sigma^+\rho-\rho\sigma^-\sigma^+)+\frac{P}{2}(1-p)(2\sigma^-\rho\sigma^+-\sigma^+\sigma^-\rho$$
$$-\rho\sigma^+\sigma^-)+\frac{P}{2}p(2\sigma^+\rho\sigma^--\sigma^-\sigma^+\rho-\rho\sigma^-\sigma^+), \tag{2}$$

where the atomic operators and the detuning of the cavity from the atomic frequency are

$$\sigma^-=|\downarrow\rangle\langle\uparrow|,\quad \sigma^+=|\uparrow\rangle\langle\downarrow|,\quad \sigma^z=|\uparrow\rangle\langle\downarrow|-|\downarrow\rangle\langle\uparrow|,\quad \Delta=\omega_a-\omega_c. \tag{3}$$

The atomic polarization operators σ^+ and σ^- and the inversion operator σ^z satisfy the relations

$$2\sigma^{\mp}\sigma^{\pm}=(1\mp\sigma^z),\quad \sigma^z\sigma^z=1. \tag{4}$$

The average numbers of photons and phonons of the field and atomic reservoirs, respectively, in thermodynamic equilibrium at temperature T that appear in Eq. (2) are

$$n_T=(\exp(\hbar\omega_c/kT)-1)^{-1},\quad N_T=(\exp(\hbar\omega_a/kT)-1)^{-1}. \tag{5}$$

The quantities γ, Γ, and P are, respectively, the loss rate of the field at the mirrors, the spontaneous emission rate, and the incoherent pumping rate, and g is the atom–field interaction constant. The parameter p characterizes the steady-state inversion $\langle\sigma^z\rangle_0=2p-1$ of the atomic states that is maintained by pumping in the absence of an interaction with the field.

Using Eq. (1), the orthonormality of the basis of Fock states, and Eq. (4) we find from Eq. (2) the following system of coupled differential equations for the elements of the density matrix:[20]

$$\rho_{1n,m}(t)\equiv\langle\uparrow|\rho_{n,m}|\uparrow\rangle+\langle\downarrow|\rho_{n,m}|\downarrow\rangle,\quad \rho_{2n,m}(t)\equiv\langle\uparrow|\rho_{n,m}|\uparrow\rangle-\langle\downarrow|\rho_{n,m}|\downarrow\rangle,$$
$$\rho_{3n,m}(t)\equiv\langle\uparrow|\rho_{n,m}|\downarrow\rangle,\quad \rho_{4n,m}(t)\equiv\langle\downarrow|\rho_{n,m}|\uparrow\rangle. \tag{6}$$

The $4\times(n_{\max}+1)\times(n_{\max}+1)$ system of equations for the components (6) was solved numerically. In the general case, the field is initially in an arbitrary mixed state, while the atom is in a state which is a superposition of the upper and lower states. Therefore the density matrix of an atom and field which are noninteracting at time $t=0$ is

$$\rho(0)=\rho_a\otimes\rho_f,\quad \rho_a=\left[\cos\frac{\theta}{2}|\uparrow\rangle+\sin\frac{\theta}{2}e^{i\varphi}|\downarrow\rangle\right]\left[\cos\frac{\theta}{2}\langle\uparrow|+\sin\frac{\theta}{2}e^{-i\varphi}\langle\downarrow|\right],$$
$$\rho_f=\sum_{n,m=0}^{\infty}c_nc_m^*|n\rangle\langle m|. \tag{7}$$

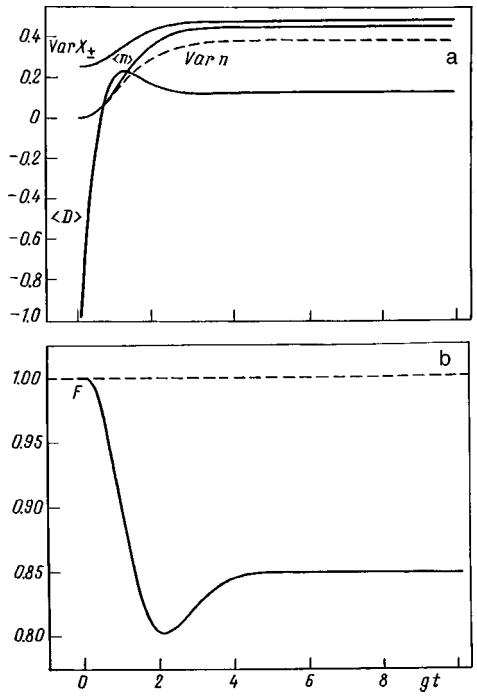

FIG. 1. a) Average number $\langle n(t)\rangle$ of photons, fluctuations (variance) Var $n(t)$ of the photon number, average inversion $\langle D(t)\rangle$, and fluctuations (variance) Var $X_{\pm}(t)$ of the quadratures of the laser field for the initial state consisting of the field in a coherent vacuum state and the atom in the lower level with $\gamma=1.4g$, $\Gamma\ll\gamma$, $P=1.4g$, $p=1$, $\Delta=0$, $T=0$. b) Fano factor $F=\mathrm{Var}(n)/\langle n\rangle$.

Grouping together the matrix elements of the form (6), we find that the average number of photons, the average inversion, the photon fluctuations (variance), and the average field are given by

$$\langle n(t)\rangle=\mathrm{Tr}(\rho(t)a^{+}a)=\sum_{n=0}^{\infty} n\rho_{1n,n}(t),\quad \langle D(t)\rangle=\mathrm{Tr}(\rho(t)\sigma^{z})=\sum_{n=0}^{\infty}\rho_{2n,n}(t),$$

$$\mathrm{Var}(n(t))\equiv\langle(\Delta n(t))^{2}\rangle=\sum_{n=0}^{\infty}(n-\langle n(t)\rangle)^{2}\rho_{1n,n}(t), \tag{8}$$

$$\langle a^{+}(t)\rangle=\sum_{n=0}^{\infty}\sqrt{n+1}\rho_{1n,n+1}(t),\quad \langle a(t)\rangle=\sum_{n=1}^{\infty}\sqrt{n}\rho_{1n,n-1}(t).$$

The variances of the conjugate quadratures $X_{+}(t)=(a^{+}(t)+a(t))/2$ and $X_{-}(t)=(a^{+}(t)-a(t))/2i$ can be expressed in terms of the matrix elements of the density operator as

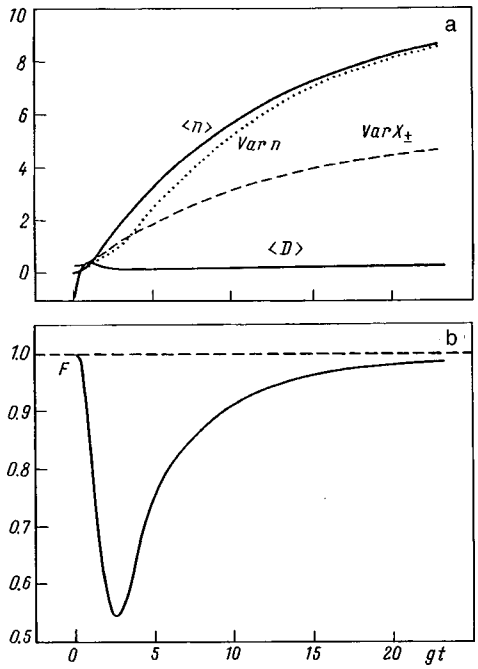

FIG. 2. Same as Fig. 1 with $\gamma=0.1g$, $\Gamma\ll\gamma$, $P=2g$, $p=1$, $\Delta=0$, $T=0$.

$$\langle(\Delta X_{\pm})^2\rangle=\frac{1}{4}\Bigg[\sum_{n=0}^{\infty}(2n+1)\rho_{1n,n}(t)\pm\sum_{n=2}^{\infty}\sqrt{n(n-1)}\rho_{1n,n-2}(t)$$
$$\pm\sum_{n=0}^{\infty}\sqrt{(n+1)(n+2)}\rho_{1n,n+2}(t)\mp\Bigg(\sum_{n=0}^{\infty}\sqrt{n+1}\rho_{1n,n+1}(t)$$
$$\pm\sum_{n=1}^{\infty}\sqrt{n}\rho_{1n,n-1}(t)\Bigg)^2\Bigg]. \tag{9}$$

As the initial state of the field at $t=0$ we used both a coherent vacuum state and a chaotic thermal state with an average number of photons corresponding to the optical radiation range $\omega_a\sim10^{14}$ s^{-1} at temperature $T\sim300$ K. A numerical investigation of the system (2) in the representation (6) with different parameters of the laser showed that the steady state of the laser possesses sub-Poisson photon-number statistics in the case when the spontaneous emission rate $\Gamma<g,\gamma$ (see Fig. 1). The maximum degree of squeezing of the photon number fluctuations occurs for $\Gamma\ll g,\gamma$ for $T=0$ K and equals 15% (see Fig. 2). With increasing $\Gamma\to\gamma$, the degree of squeezing decreases, and for $\Gamma>\gamma$ the radiation passes into a super-Poisson state. The value of the pumping parameter p strongly influences the steady-state statistics of the radiation; the degree of squeezing is greatest for $p=1$ and decreases for $p<1$. The presence of detuning ($\Delta\neq0$) likewise has a negative effect on the degree of squeezing. The optimal cavity loss rate γ and the pump rate P with respect to the coupling constant g are $\gamma=P\approx1.4g$ for $p=1$ and $\Delta=0$, for which the Fano factor ($F=\mathrm{Var}(n)/\langle n\rangle$) is $F=0.85$ at temperatures $T<100$ K, $\omega_a=10^{14}$. As

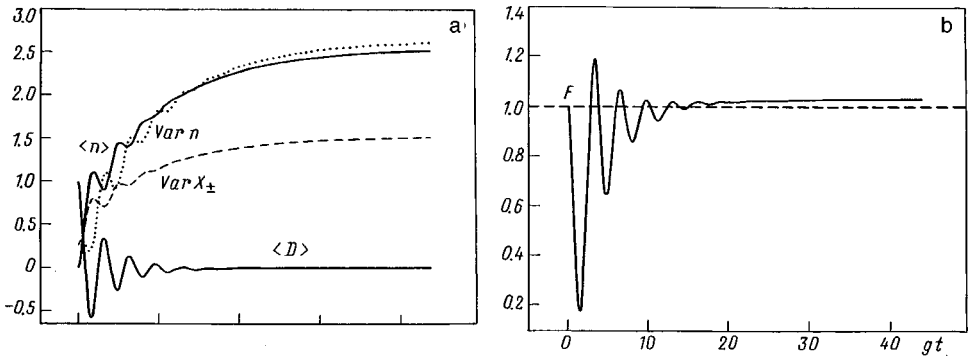

FIG. 3. Same as Fig. 1 with $\gamma=0.1g$, $\Gamma\ll\gamma$, $P=0.5g$, $p=1$, $\Delta=0$, $T=0$, and the atom initially on the upper level.

one can see from Fig. 2, during the process leading to the establishment of steady-state lasing the laser radiation is in a state with nonclassical sub-Poisson photon statistics. The Fano factor can be sharply decreased by decreasing the cavity loss rate with respect to the pumping rate. Figure 2 shows the dynamics of the variation of the Fano factor for $\gamma=0.1g$, $P=2g$ for the case of lasing from a state with the field in a coherent vacuum state and the atom in the lower level. In this case the minimum value is $F_{\min}=0.54$ for $\langle n\rangle=1.43$. Therefore, generation of intense squeezed radiation is possible in the transient lasing regime. The degree of squeezing in the transient regime depends on the initial state. The highest degree of squeezing and the highest radiation intensity are obtained in the case when the atom is in the upper state while the field is in the coherent vacuum state. In this case, for example, for $\gamma=0.1g$ and $P=0.5g$, five-fold squeezing ($F_{\min}=0.19$) is achieved for $gt=1.8$ and $\langle n\rangle=1.2$ (Fig. 3).

The case studied above, where the coupling constant is much less than the spontaneous emission rate and is comparable in magnitude to the cavity loss and pump rates, is not characteristic for most known lasers. The indicated requirements are best met by a laser operating on transitions between highly excited states of Rydberg atoms, for which the coupling constant can reach $g\sim 10^6\ \mathrm{s}^{-1}$.

[1] Yu. M. Golubev and I. V. Sokolov, Zh. Éksp. Teor. Fiz. **87**, 408 (1984) [Sov. Phys. JETP **60**, 234 (1984)].
[2] Y. Yamamoto, S. Mashida, and O. Nilson, Phys. Rev. A **34**, 4025 (1986).
[3] C. Benkert, M. O. Scully, J. Bergou *et al.*, Phys. Rev. A **41**, 2756 (1990).
[4] C. Benkert and M. O. Scully, Phys. Rev. A **42**, 2817 (1990).
[5] L. Davidovich, J. Mod. Phys. **68**, 127 (1996).
[6] M. A. Marte, H. Ritsch, and D. F. Walls, Phys. Rev. Lett. **61**, 1093 (1988).
[7] T. A. B. Kennedy and D. F. Walls, Phys. Rev. A **40**, 6366 (1989).
[8] H. Ritsch, P. Zoller, C. W. Gardiner, and D. F. Walls, Phys. Rev. A **44**, 3361 (1991).
[9] H. Ritsch and P. Zoller, Phys. Rev. A **45**, 1881 (1992).
[10] H. Ralph and C. M. Savage, Phys. Rev. A **44**, 7809 (1991).
[11] D. L. Hart and T. A. B. Kennedy, Phys. Rev. A **44**, 4572 (1991).
[12] A. V. Kozlovskiĭ and A. N. Oraevskiĭ, Kvantovaya Élektron. (Moscow) **21**, 273 (1994).
[13] H.-J. Briegel, G. M. Meyer, and B. C. Englert, Phys. Rev. A **53**, 1143 (1996).
[14] A. V. Kozlovskiĭ, Zh. Eksp. Teor. Fiz. **104**, 2995 (1993) [JETP **77**, 393 (1993)].
[15] A. Eschmann and C. V. Gardiner, Phys. Rev. A **54**, 3373 (1996).
[16] G. M. D. D'Ariano, C. Macchiavello, and M. G. A. Paris, Phys. Rev. Lett. **73**, 3187 (1994).
[17] A. V. Kozlovskiĭ and A. N. Oraevskiĭ, Zh. Éksp. Teor. Fiz. **109**, 1524 (1996) [JETP **82**, 820 (1996)].

[18] M. Lax, *Fluctuations and Coherence Phenomena in Classical and Quantum Physics*, edited by M. Chretien, E. P. Gross, and S. Deser, Gordon and Breach, New York, 1968 [Russian translation, Mir, Moscow, 1974].
[19] C. W. Gardiner, *Handbook of Stochastic Methods*, edited by H. Haken, Springer-Verlag, Berlin, 1985 [Russian translation, Mir, Moscow, 1986].
[20] B. Daeubler, H. Risken, and L. Schoendorff, Phys. Rev. A **46**, 1654 (1992).

Translated by M. E. Alferieff

Experimental observation of optical diffraction radiation

I. E. Vnukov, B. N. Kalinin, G. A. Naumenko,[a)] D. V. Padalko,
A. P. Potylitsyn, and O. V. Chefonov
Institute of Nuclear Physics, 634050 Tomsk, Russia

(Submitted 6 April 1998)
Pis'ma Zh. Éksp. Teor. Fiz. **67**, No. 10, 760–764 (25 May 1998)

The optical diffraction radiation of ultrarelativistic electrons at the boundary of a conducting medium is observed experimentally. Backward diffraction radiation, which, like transition radiation, is emitted at the angle of specular reflection from the target, is detected. © *1998 American Institute of Physics.* [S0021-3640(98)00910-4]

PACS numbers: 41.60.Ap, 41.75.Ht

Theoretical investigations of diffraction radiation (DR), i.e., radiation arising during the motion of a charged particle near a conducting target, began more than 30 years ago.[1–4] The characteristics of DR were investigated in greater detail in Refs. 5–7, but until recently there were no experimental works on the DR of ultrarelativistic particles. At the same time, the DR of nonrelativistic electrons is widely used in microwave electronics.[8]

Millimeter-range DR in the forward direction for 150 MeV electrons passing through a circular opening was apparently first investigated experimentally in Ref. 9. However, in the experimental apparatus a mirror was present in the path of the electron beam, resulting in interference between the DR and the transition radiation (TR) generated in the mirror material, which contributed an uncertainty in the interpretation of the results. Optical-range DR has not been investigated experimentally up to now. At the same time optical DR can be an effective method of nonperturbative diagnostics of charged-particle beams with extremely small emittance.[10,11]

In a series of works[12,13] the backward transition radiation (BTR) was investigated experimentally in the optical range (reflection from a metal foil of the pseudophotons describing the field of a relativistic charged particle) and it was shown that optical TR can be used for highly accurate diagnostics of beams with Lorentz factors $\gamma \leqslant 200$.

By their very nature TR and DR are particular cases of a more general mechanism — so-called polarization radiation arising as a result of the dynamic polarization of a medium by relativistic electrons. Therefore it should be expected that by analogy to BTR optical DR will be generated near the angle of specular reflection as a charged particle travels near an inclined metal target. A theory of DR accompanying the passage of a charged particle near an inclined half plane consisting of an ideally conducting material was developed in Ref. 3. It can be shown[7] that in this case the angular distribution of DR for ultrarelativistic particles has two sharp peaks, one in the same direction as the primary beam and the other in the direction of its specular reflection. According to the theory of

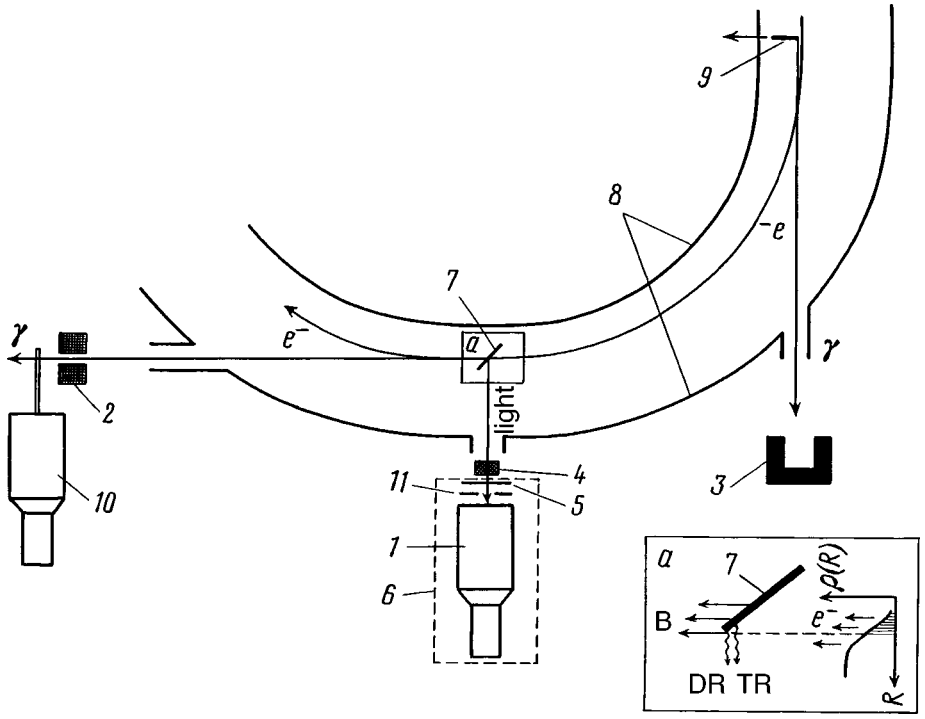

FIG. 1. Arrangement of the experimental apparatus: *1* — Photomultiplier, *2,11* — collimators, *3* — graveyard, *4* — mirror, 5 — light filter, *6* — detection system, *7* — target, *8* — accelerator chamber, *9* — scraper, *10* — scintillation counter.

Ref. 3, the maximum value of the spectral-angular distribution of the DR intensity in the direction of specular reflection can be expressed in terms of the analogous characteristic of the TR:

$$\frac{d^2W_{\max}^{\mathrm{DR}}}{d\omega d\Omega}=\exp\left(-\frac{4\pi a}{\gamma\lambda}\right)\frac{d^2W_{\max}^{\mathrm{TR}}}{d\omega d\Omega}. \tag{1}$$

Here a is the distance between the particle trajectory and the target edge, λ is the wavelength of the DR, $d^2W_{\max}^{\mathrm{TR}}/d\omega d\Omega=\alpha\gamma^2/4\pi^2$, and α is the fine-structure constant.

In contrast to optical TR the spectral distribution of the DR intensity depends explicitly on λ. We employed this factor to observe the optical DR of ultrarelativistic electrons in our experiment.

The experiment was performed on the internal beam of the Tomsk synchrotron. To decrease the contribution from the scattered synchrotron radiation the measurements were performed with 200 MeV electrons briefly ($\sim$20 μs) dumped on the target. The dumping was performed at a section of the accelerator where the magnetic field was increasing. The spiral pitch of the the electron trajectories was equal to 40 μm. The angular divergence of the electron beam was $\sigma_\theta=2.3$ mrad.

Figure 1 shows a diagram of the experimental apparatus for detecting optical-range DR. A 1-mm-thick polished aluminum target *7* was placed on an $X-Y$ goniometer in a

rectilinear section of the accelerator. In the experiment the bremsstrahlung in the forward direction was detected with a scintillation counter *10*, and the optical radiation was detected in the specular-reflection geometry with the detector system *6* at an angle of 90° with respect to the direction of the primary electrons. The collimations (collimators *2*, *11*) of the bremsstrahlung and optical beams were 1.5 and 1.16 mrad, respectively. The inset (a) shows schematically the electron flux distribution $\rho(R)$ over the radius R in the region of the target. The shaded region corresponds to the electrons that contribute to the transition radiation and to the bremsstrahlung.

To a first approximation the intensity I_{BTR} of the backward transition radiation of the electron beam, like the bremsstrahlung intensity I_{B}, is determined by the number of electrons which have passed through the target. In this case a strict proportionality should exist between the bremsstrahlung and the BTR:

$$I_{\mathrm{BTR}} = \mathrm{const} \cdot I_{\mathrm{B}}. \tag{2}$$

A scintillation counter was chosen to detect the bremsstrahlung because the time constant of an absolute total-absorption detector (Gauss quantometer) is much longer than the dumping time of the electrons on target. The bremsstrahlung spectrum remains virtually unchanged upon small changes in the orientation angle of the target, so that the use of a scintillation counter for monitoring the bremsstrahlung yield does not introduce any systematic errors. The detection system *6* for detecting optical radiation consists of a photomultiplier *1*, an interchangeable light filter *5*, and a collimator *11*. An FÉU-110 unit with photocathode photosensitivity 5.5×10^{-5} A/lm was used as the photomultiplier. The spectral sensitivity range of the photocathode was 300–900 nm.

To decrease the background the detection system *6* was taken out of the plane of the electron orbit with the aid of a mirror *4* and arranged vertically. A thick target *9* — the absorber (scraper) — was placed in the preceding rectilinear section. The target could move in the radial direction, ''cutting off'' a portion of the electrons that could strike the main target. The bremsstrahlung beam from the scraper was absorbed in the graveyard *3*.

With the scraper removed all electrons strike the target *7*. The bremsstrahlung and transition radiation yields will then be maximum. The number of electrons passing outside the target near its edge, which determine the yield of the diffraction radiation, will also be maximum. By covering a portion of the electron beam with the scraper we decrease to a larger extent the bremsstrahlung and transition radiation yields, while the diffraction radiation yield does not decrease as rapidly.

As we have said, the backward TR is concentrated in a narrow range of angles near the direction of specular reflection. Figure 2 shows the orientational dependences of the optical radiation intensity with the target rotating around a vertical axis with different positions of the scraper. The width of the orientational dependences is determined by the divergence of the electron beam, the angular aperture of the detector, and the intrinsic divergence of the TR and DR. The angle $\theta = 0$ in Fig. 2 corresponds to the specular-reflection geometry. Curve *1* was measured with the scraper removed, in which case the TR makes the main contribution to the optical radiation. The same curve obtained with a small scan step is shown in the inset (a). Despite the large divergence of the electron beam, one can see in the figure the splitting of the peak of the orientational dependence that is characteristic for TR ($\Delta\theta \sim \gamma^{-1} = 2.5$ mrad). The curve *2* corresponds to the position of the scraper at 1 mm (Fig. 3). In this position a large portion of the electron

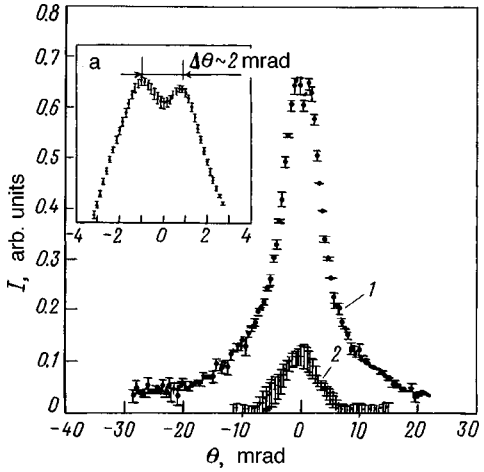

FIG. 2. Orientational dependences of the intensity of optical radiation. *1* — Scraper removed, *2* — scraper position at 1 mm.

beam is ''cut off'' by the scraper and does not reach the target: Therefore the DR can make a substantial contribution to the radiation investigated. According to Ref. 7, the angular distribution of the DR is unimodal, i.e., it does not split into two peaks.

For a detailed analysis of the DR contribution, we performed measurements of the scraper dependences (the dependence of the radiation yield on the radial position of the scraper) for bremsstrahlung and optical radiation in the specular-reflection geometry.

Figure 3 shows the scraper dependence obtained with a SS-1 blue light filter with transmission interval $\lambda \approx 350-500$ nm placed in front of the photomultiplier. The derivatives of these dependences, characterizing the differential yield of the optical radiation,

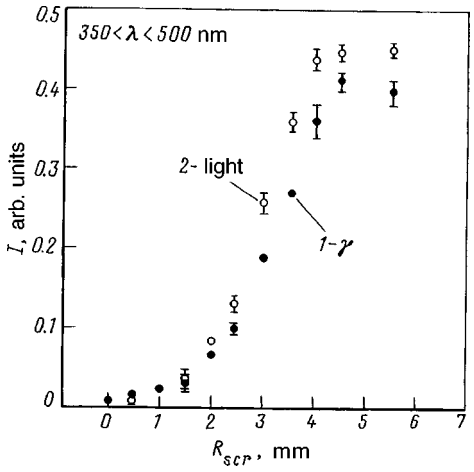

FIG. 3. Scraper dependences of the bremsstrahlung (*1*) and optical radiation (*2*) intensities.

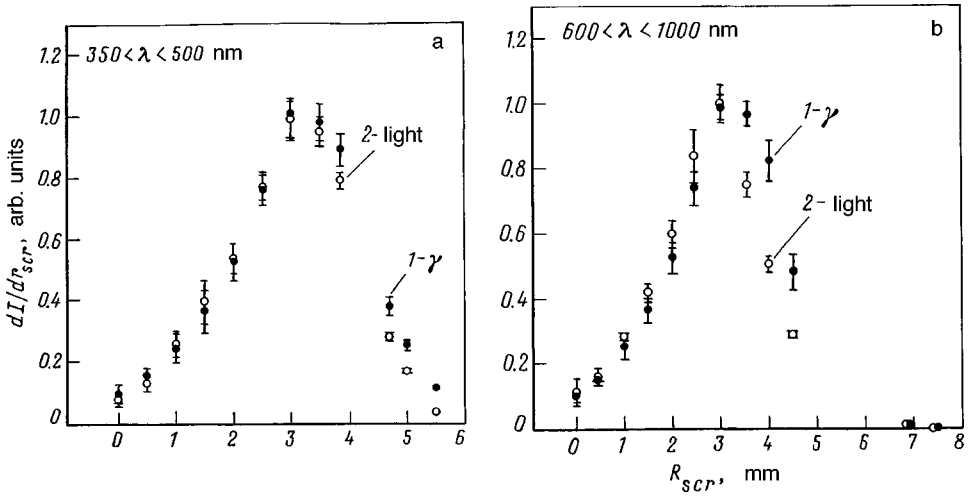

FIG. 4. Derivatives of the scraper dependences of the radiation intensity. a — $\lambda \approx 350-500$ nm, b — $\lambda \approx 600-1000$ nm. *1* — Bremsstrahlung, *2* — optical radiation.

are more informative. The derivatives of curves *1* and *2* (Fig. 3) were calculated by the methods of nonparametric statistics and are presented in Fig. 4a.

According to Eq. (2), in the absence of DR the curves *1* and *2* would be identical to within a constant factor. Let us consider the contribution that DR should make to the ratio of these dependences. When an electron passes near the target, the effective impact parameter $\bar{a}$ for DR generation (the effective distance between the electron trajectory and the target edge), determined by the characteristic transverse size of the field of virtual photons with wavelength λ, can be written, according to Eq. (1), as

$$\bar{a} \sim \gamma\lambda/4\pi. \tag{3}$$

The DR contribution should shift curve *2* (Fig. 4a) in our reference system to a scraper position at a smaller radius, which we in fact observe in the experiment. We note that under the conditions of a cyclic accelerator this shift is determined by, but does not equal, $\bar{a}$. The displacement of the centroid of curve *2* relative to curve *1* is 110 ± 35 μm.

At the same time, one can see from Eq. (3) that the effective impact parameter increases with λ and therefore the shift of curve *2* relative to curve *1* should also increase.

Figure 4b shows similar curves measured with an orange OS-14 light filter ($\lambda \approx 600-1000$ nm). The shift in the centroid of the curves in this case was equal to 230 ± 27 μm, i.e., when the average value of λ increased by approximately a factor of 1.8 (when the spectral sensitivity range of the photomultiplier is taken into account), the shift in the centroid increased by a factor of 2.1 ± 0.7.

In the absence of a DR contribution there is no reason for such a wavelength-dependent shift. It can be asserted on the basis of these experimental data that we have detected *optical backward diffraction radiation* of an ultrarelativistic electron. Further

analysis of the results obtained will make it possible to obtain quantitative estimates of the DR yield and to compare with the characteristics of the well-studied optical TR, which we plan to do in a separate paper.

This work was supported in part by the Russian Fund for Fundamental Research under Grants 98-02-17-994 and 96-02-16819a.

[a)]Corresponding author, e-mail: naumenko@npi.tpu.ru

[1] Yu. N. Dnestrovskiĭ and D. P. Kostomarov, Dokl. Akad. Nauk SSSR **124**, 1026 (1959) [Sov. Phys. Dokl. **4**, 158 (1959)].
[2] Yu. N. Dnestrovskiĭ and D. P. Kostomarov, Dokl. Akad. Nauk SSSR **116**, 377 (1957) [Sov. Phys. Dokl. **2**, 442 (1957)].
[3] A. P. Kazantsev and G. I. Surdutovich, Dokl. Akad. Nauk SSSR **147**, 74 (1962) [Sov. Phys. Dokl. **7**, 990 (1963)].
[4] D. M. Sedrakyan, Izv. Akad. Nauk SSR Ser. Fiz. Mat. Nauk **17**, 103 (1964).
[5] B. M. Bolotovskiĭ and G. V. Voskresenskiĭ, Usp. Fiz. Nauk **88**, 209 (1966) [Sov. Phys. Usp. **9**, 73 (1966)].
[6] M. L. Ter-Mikaelyan, *The Effect of the Medium on Electromagnetic Processes at High Energies* [in Russian], Erevan, 1969.
[7] A. P. Potylitsin, ''Transition radiation and diffraction radiation. Similarities and differences,'' to be published in Nucl. Instrum. Methods B (1998).
[8] V. P. Shestopalov, *Diffraction Electronics* [in Russian], Kharkov, 1976.
[9] Y. Shibata, S. Hasebe, K. Ishiki *et al.*, Phys. Rev. E **52**, 6787 (1995).
[10] D. W. Rule, R. B. Fiorito, and W. D. Kimura, ''Noninterceptive beam diagnostics based on diffraction radiation,'' to be published in *Proceedings of the 7th Beam Instrumentation Workshop*, Argonne, Illinois (1996).
[11] M. Castellano, Nucl. Instrum. Methods Phys. Res. A **394**, 275 (1997).
[12] X. K. Maruyama, M. J. Hellstrem, C. B. Reid *et al.*, Nucl. Instrum Methods Phys. Res. B **79**, 788 (1993).
[13] R. B. Fiorito, D. W. Rule *et al.*, Phys. Rev. E **51**, 2759 (1995).

Translated by M. E. Alferieff

Long-lived electronic–deformation excitations in a polyacetylene chain — the photoexcitation spectrum

R. I. Rokitskiĭ, D. Yu. Parashchuk,[a)] and T. A. Kulakov
M. V. Lomonosov Moscow State University, 119899 Moscow, Russia

V. M. Kobryanskiĭ
N. N. Semenov Institute of Chemical Physics, Russian Academy of Sciences, 117977 Moscow, Russia

(Submitted 4 March 1998; resubmitted 20 April 1998)
Pis'ma Zh. Éksp. Teor. Fiz. **67**, No. 10, 765–770 (25 May 1998)

It is observed that the photoexcitation efficiency of neutral long-lived states in a *trans*-polyacetylene chain increases with increasing photon energy of the excitation. The observed effect is given an interpretation according to which the energy of a photon above the optical absorption edge is added to the excitation of the vibrational subsystem, increasing sharply the probability that the chain relaxes into a long-lived deformed neutral state. © *1998 American Institute of Physics.* [S0021-3640(98)01010-X]

PACS numbers: 78.40.Me, 71.20.Rv

Polyacetylene $(CH)_x$ is a polymer with a very simple chemical structure containing a system of conjugate π-electron bonds. It has been actively investigated since the end of the 1970s. After a photon is absorbed, rapid nonradiative relaxation of the photoexcitation occurs in a chain of the *trans* isomer of $(CH)_x$. In the process, one relaxation channel corresponds to the formation of bound electronic–deformation excitations called solitons.[1] It is believed that soliton excitations are responsible for a number of unique optical and electronic properties of *trans*-$(CH)_x$ (Ref. 1). Such excitations are observed in the form of photoinduced absorption (PIA) bands below the fundamental absorption edge, and their characteristic lifetime reaches the millisecond range. In the present letter we report the observation of a sharp increase in the photoexcitation efficiency of long-lived electronic–deformation states in a *trans*-$(CH)_x$ chain with increasing excitation photon energy.

The experiments were performed with a highly ordered form of $(CH)_x$, differing from other known types of $(CH)_x$ by high stability and low defect content. Films of highly ordered $(CH)_x$ with approximately the same concentration of the *cis* and *trans* isomers were prepared by the method described in Ref. 2. $(CH)_x$ particles with a characteristic size of 10 nm were dispersed with a concentration of $\sim 2\%$ in a transparent polyvinylbutyral matrix. $(CH)_x$ films with thickness $d \simeq 5$ μm and optical density $\alpha d \simeq 3$ (α is the absorption coefficient of the film) deposited on a sapphire substrate were investigated at temperatures of 85 and 300 K. The variances of the particle size and conjugate-chain length can be neglected in the present investigation. This is indicated by,

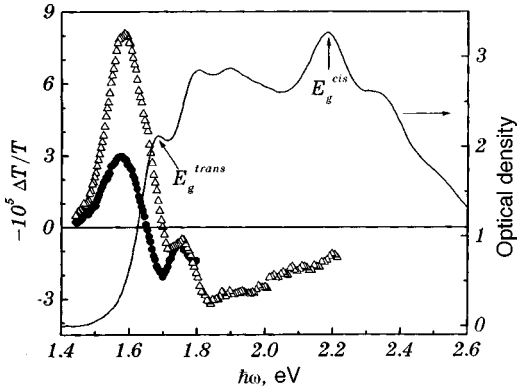

FIG. 1. Linear absorption (solid curve) and PIA spectra for laser excitation with photon energy 2.81 eV (△) and 1.96 eV (●), excitation intensities ≃ 0.2 and 0.6 W/cm^2, respectively, and modulation frequency 140 Hz.

specifically, the sharp optical absorption edge (Fig. 1) and narrow Raman scattering lines of highly ordered $(CH)_x$ (Ref. 3), in light of the well-known dependences of the optical absorption and Raman scattering frequencies on the length of a polymer chain.

The PIA spectra were measured by the ''excitation–probe'' method. Radiation from a xenon lamp equipped with a set of interference filters was used as a wavelength-tunable excitation source. Radiation from cw He–Ne (633 nm) and He–Cd (442 nm) lasers was also used. The excitation-induced changes $\Delta T/T$ in the transmission spectrum of the sample were detected in the probe channel, which included an incandescent lamp, a monochromator, and a silicon photodetector. The photodetector signal was measured with a synchronous detector at the mechanical-modulation frequency of the exciting radiation. The measured signal can be represented in the form $\Delta T/T = N\sigma$, where N is the density of photoexcitations per unit area of the sample, i.e., the volume density integrated over the sample thickness, and σ is the cross section for the absorption of the probe light by photoexcitations. The density of long-lived neutral photoexcitations increases linearly with the optical excitation intensity and is characterized by a linear recombination mechanism.[4] Then, we have in the case of a one-dimensional geometry of the experiment[5]

$$N = (1-R)\epsilon\tau F(1-e^{-\alpha d}), \tag{1}$$

where R is the reflection coefficient of the film, $\tau \lesssim 10$ μs is the recombination time of the photoexcitations, and F is the incident flux of excitation photons. The efficiency of photoexcitation of long-lived states is characterized by ϵ, which includes all possible processes leading to conversion of the initial photoexcitation over times much shorter than τ. We shall assume that τ does not depend on the excitation photon energy; our experiments show that this is so. Only ϵ and α depend on the excitation photon energy, since for our samples with low $(CH)_x$ concentration, R is determined mainly by the matrix.

Figure 1 shows the typical PIA spectra of a $(CH)_x$ film measured for excitation wavelengths of 633 and 442 nm at $T \simeq 300$ K. Three characteristic peaks[4] belonging to *trans*-$(CH)_x$ are observed in the PIA spectrum: a peak due to long-lived neutral excita-

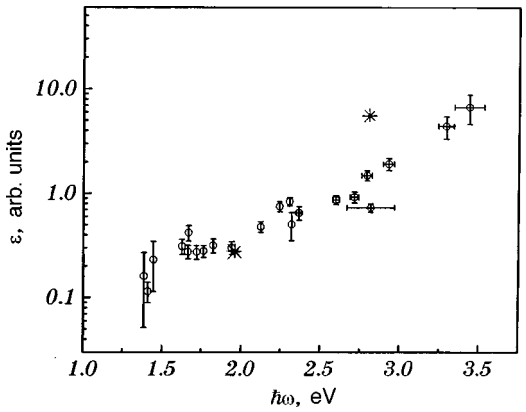

FIG. 2. Photoexcitation spectrum obtained for the 1.6 eV PIA band with a xenon lamp. The two points marked by the asterisk correspond to the data in Fig. 1.

tions (1.6 eV) and two thermally induced peaks due to the temperature modulation of the position of the absorption edge (1.7 and 1.85 eV). The wide ''bleaching'' band above 1.9 eV reflects the transfer of the oscillator strength from the main dipole transition to the peak due to neutral excitations. One can see from Fig. 1 that the ''blue'' radiation (442 nm) gives more efficient photoexcitation of the 1.6 eV band even though it is hardly absorbed at all in the sample and its intensity is three times weaker than the ''red'' radiation (633 nm). We note that only the *trans* isomer of $(CH)_x$ contributes to the signal due to the PIA absorption band at 1.6 eV, since the total isomerization of the sample into the *trans* form changes the PIA spectrum very little. Similar PIA spectra were measured with excitation of a $(CH)_x$ film at $T \simeq 85$ K by radiation from a xenon lamp. The photoexcitation spectrum $\epsilon(\omega)$, calculated according to Eq. (1), for neutral states per pump photon absorbed in the sample is displayed in Fig. 2. Since we were not able to separate correctly the contributions of the *cis* and *trans* isomers to the absorption spectrum of the film above $E_g^{cis} \simeq 2.2$ eV, the photoexcitation spectrum was normalized to the absorption spectrum of the *cis–trans* composition of $(CH)_x$ and not to that of the *trans* isomer. For this reason, the rate of growth of the photoexcitation spectrum should be even higher than follows from Fig. 2. Therefore, a change in the energy of the excitation photon strongly influences the relaxation path of the initial photoexcitation. As the photon energy increases, the probability that $\epsilon(\omega)$ relaxes into a long-lived neutral state increases by at least a factor of 30. No changes in $\epsilon(\omega)$ with temperature were observed (Fig. 2).

In the form of $(CH)_x$ which we investigated, approximately 70 carbon atoms form the polymer chain. For this reason, the $(CH)_x$ chain can be regarded as long polyene molecule on the one hand and a quasi-one-dimensional crystal on the other. We shall discuss our experimental results both on the basis of the concepts of solid-state theory and in terms of the molecular approach.

In terms of band theory, the sharply rising soliton photoexcitation spectrum (Fig. 2), as compared with the corresponding spectra of other known quasiparticles, seems very unexpected. For example, the photoexcitation spectrum of conduction electrons has the form of a step starting at the conduction band edge E_g^{trans}. Optical energy above the band edge $\hbar\omega - E_g^{trans}$ is converted into translational kinetic energy of an electron and a hole.

The photoexcitation spectrum of Wannier–Mott excitons is qualitatively different: It has the form of a sequence of lines with decreasing intensity (excitonic series), starting with the exciton formation energy E_{ex}. It is obvious that under one-photon excitation conditions the excess photon energy $\hbar\omega - E_{ex}$ cannot be transferred into the kinetic energy of an exciton on account of the law of conservation of momentum. An electronic excitation can be self-trapped in a number of materials. In the case of *trans*-$(CH)_x$ it is believed that polaron-type states — topological solitons — are formed as a result of the nonpolar electron–phonon interaction.[1] The self-trapping rate is determined by the characteristic optical-phonon emission times. For example, experiments with a high temporal resolution indicate that in conjugate polymers intraband states are formed no later than 0.1–0.2 ps after photoexcitation.[6–8] In the case of *trans*-$(CH)_x$ it has been established[1,9] that the induced subband absorption peak corresponds to long-lived neutral excitations.

We shall assume that the photoexcitation is self-trapped into solitons. On account of their topological character the solitons should be produced in pairs from the initial photoexcitation.[1,10] The latter should be a state of a bound electron–hole pair (often called a polaron–exciton), since one free carrier can relax only into a polaron. We assume next that the photoexcitation spectrum characterizes not the probability of formation of solitons, but rather the subsequent processes, for example, recombination of solitons. For this it must be assumed that the excess energy ~ 1 eV of a photoexcited electron–hole pair is converted into kinetic energy of the separating quasiparticles, which then influences the probability of their recombination. However, the kinetic energy carried off by a pair of solitons clearly does not exceed $M_s v_s^2 \sim 0.1$ eV, where $v_s \sim 10^6$ cm/s is the speed of sound, $M_s \simeq 6m_e$,[1] and m_e is the electron mass. Therefore the steeply rising photoexcitation spectrum of neutral states reflects, first and foremost, the process of their formation and not the subsequent relaxation.

According to existing ideas, self-trapping in one-dimensional systems is a barrier-free process.[11] For this reason, the observed sharp increase in the probability of photoexcitation of neutral states with excess excitation photon energy $\hbar\omega - E_g^{trans}$ (Fig. 2) is most likely a reflection of the strong dependence of the internal conversion probability (transition from a charged into a neutral state) on $\hbar\omega - E_g^{trans}$. We note that exponential growth of the internal conversion probability as a function of the excess excitation photon energy has been detected in stilbene[12] (see below). The absence of a pronounced temperature dependence of the photoexcitation spectrum implies that the self-trapping and internal conversion processes are determined by nonequilibrium phonons, into which almost all the excess energy $\hbar\omega - E_g^{trans} \sim 1$ eV can be converted. Therefore self-trapping and internal conversion proceed at least more quickly than the phonon subsystem of $(CH)_x$ cools down, which is in agreement with data obtained in experiments with high temporal resolution.[6]

Let us now examine the photoexcitation of a $(CH)_x$ chain in terms of the molecular approach. In the adiabatic approximation and in accordance with the Franck–Condon principle it must be assumed that ''blue'' photoexcitation ($\hbar\omega - E_g^{trans} \sim 1$ eV) populates the high-lying vibrational sublevels of the main dipole transition with quantum number $(\hbar\omega - E_g^{trans})/\hbar\omega_o \sim 10$, where $\hbar\omega_o \sim 0.1$ eV is the optical phonon energy. These vibrational sublevels correspond to vibrations of the chain which are most strongly coupled with π-electrons. The optical excitation of these vibrations is all the more efficient the stronger the electronic–vibrational coupling. Analysis of the absorption spectrum of

trans-$(CH)_x$ on the basis of the Franck–Condon formalism indeed indicates a strong electronic–vibrational coupling, which can be characterized by a Huang–Rice factor of the order of 1 for the lowest vibrational mode. As follows from the photoexcitation spectrum obtained (Fig. 2), the higher the energy (amplitude) of such optically excited vibrations, the higher the probability of the subsequent relaxation of the chain into a deformed neutral state.

For polyatomic molecules it is ordinarily assumed that the energy of a highly excited vibrational mode is rapidly redistributed over a large number of other modes. In the case of molecules prone to change geometry it must be assumed that in the case of intramolecular redistribution of the vibrational energy one or several distinguished (stimulating) modes responsible for the geometric relaxation of the molecule are excited. Apparently, here there is an apt analogy with the *cis–trans* photoisomerization dynamics of stilbene molecules, for which it has been shown experimentally that intramolecular redistribution of vibrational energy and the *cis–trans* conformational transition occur within a few hundred femtoseconds.[12,13] In addition, the probability of a *trans–cis* conformational transition in stilbene[12] increases rapidly with increasing excitation photon energy, just as in our photoexcitation spectrum (Fig. 2). We assume that the excitation of stimulating modes in *trans*-$(CH)_x$ gives rise to a fast internal conversion process corresponding to a parity-violating transition between the dipole excited $1B_u$ state and some neutral state with A_g symmetry. Such an intramolecular transition is forbidden in a centrosymmetric planar $(CH)_x$ chain, but it becomes possible, for example, in the case when noncoplanar vibrations of the chain which remove the forbiddenness with respect to symmetry, specifically, torsional vibrations, are excited.

We shall now note the facts pointing toward a high probability of internal conversion. Our experiments[14] on electroabsorption in $(CH)_x$ and the corresponding model[15] indicate that a state with A_g symmetry lies near the $1B_u$ state within the homogeneously broadened line. Moreover, the states corresponding to these close-lying levels of different symmetry are coupled by a substantial dipole moment of ~ 20 D.[15] The energy of the excitation responsible for the conversion of a charged into a neutral excitation can be estimated as the homogeneous linewidth of the excited electronic states, $\gamma \sim 10$ meV.[7] One can see that torsional vibrational energies of the order of γ are entirely sufficient for fast internal conversion with characteristic time $h/\gamma \simeq 400$ fs, where h is the Planck constant. We note that the intense Raman scattering line with frequency ~ 100 cm^{-1} (12 meV) has been observed[16] in our highly ordered form of $(CH)_x$.

Therefore we arrive at the following conclusion on the basis of both the concepts of solid-state theory and the molecular approach: The photoexcitation spectrum of neutral long-lived states in *trans*-$(CH)_x$ reflects an internal conversion process which can proceed on a subpicosecond time scale. In addition, the probability of this process depends strongly on the excitation level of the phonon subsystem. Paths for further relaxation of a photoexcitation in $(CH)_x$ and polyenes have been discussed in detail in the literature, and their analysis falls outside the scope of the present letter. The final result of this relaxation is in fact observed in the photoinduced absorption spectra in the form of long-lived neutral states, apparently corresponding to a local deformation of the chain. It is likely that dynamic neutral solitons or their bound pairs are responsible for one of the stages of such relaxation.

This work was supported as part of the program ''Fundamental Natural Science'' of

the Ministry of Education of the Russian Federation (Grant 95-0-5.5-176).

[a)]e-mail: paras@polys.ilc.msu.su

---

[1] A. J. Heeger, S. Kivelson, J. R. Schrieffer and W.-P. Su, Rev. Mod. Phys. **60**, 781 (1988).
[2] V. M. Kobryanskii and E. A. Tereshko, Synth. Met. **39**, 367 (1991).
[3] D. Yu. Paraschuk, S. A. Arnautov, A. N. Shchegolikhin, and V. M. Kobryanskii, JETP Lett. **64**, 658 (1996).
[4] D. Yu. Paraschuk, T. A. Kulakov, and V. M. Kobryanskii, Phys. Rev. B **50**, 907 (1994).
[5] J. Orenstein, Z. Vardeny, G. L. Baker *et al.*, Phys. Rev. B **30**, 786 (1984).
[6] C. V. Shank, R. Yen, R. L. Fork *et al.*, Phys. Rev. Lett. **49**, 1660 (1982).
[7] T. Kobayashi, Synth. Met. **50**, 565 (1992).
[8] G. S. Kanner, X. Wei, B. C. Hess *et al.*, Phys. Rev. Lett. **69**, 538 (1992).
[9] J. Orenstein, in *Handbook of Conducting Polymers*, edited by T. A. Skotheim, Marcel Dekker, New York, 1986, Vol. 2, p. 1297.
[10] S. Kivelson and C. Wu, Phys. Rev. B **34**, 5423 (1986).
[11] E. I. Rashba in *Excitons*, edited by E. I. Rashba and M. D. Sturge, North Holland, Amsterdam, 1982 [Russian translation, Nauka, Moscow, 1985].
[12] J. S. Baskin, L. Banares, S. Pederson and A. H. Zewail, J. Phys. Chem. **100**, 11920 (1996).
[13] R. J. Sension, S. T. Repinec, A. Z. Szarka, and R. M. Hochstrasser, J. Chem. Phys. **98**, 6291 (1993).
[14] D. Yu. Paraschuk, T. A. Kulakov, R. I. Rokitskii, and V. M. Kobryanskii, Synth. Met. **84**, 949 (1997).
[15] T. A. Kulakov, Candidate's Dissertation [in Russian], Department of Physics, Moscow State University, Moscow, 1997.
[16] V. M. Kobryanskiĭ, unpublished.

Translated by M. E. Alferieff

Hot-electron-pumped *K*-shell x-ray laser

F. N. Chukhovskii
Institute of Crystallography, Russian Academy of Sciences, 117333 Moscow, Russia

P. Gibbon, I. Uschmann, and E. Förster
Abteilung Röntgenoptik, Institut für Optik und Quantenelektronik, Friedrich-Schiller-Universität Jena, D-07743 Jena, Germany

(Submitted 22 April 1998)
Pis'ma Zh. Éksp. Teor. Fiz. **67**, No. 10, 771–776 (25 May 1998)

Amplified spontaneous inner-shell emission produced via an ultrafast burst of high-energy electrons from a femtosecond laser-produced plasma is proposed as a novel electron-pumped x-ray laser. In this scheme, a population inversion of the upper laser level is created via impact ionization of atomic inner shells by electron bombardment. Based on the requirement of a positive gain coefficient for amplifying spontaneous K_α line emission, a simple pumping threshold is found for the incident electron flux, and feasibility of the scheme is assessed for a range of low-Z elements. © *1998 American Institute of Physics.* [S0021-3640(98)01110-4]

PACS numbers: 42.55.Vc, 42.60.By

It is well-known that bombardment of solids by energetic electrons can produce characteristic x rays via ionization of atoms in the target material.[1] Selective ejection of electrons from inner shells can in principle create a population inversion, providing the conditions for lasing at x-ray wavelengths. However, owing to the high electron flux requirements, short pumping times and superior ionizing selectivity of photons compared to electrons, recent research has concentrated on photo-pumping by soft x-ray pulses from femtosecond laser-produced plasmas (LPPs).[2,3] The attraction of inner-shell x-ray laser schemes is that they offer the possibility of much shorter wavelengths than either traditional collisional and recombination schemes or techniques based on optical field ionization[4] using sub-100 fs lasers.[5]

In this letter we present a simple analysis of an inner-shell ionization x-ray laser pumped by a hot-electron flux from a laser-produced plasma and investigate its feasibility for the K_α line emission of different materials, namely: carbon, fluorine, sodium, and titanium as gain media. We believe that no such kind of assessments for this type of active lasing system has been earlier reported. Related experimental aspects for high-power femtosecond laser systems are discussed.

A prerequisite to achieving lasing in an active medium is to create an inner-shell population inversion of the upper laser level, giving a positive gain–length product. Underneath we follow the time-integrated pumping approach first proposed in Ref. 3, which is reasonable from the physical viewpoint and, for example, does not depend on

any assumptions for constructing appropriate rate equations to describe the evolution of the level populations.

Assuming that the number of vacancies (K-shell holes) per unit volume $N_K^{(\mathrm{vac})}$ is much smaller than the atomic density N_m of the medium: $N_K^{(\mathrm{vac})} \ll N_m$, then the number-vacancy distribution $n_K^{(\mathrm{vac})}$ pumped through a hot-electron K-shell ionization of ground-state atoms as a function of the depth x into the medium is given by (cf. Ref. 3)

$$n_K^{(\mathrm{vac})}/dx = \sigma_K^{(\mathrm{ion})}(U) N_m \tau S \Phi(U), \tag{1}$$

where $\tau\Phi(U)$ is the time-integrated pump electron flux per cm^2 bombarding a solid sample at depth x from a laser-plasma source, τ is the laser pulse duration, and S is the illuminated area [cm^2] of the medium. We assume that the duration of the electron burst $\tau_e \simeq \tau$ and further, that the K-shell lifetime τ_K is typically shorter than τ. $U(x, U_0)$ is the electron-impact energy at depth $x > 0$, and we define $U_0 \equiv U(x=0)$ as the initial energy of an impact electron at the depth $x=0$. The electron-impact K-shell ionization cross section $\sigma_K^{(\mathrm{ion})}[U(x, U_0)]$ is given for a large range of elements in Ref. 6. The energy $U(x, U_0)$ at depth x can be found from the Bethe formula valid over the range $U_0 \simeq 10$–100 keV.[7] Note that Eq. (1) takes into account the population inversion of the *upper* laser level in relation to the number of K-shell vacancies n_K only. The eventual saturation of this value due to other processes detrimental to the lasing effect — in particular to L-shell vacancy production — will be discussed in detail later. For simplicity, we neglect these additional destructive effects in order to obtain the gain threshold.

In Eq. (1) a monoenergetic electron beam has been assumed. In fact, electrons from a LPP generally have an energy distribution $f(U_0)$. It is then necessary to modify Eq. (1) by substituting

$$\sigma_K^{(\mathrm{ion})}(U)\Phi(U) \to \overline{\sigma_K^{(\mathrm{ion})}(x)\Phi(x)} \equiv \int (dU_0 f(U_0) \times \sigma_K^{(\mathrm{ion})}(U)\Phi(U)).$$

For a monodirectional Maxwellian the function $f_H(U_0)$ has the normalized form $f_H(U_0) = U_0 T_H^{-2} \exp(-U_0/T_H)$, where T_H is the characteristic hot-electron temperature.

Let us designate the average gain coefficient of amplified spontaneous emission (ASE) as

$$\overline{G}_K \equiv X_H^{-1} \int_0^{X_H} G_K(x)\, dx,$$

where X_H is the hot-electron penetration depth, equal to the effective thickness of the gain medium. Then

$$\overline{G}_K = \sigma_K^{(\mathrm{stim})} \frac{N_m \tau_K}{X_H} \int_0^{X_H} dx\, \overline{\sigma_K^{(\mathrm{ion})}(x)\Phi(x)} - \mu_K, \tag{2}$$

where μ_K is the absorption coefficient of the K_α line radiation obtained (see Ref. 8). X_H can be estimated from the Bethe formula

$$X_H = \frac{4\pi}{e^4 N_m Z_m} [0.5(1 - \ln 2) + \ln(T_H/J)]^{-1}, \tag{3}$$

where Z_m is the atomic number of the medium, and $J=13.6Z_m$ eV is the average ionization potential. Setting $\overline{G_K}=0$ in Eq. (2), we obtain an estimate for the time-integrated pump electron flux threshold over the effective lifetime τ_K

$$\Phi_H^{(\mathrm{thres})}\tau_K \approx \mu_K/(\sigma_K^{(\mathrm{stim})}N_m\sigma_K^{(\mathrm{ion})}(T_H)), \tag{4}$$

required to produce single-pass self-terminating ASE over the length of a gain medium equal to the lateral size of the hot-electron pump beam.

In the case under consideration here, the x-ray K_α linewidth mainly depends on a broadening of τ_K, in which case the cross section for stimulated emission $\sigma_K^{(\mathrm{stim})}$ is given by[9]

$$\sigma_K^{(\mathrm{stim})}=\lambda_K^2\tau_K/4\tau_K^{(\mathrm{rad})}, \tag{5}$$

where $1/\tau_K^{(\mathrm{rad})}$ is the probability of spontaneous K_α line emission. Note that the K_α transitions of the materials considered here have typical effective lifetimes τ_K of the order of few femtoseconds, which are much shorter than a laser pulse duration τ. Thus the effective pumping flux is reduced by a factor $\tau_K/\tau<1$.

In order to evaluate Eq. (4), we need values of the electron impact ionization cross section for the production of K-shell vacancies in a variety of candidate media for lasing. Direct calculations taking into account corrections for weakly relativistic energies for the K-shell cross sections $\sigma_K^{(\mathrm{ion})}$ of carbon, fluorine, sodium, and titanium definitely show that of the four media investigated, carbon has the largest cross section $\sigma_K^{(\mathrm{ion})}=10^{-19}$ cm^2 in the electron impact-energy range, extending well above the minimum energy threshold required for ejection of a K-shell electron to the continuum. Using the numerical values obtained for $\sigma_K^{(\mathrm{ion})}$ together with Eqs. (2)–(5), we find that the resulting hot-electron flux threshold $\Phi_H^{(\mathrm{thres})}\tau_K$ [10^{16} cm^{-2}] for the K_α lines of carbon, fluorine, sodium, and titanium are equal to 0.163, 0.401, 1.099, and 21.035, respectively.

On the other hand, the corresponding values of $\sigma_L^{(\mathrm{ion})}$ are at least one order of magnitude larger than $\sigma_K^{(\mathrm{ion})}$, which at first sight appears to support the original conclusion made in Ref. 2 that electrons are not as well suited as photons for selectively removing electrons from inner shells. However, it will be shown later that L-shell ionization sets an effective upper limit on the flux which for low Z is sufficiently far above the K-shell threshold to allow a flux window in which positive gain is possible. We therefore initially consider the elements above as candidates for selective K-shell x-ray stimulated emission.

Before we can determine the x-ray gain which can be obtained with this type of scheme, we need to know the hot electron flux available from contemporary femtosecond-laser-produced plasmas. Although a number of experimental studies of hot-electron generation with short pulse lasers now exist, there are considerable variations in the absorption levels and hot-electron temperatures found (see Ref. 10 for a recent review). To determine the hot-electron temperature T_H and number flux $\Phi[T_H]$, we have performed particle-in-cell (PIC) simulations for a range of intensities relevant to the electron-pumped x-ray laser scheme. By performing a series of these simulations for different laser intensities, we obtain the scaling law for the hot-electron temperatures T_H:

$$T_H=7.5(I_{16}\lambda_{\mu m}^2)^{1/3}, \tag{6}$$

where I_{16} is the intensity in 10^{16} W/cm^2 and $\lambda_{\mu m}$ is the wavelength is microns. The hot-electron energy flux can be obtained from the energy balance equation

$$Q_H = \int dU_0 U_0 f_H(U_0) = \eta_H I \tau \cos\theta,$$

where η_H is the fraction of laser energy absorbed by the hot electrons and θ is the angle of incidence to the target normal. Assuming we can approximate the energy spectrum of hot electrons by a Maxwellian, we may write $Q_H = 2T_H \Phi_H \tau$, so that:

$$\Phi_H \tau = \eta_H I \tau \cos\theta / 2T_H . \tag{7}$$

Both η_H and T_H are to be determined by simulation. In general, if $f_H(U_0)$ is highly non-Maxwellian, then Φ_H must also be determined numerically.

For the purposes of this study however, it suffices to use the temperature from the simulations given by Eq. (6), which on substituting into Eq. (7), gives the following expression for the time-integrated hot-electron flux:

$$\Phi_H \tau [10^{16}\ \text{cm}^{-2}] \simeq 0.9 \eta_H I_{16}^{2/3} \lambda_{\mu m}^{-2/3} \tau_{fs} \cos\theta, \tag{8}$$

where τ_{fs} is the pulse length in femtoseconds. For example, the hot-electron number flux expected for a 10 fs Ti–Sa laser at an intensity of 10^{16} W/cm^2 is 1.1×10^{16} cm^{-2} with a temperature of 6 keV, whereas at 10^{18} W/cm^2 we would have $\Phi_H = 2.4\times10^{17}$ cm^{-2} with $T_H = 30$ keV. This assumes an average laser absorption of $\eta_H = 0.15$, which was roughly constant ($\pm 2\%$) over the range of parameters considered here, and no attempt was made to maximize it according to the plasma conditions (in fact, one would expect 50–60% absorption at grazing incidence angles).[11] Note that Eq. (8) is not universal and does not take into account differences in target material, bulk plasma temperature, or lateral spreading of the electrons due to scattering.

For typical laser parameters considered here ($I \sim 10^{16} - 10^{17}$ W/cm^2, $\tau \sim 10$ fs), one finds that the ratio of the number of K-shell vacancies per unit volume to the atomic density has values $N_K^{(\text{vac})}/N_m \sim 10^{-3} - 10^{-2}$ for elements with $Z < 10$. However, for the L shell the ratio is of the order of unity, implying that the L-shell vacancy population equation really should be taken into account when calculating the phenomenological damping factor. Increasing the either flux or Z will increase the ratios $N_K^{(\text{vac})}/N_m$, $N_L^{(\text{vac})}/N_m$, etc., reducing and eventually reversing the gain.

A quantitative assessment of the threshold beyond which L-vacancy generation becomes dominant can be made within the scope of the present model by introducing a correction factor into Eq. (1). We assume that this correction has two principal contributions: on the one hand, the L-shell vacancies 'poison' the ground state of neutral atoms N_m, and on the other hand, they enhance the pumping hot-electron flux by adding a slightly ''colder'' secondary electron flux. The pumping flux and density of neutral atoms are therefore modified as follows:

$$\Phi^{\text{cor}} \tau_K = \Phi \tau_K (1 + \tau_K (2U/m_e)^{1/2} \sigma_L N_m), \tag{9}$$

$$N_m^{\text{cor}} = N_m (1 - \sigma_L \Phi^{\text{cor}} \tau_K). \tag{10}$$

Combining Eq. (1) with Eqs. (9) and (10) for $v_H = (2U/m_e)^{1/2}$, we can write the correction factor to the K-vacancy production rate as

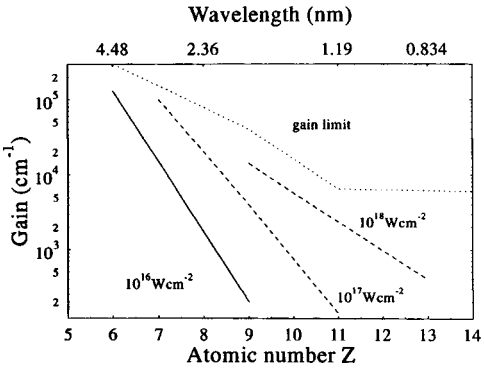

FIG. 1. Scaling of gain coefficients with Z for electron pumping at different laser intensities and wavelength of 0.8 μm. The top x axis shows the corresponding K_α wavelength. The ''gain limit'' curve is obtained by setting $d\bar{G}_K/d\Phi=0$ according to Eq. (12).

$$A\equiv\frac{N_m^{\rm cor}\Phi^{\rm cor}}{N_m\Phi}=[1-\sigma_L\Phi\tau_K(1+\tau_K(2U/m_e)^{1/2}\sigma_L N_m)^2+\tau_K(2U/m_e)^{1/2}\sigma_L N_m]. \quad (11)$$

The second term on the right-hand side of Eq. (11) diminishes the population of the upper laser level due to L-vacancy generation, so reducing the gain. In contrast, the third term actually enhances the number of K-shell vacancies owing to the flux of secondary electrons produced by the L-shell ionization. This leads to an enhancement of the inversion and gain. To give a numerical example, the correction factor for a carbon target with $N_m=10^{23}$ cm^{-3}, $\sigma_L=2\times10^{-18}$ cm^2, $\tau_K=10^{-14}$ s, $v_H=3\times10^9$ cm/s ($2U\sim T_H=10$ keV) and $\Phi=3\times10^{15}$ cm^{-2} is $A\simeq1-0.2+6=6.8$, whereas for a $\Phi=3\times10^{17}$ cm^{-2}, we have $A\simeq1-22+6=-15$. In other words, for a given element there should be an operating ''window'' of flux in which we can expect amplification of the K_α line, the upper limit of which is determined by setting Eq. (10) to zero.

Combining Eqs. (2) and (11), averaging over the cross-section integral $\bar{\sigma}_K\simeq X_H^{-1}\int_0^{X_H}dx\sigma_K$, with $\Phi=\bar{\Phi}=$const, we finally arrive at an expression for the gain including the effect of secondary electrons:

$$\bar{G}_K=\sigma_K^{(\rm stim)}N_m\tau_K\bar{\Phi}\bar{\sigma}_K[1-\sigma_L\Phi\tau_K(1+\tau_K(2U/m_e)^{1/2}\sigma_L N_m)^2 + \tau_K(2U/m_e)^{1/2}\sigma_L N_m]-\mu_K. \quad (12)$$

This expression is evaluated for different Z using values for τ_K and μ_K from Ref. 12.

We are now in a position to estimate the gain coefficient according to Eq. (12) by substituting Eq. (8) for the electron flux. This is done in Fig. 1, which shows best-fit curves for different elements and laser intensities, assuming a constant pulse length of 10 fs.

The gain–length product will of course depend on the lateral extent of the hot electrons, or the laser focal spot size. For example, a 1 J, 10 fs Ti–Sa laser focused to a

spot size of 100 μm and intensity 3×10^{17} W/cm^2 would yield $G_KL\simeq130$ for fluorine. The maximum gain can be found by setting $d\overline{G}_K/d\Phi=0$ and is shown as the upper dashed curve in Fig. 1.

One could argue that the L-shell and secondary processes will always dominate because the absolute value of the ''correction'' factor in Eq. (11) is substantially larger than unity. Nevertheless, we neglect all additional processes (production of tertiary electrons, effects of plasma radiation etc) on the grounds that these will mainly occur *after* the lasing lifetime τ_K.

The presence of satellite lines arising from transitions in multiply-ionized inner shells on the high-energy side of the K- and L-shell emission (see, e.g., Ref. 13) could also reduce the gain coefficients depicted in Fig. 1. On the other hand, by including the fluorescence yields and impact cross sections for the production of satellites, the model presented here could be extended to *multimode* soft x-ray schemes for pumping ASE by LPP hot electrons.

In conclusion, we have developed a semi-analytical model to assess the hot-electron pumping requirements for a transverse ASE positive gain on the K-shell transitions of light elements. The scheme appears to be best suited to laser pulse lengths around 10 fs and elements with $Z\leqslant15$, and offers a potential means of extending the operational regime of x-ray lasers down to subnanometer wavelengths.

This work was supported in part by European TMR Contract ERB 4061PL95-1313.

[1] M. Green and E. Cosslett, Brit. J. Appl. Phys. (J. Phys. D) **1**, Ser. 2 (1968).
[2] M. A. Duguay and P. M. Rentzepis, Appl. Phys. Lett. **10**, 350 (1967).
[3] W. T. Silfvast and O. R. Wood II, J. Opt. Soc. Am. B **4**, 609 (1987).
[4] P. Amendt, D. C. Eder, and S. C. Wilks, Phys. Rev. Lett. **66**, 2589 (1991).
[5] C. P. J. Barty *et al.*, Inst. Phys. Conf. Ser. **151**, 282 (1996) (Proc. 5th Intern. Conf. on X-Ray Lasers, Lund, Sweden, June 10–14, 1996).
[6] W. Lotz, Z. Phys. **232**, 101 (1970).
[7] H. Bethge and J. Heydenreich, *Elektronenmikroskopie in der Festkörperphysik*, Springer, 1982.
[8] B. L. Henke, E. M. Gullikson, and J. C. Davis, At. Data Nucl. Data Tables **54**, 181 (1993).
[9] R. C. Elton, *X-ray lasers* (Academic Press, 1990).
[10] P. Gibbon and E. Förster, Plasma Phys. Controlled Fusion **38**, 769 (1996).
[11] A. A. Andreev *et al.*, Zh. Éksp. Teor. Fiz. **101**, 1808 (1992) [Sov. Phys. JETP **74**, 963 (1992)].
[12] G. Zschornack, *Atomdaten für die Röntgenspektralanalyse*, Deutscher Verlag für Grundstoffindustrie, Leipzig, 1989.
[13] J.-C. Gauthier *et al.*, Phys. Rev. E **51**, 2963 (1995).

Published in English in the original Russian journal. Edited by Steve Torstveit.

Spin waves in classical gases

T. L. Andreeva and P. L. Rubin
P. N. Lebedev Physical Institute, Russian Academy of Sciences, 117924 Moscow, Russia

(Submitted 13 April 1998)
Pis'ma Zh. Éksp. Teor. Fiz. **67**, No. 10, 777–782 (25 May 1998)

A criterion for the propagation of weakly-damped spin waves is obtained on the basis of a detailed analysis of the quantum collision integral for particles in a paramagnetic polarized Boltzmann gas. It is shown that according to this criterion spin waves can propagate in classical (nonquantum) gases at temperatures close to room temperature. © *1998 American Institute of Physics.*
[S0021-3640(98)01210-9]

PACS numbers: 51.60.+a, 34.90.+q

In the absence of external electric and magnetic fields, the only propagating collective mode in gases that have Boltzmann statistics is a sound wave. Silin has pointed out the possibility of collective spin oscillations in a paramagnetic gas,[1] Aronov has examined spin-wave oscillations of an electron gas in semiconductors,[2] and Bashkin has predicted the existence of weakly damped spin waves in spin-polarized Boltzmann gases.[3] In Ref. 3 the criterion for the existence of a new collective mode in a spin-polarized gas is reduced to the requirement that the gas be a ''quantum'' gas: The average de Broglie wavelength must be much greater than the size of an atom (scattering amplitude). Despite the large number of works devoted to the dynamics and kinetics of spin-polarized gases (see, for example, Ref. 4 and the references cited therein), this criterion has never been questioned, even though it was based on purely qualitative considerations.[5] It imposes a quite strict constraint on the gas temperature, since most gases condense long before the indicated criterion is first satisfied. For this reason the only appropriate objects were considered to spin-polarized hydrogen $H\uparrow$ and $^3He\uparrow$. The existence of spin waves in these two gases has been confirmed experimentally.[6,7] We underscore that in this case the spin is nuclear spin.

In the present letter a criterion for the propagation of spin waves in a polarized Boltzmann gas is obtained on the basis of a detailed investigation of the collision integral. It is shown that the main quantity governing the propagation of spin waves in Boltzmann paramagnetic gases is the real part of the zero-angle exchange-scattering amplitude. It happens that in ordinary gases, where the scattering of atoms is of a quasiclassical character and sharply anisotropic, the situation is more favorable than in ''quantum'' gases, where scattering is essentially isotropic (*s* scattering).[8] The criterion obtained is different from that adopted in the literature.[3–6] It greatly expands the group of paramagnetic gases where weakly damped spin waves can propagate at temperatures close to room temperature. An example are alkali-metal vapors (Na, Cs, Rb), where a high degree of polarization of the electron spin can be obtained.[9]

Let us consider a paramagnetic gas with externally induced spin polarization (whose vector **M** is directed along the z axis). In this case the Wigner matrix has the form

$$f_{\alpha\alpha'}(p)=f^{(0)}(p)[(\delta_{\alpha\alpha'}+M\sigma_{\alpha\alpha'})+\phi_{\alpha\alpha'}(p)].$$

Here $f^{(0)}(p)$ is the equilibrium Maxwell momentum distribution function (as is the convention in the kinetic theory of gases, the function is normalized to the particle density $n=\int dp f^{(0)}(p)$), $\sigma_{\alpha\alpha'}$ is a vector of Pauli matrices, and $\phi_{\alpha\alpha'}(p)$ is a small perturbation of the Wigner function. It is convenient to decompose the function $\phi_{\alpha\alpha'}(p)$ into scalar (φ) and vector (μ) components:

$$\phi_{\alpha\alpha'}(p)=\varphi(p)\delta_{\alpha\alpha'}+\mu(p)\sigma_{\alpha\alpha'}. \tag{1}$$

The present work is concern with the dynamics of the transverse (with respect to the z axis) component of the magnetic polarization of a gas. It is convenient to combine the quantities μ_x and μ_y as follows: $\mu_\pm=\mu_x\pm i\mu_y$. The kinetic equation for the space–time Fourier components of $\mu_\pm$ has the form

$$[-i\omega\mu_\pm(\omega,k,p)+ikv\mu_\pm(\omega,k,p)]=J_\pm(\mu_\pm). \tag{2}$$

Here ω is the frequency, k is the wave vector, and $J_\pm$ is the collision integral.

The explicit form of the collision integral can be obtained with the aid of Refs. 10 and 11. In view of its complexity, we present an abbreviated form and describe in detail only the term L_I that plays the main role in what follows:

$$J_\pm=Q_R\pm i|M|Q_I\mp i|M|L_I. \tag{3}$$

Here Q_R and Q_I are integral operators which are quadratic in the T matrix (scattering amplitude) and whose structure has the same character as in the conventional Boltzmann equation. The eigenvalues of the operators Q_R and Q_I are of the same order of magnitude as $\nu_s\simeq n\bar{v}\sigma$, where σ is the gas kinetic collision cross section and $\bar{v}$ is the average thermal velocity of the atoms.

The structure of the operator L_I is substantially different:

$$L_I(\mu_\pm)=16\pi^3\hbar^2\int dp_1 f^{(0)}(p_1)$$
$$\times\mathrm{Re}\left\{T_{\mathrm{ex}}\left(\frac{p-p_1}{2},\frac{p-p_1}{2}\right)[\mu_\pm(p)-\mu_\pm(p_1)]\right\}. \tag{4}$$

Here T_{ex} is the T matrix of spin-exchange scattering $(\uparrow\downarrow\rightarrow\downarrow\uparrow)$:

$$T_{\mathrm{ex}}(P,P')=2\theta(P,P')+\theta(-P,P')-t(-P,P'),$$

P and P' are the relative momenta of the colliding particles, scaled to the reduced mass of the atoms $(m/2)$, while t and θ are related with the total scattering matrix (for identical fermions) as follows:

$$T_{\alpha\beta\mu\nu}(P,P')=\hat{A}[t(P,P')\delta_{\alpha\mu}\delta_{\beta\nu}+\theta(P,P')\sigma_{\alpha\mu}\sigma_{\beta\nu}]$$
$$=t(P,P')\delta_{\alpha\mu}\delta_{\beta\nu}-t(-P,P')\delta_{\alpha\nu}\delta_{\beta\mu}+\theta(P,P')\sigma_{\alpha\mu}\sigma_{\beta\nu}-\theta$$
$$\times(-P,P')\sigma_{\alpha\nu}\sigma_{\beta\mu}. \tag{5}$$

Here $\hat{A}$ denotes antisymmetrization with respect to an interchange of the particles (incident and scattered). The product of Pauli matrices is a scalar product: $\Sigma_j \sigma_{\alpha\mu}^{(j)} \sigma_{\beta\nu}^{(j)}$. It is easy to show that formula (5) describes collisions which conserve the total spin. This is a good approximation not only in the case of nuclear spin (H, ^{3}He) but also for atoms with electronic spin (alkali-metal vapors).[9]

All three operators Q_R, Q_I, and L_I are Hermitian in the space L of the functions $\mu(p)$ with the scalar product conventionally used in the kinetic theory of gases,[12] so that the operators J_+ and J_- are Hermitian conjugates of each other. The function $|1\rangle = \mu_\pm \equiv 1$ is an eigenfunction of the operators $J_\pm$ with zero eigenvalue, which is a consequence of the conservation of the total spin in collisions (see Eq. (5)). Moreover, the zero eigenvalue of $J_\pm$ is nondegenerate, since there are no other conservation laws in the ''$\mu_\pm$ subspace.'' The conservation laws for momentum, energy, and particle number refer to the diagonal elements of the Wigner matrix.

Mathematically, Eq. (2) is an eigenvalue problem for the operators $J_\pm - ik\hat{v}$ ($\hat{v}$ denotes multiplication by the velocity treated as an operator). For small k ($|kv| \ll \nu$, where ν is the absolute magnitude of the characteristic eigenvalue of the operator $J_\pm$), this problem can be solved by perturbation theory with respect to the operator $ik\hat{v}$, i.e., in the hydrodynamic approximation.[12] The first-order perturbation theory correction equals zero because of the isotropy of the equilibrium velocity distribution function.

In the present case the second-order correction can be written as[12]

$$-i\omega_\pm = k^2 \langle 1|\hat{v} J_\pm^{-1} \hat{v}|1\rangle. \tag{6}$$

Here $J_\pm^{-1}$ is the inverse of the operator $J_\pm$ on the subspace $(1-\hat{P})L$ ($\hat{P} = |1\rangle\langle 1|$): The operator $J_\pm$ is noninvertible in the initial space L, since it has a zero eigenvalue.

Let us consider first an unpolarized gas ($M=0$). In this case $J_+ = J_- = Q_R$. The eigenvalues of Q_R (and Q_R^{-1}) are real, and therefore ω is purely imaginary. Therefore in this case we have simply spin diffusion. As usual,[12] in this situation it is possible only to estimate the corresponding diffusion coefficient:

$$D_s = \langle 1|\hat{v} J_R^{-1} \hat{v}|1\rangle. \tag{7}$$

In order of magnitude $D_s \sim \overline{v^2}/3\nu_s$, where $1/\nu_s$ is the characteristic eigenvalue of the operator Q_R^{-1}. The spin diffusion coefficient D_s in the general case is different from other transport coefficients, since the corresponding effective collision frequencies are different.

The situation is substantially different in a polarized gas. Let $|M| \sim 1$ (the requirement that the density matrix be positive-definite gives the condition $0 \leqslant |M| \leqslant 1$, and for optical polarization of a paramagnetic gas a value of $|M|$close to 1 can be achived in a straightforward way). Now, the operators $J_\pm$ essentially reduce to the third term on the right-hand side of Eq. (5), while the first two operators can be treated as a small correction.

To show this we shall estimate the real part $\mathrm{Re}[T_{ex}(0)]$ of the zero-angle exchange-scattering amplitude. It follows from the general formula for the T matrix[13] that the Born term makes the main contribution to the zero-angle scattering matrix for fast atoms, since the oscillations of the factor $\exp(ikx)$, which describes the incident wave ($k = p/\hbar$ is the

wave vector of the atom), are completely cancelled out in it. At room temperature (and actually at lower temperatures also) the relation $|k|a_0 \gg 1$, where a_0 is the effective interaction radius, holds by a large margin for electron spin exchange. This last inequality means that the atoms are fast. Thus the operator L_I, or, more accurately, its characteristic eigenvalue ν_{ex}, is proportional to the Born amplitude for scattering by zero angle:

$$A(0) = -\frac{m}{4\pi\hbar^2}\int U d^3x \simeq -\frac{m}{4\pi\hbar^2}|U|a_0^3$$

(U is the exchange interaction potential).

The ratio ν_{ex}/ν_s can now be easily estimated. It equals in order of magnitude

$$\frac{\nu_{ex}}{\nu_s} \sim |M|\frac{|U|a_0}{\hbar\overline{v}}. \tag{8}$$

We note that the right-hand side of this relation is, to within the factor $|M|$, the so-called ''Born parameter,''[8] which is usually large in classical (nonquantum) gases. A numerical estimate of the Born parameter for cesium atoms will be presented below as an example.

So, to a first approximation in the (inverse) Born parameter Eq. (2) can be represented in the form

$$(kv-\omega)\mu_\pm(p) = \mp 16|M|\pi^3\hbar^2\int dp_1 f^{(0)}(p_1)\mathrm{Re}\ T_{ex}(0)[\mu_\pm(p)-\mu_\pm(p_1)]. \tag{9}$$

This equation can once again be studied in perturbation theory, just as we did earlier. Here, however, a different method will be used for estimates. To simplify the problem let $T_{ex} =$ const, i.e., T_{ex} is independent of energy. Then

$$(kv-\omega)\mu_\pm(p) = \mp\nu_{ex}\left[\mu_\pm(p) - \frac{1}{n}\int dp_1 f^{(0)}(p_1)\mu_\pm(p_1)\right]$$

(but now $\nu_{ex} = 16|M|\pi^3\hbar^2 n\mathrm{Re}T_{ex}$).

The following dispersion relation is obtained in the hydrodynamic approximation ($|k\overline{v}/\nu_{ex}| \ll 1$, $|\omega/\nu_{ex}| \ll 1$):

$$\omega = \pm\frac{k^2\overline{v^2}}{3\nu_{ex}}. \tag{10}$$

This equation describes an undamped spin-polarization wave. The diffusion damping Γ of the wave is an effect of the next order in the inverse Born parameter ν_s/ν_{ex}. The quantity Γ can be estimated as

$$\Gamma \sim \frac{k^2\overline{v^2}}{\nu_{ex}}\frac{\nu_s}{\nu_{ex}} \ll \omega. \tag{11}$$

Therefore weakly damped spin waves, whose frequency and damping are estimated by Eqs. (10) and (11), can propagate in a paramagnetic polarized Boltzmann gas. We note that the diffusion damping Γ (11) of spin waves in a polarized gas is $(\nu_s/\nu_{ex})^2$ times smaller than the corresponding quantity in an unpolarized gas (7).

As an example, let us consider the parameters of spin waves in vapor of polarized cesium, for which the required experimental data are available. According to Ref. 14, electronic spin polarization in cesium vapors is conserved to a high degree of accuracy: The ratio of the cross sections for collisions with spin nonconservation and spin exchange is of the order of 1%. The quantity $a_0 \sim 10^{-7}$ cm.[14,15] We take as an estimate of $|U|$ a values of twice the binding energy of the Cs_2 molecule: $|U| \sim 1$ eV.[16] Then the Born parameter at an average thermal velocity of cesium atoms $\bar{v} = 2 \times 10^4$ cm/s is of the order of 10^3. This large value of the Born parameter is intimately connected with the pronounced anisotropy of the scattering indicatrix of fast particles.[8] We note that the temperature dependence of this parameter derives mainly from the dependence $\bar{v} \sim \sqrt{T}$. Therefore the Born parameter approaches 1 only at temperatures less than 10^{-4}–10^{-3} K.

According to Eqs. (10) and (11), the frequency-to-damping ratio of a spin wave is

$$\frac{\omega}{\Gamma} \sim 10^3 |M|.$$

It follows hence that narrowing increases with $|M|$. It should be kept in mind that, generally speaking, this estimate may need to be refined by taking into account the actual weak spin nonconservation.

In summary, the condition for spin-wave propagation in a polarized Boltzmann gas is determined by two factors: spin conservation, i.e., the slowness of spin destruction in collisions, and a sharp anisotropy of the scattering phase function for atoms at room temperature. As is well known, in this case the scattering occurs mainly by small angles near $(|k|a_0)^{-1}$ $(|k| = m\bar{v}/\hbar)$. For cesium at room temperature the corresponding range of angles is $\simeq 10^{-3}$.

To observe spin waves in alkali-metal vapors, besides the conventional magnetic-resonance method,[17] it is of interest to employ the method of scattering of light near the resonance D lines of the atoms. As was shown in Ref. 18, the polarizability of an atom near resonance lines has a large antisymmetric component, which makes it possible to observe the kinetics of spin fluctuations. In the presence of spin waves the spectrum of electron spin polarization fluctuations should consist of a well-resolved doublet with narrow components.

This work was supported by the Russian Fund for Fundamental Research under Grant 96-02-17312-a.

[1] V. P. Silin, Zh. Éksp. Teor. Fiz. **33**, 1227 (1957) [Sov. Phys. JETP **6**, 945 (1958).
[2] A. G. Aronov, Zh. Eksp. Teor. Fiz. **73**, 577 (1977) [Sov. Phys. JETP **46**, 301 (1977)].
[3] E. P. Bashkin, JETP Lett. **33**, 8 (1981).
[4] A. E. Meyerovich, S. Stepaniants, and F. Laloë, Phys. Rev. B **52**, 6808 (1995).
[5] E. P. Bashkin, Usp. Fiz. Nauk **148**, 433 (1986) [Sov. Phys. Usp. **29**, 238 (1986)].
[6] B. R. Johnson, J. S. Den'ker, N. Bigelow *et al.*, Phys. Rev. Lett. **52**, 1508 (1983); **53**, 302 (1984).
[7] N. Bigelow, P. J. Nacher, and M. Leduc, J. Phys. II France **2**, 2159 (1992).
[8] L. D. Landau and E. M. Lifshitz, *Quantum Mechanics: Non-Relativistic Theory*, 3rd ed., Pergamon Press, New York, 1977 [cited Russian original, 4th ed., Nauka, Moscow, 1989].
[9] R. J. Knize, Phys. Rev. A **40**, 6219 (1989).
[10] R. F. Snider, J. Chem. Phys. **32**, 1051 (1960).
[11] T. L. Andreeva and P. L. Rubin, Zh. Éksp. Teor. Fiz. **111**, 831 (1997) [JETP **84**, 457 (1997)].
[12] R. Balescu, *Equilibrium and Nonequilibrium Statistical Mechanics*, Wiley, New York, 1975 [Russian trans-

lation, Mir, Moscow, 1978]; P. Résibois and M. De Leener, *Classical Kinetic Theory of Fluids*, Wiley, New York (1997) [Russian translation, Mir, Moscow, 1980].
[13] M. Goldberger and K. Watson, *Collision Theory*, Wiley, New York, 1964 [Russian translation, Mir, Moscow, 1967].
[14] N. D. Bhaskar, J. Pietras, J. Camparo *et al.*, Phys. Rev. Lett. **44**, 930 (1980).
[15] A. A. Radtsig and B. M. Smirnov, *Reference Data on Atoms, Molecules, and Ions*, Springer-Verlag, New York, 1985 [Russian original, Atomizdat, Moscow, 1980].
[16] W. Happer, Rev. Mod. Phys. **44**, 169 (1972).
[17] L.-J. Wey, N. Kalenchofsky, and D. Candela, Phys. Rev. Lett. **71**, 879 (1993).
[18] T. L. Andreeva, P. L. Rubin, and E. A. Yukov, Zh. Éksp. Teor. Fiz. **107**, 1160 (1995) [JETP **80**, 645 (1995)].

Translated by M. E. Alferieff

Efficient photoluminescence from triangular quantum wells at the interface of an InP/$In_{0.53}Ga_{0.47}As$ heterostructure

É. L. Nolle[a)] and A. M. Prokhorov
Institute of General Physics, Russian Academy of Sciences, 117942 Moscow, Russia

(Submitted 6 March 1998)
Pis'ma Zh. Éksp. Teor. Fiz. **67**, No. 10, 783–787 (25 May 1998)

Efficient photoluminescence (PL) with quantum yield close to 1 from InP/$In_{0.53}Ga_{0.47}As$ heterostructures (HSs) at temperatures 77–300 K and low excitation levels is observed and investigated. The PL is due to a quasi-triangular quantum well (TQW) located at the HS interface and consists of two spectrally similar lines: InGaAs interband emission and emission from the bottom level of the TQW. It is found that as the temperature increases, the intersubband emission rises, while the TQW radiation is quenched. © *1998 American Institute of Physics.* [S0021-3640(98)01310-3]

PACS numbers: 78.66.Fd, 68.65.+g, 81.15.Kk

Lightly doped semiconductors at low excitation levels $g \leqslant 1$ W/cm^2 and $T \approx 300$ K have a low quantum yield of radiation $Q \ll 1$ (ratio of the number of photons emitted inside the semiconductor to the number of electron–hole pairs excited in the emission region), while for high $g \geqslant (10^3 - 10^4)$ W/cm^2 the nonradiative recombination processes are suppressed, making it possible to obtain $Q \approx 1$.[1] By exploiting quantum size effects to restrict the spreading of nonequilibrium electrons and holes, it is now possible to obtain radiative transitions at lower excitation levels. Even so, however, the intensity of the photoluminescence (PL) of quantum dots, for example, is approximately 20 times lower at $T = 300$ K than at 77 K.[2]

This letter reports the generation of efficient PL in a lightly doped semiconductor with quantum yield of radiation $Q = 0.8$ at $T = 295$ K and a low excitation level ($g = 0.05$ W/cm^2). Such intense PL is explained by the formation of a quasi-triangular quantum well (TQW) at the interface of an InP/$In_{0.53}Ga_{0.47}As$ heterostructure (HS).

An InP/$In_{0.53}Ga_{0.47}As$ layer with thickness $t_b \approx 1$ μm and $p_0 \approx 10^{16}$ cm^{-3} and a top InP layer with $t_a \approx 1$ μm and $p_0 \approx 10^{16}$ cm^{-3} (Fig. 1) was grown on an InP substrate with hole density $p_0 \approx 10^{18}$ cm^{-3} by means of chloride vapor-phase epitaxy, which yields smooth heterojunctions with a transition region several hundred angstroms accross. An InGaAs layer with $n_0 \approx 10^{16}$ cm^{-3} was used in some HSs. The PL was investigated by illuminating the top InP layer by a cw He–Ne laser with photon energy $h\nu = 1.97$ eV, which is absorbed over a depth $\alpha^{-1} \approx 0.1$ μm (α is the absorption coefficient of such photons in InP), which is approximately equal to the thickness t_d of the space-charge region. For this reason, most of the excited electron–hole pairs apparently recombine at

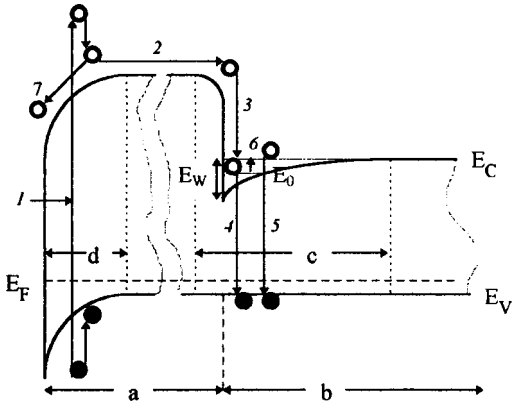

FIG. 1. Excitation scheme of PL in the HS (p)InP/$(p)$$In_{0.53}Ga_{0.47}As$: a — InP layer with $E_g=1.35$ eV; b — $In_{0.53}Ga_{0.47}As$ layer with $E_g=0.735$ eV; c — $In_xGa_{1-x}P_yAs_{1-y}$ transition region; d — space-charge region at the InP surface; *1* — excitation and thermalization of Δn and Δp in InP; *2* — diffusion of Δn into the InGaAs layer; *3* — trapping of Δn in levels of a TQW of depth E_w; *4* — PL from the lower level E_0 in the TQW; *5* — interband PL from InGaAs; *6* — thermal ejection of Δn from the TQW; *7* — trapping and annihilation of Δn at the surface; E_F, E_C, and E_V — Fermi level, conduction-band bottom, and valence-band top.

the InP surface, and only relatively few electron–hole pairs reach the InGaAs and excite PL in it. Despite this, the PL intensity in the InP was several orders of magnitude lower than in the InGaAs. The intensity of the PL lines of the InGaAs layer depended linearly on the excitation power, which varied from 0.05 to 5 W/cm^2, while the spectral shape and position of the PL lines remained unchanged. The quantity Q was determined taking into account the isotropic distribution of photons inside the sample and the angle of total internal reflection.[1] On account of the strong absorption of radiation in the substrate, only single reflection was taken into account.

In the experimental temperature range 77–295 K two InGaAs emission lines with characteristic properties were observed in the PL spectrum of the heterostructures — short-wavelength L_1 and long-wavelength L_2.

1. The L_1 line lies near the edge of the main absorption band of InGaAs, and its spectral shape and position are identical to the values computed according to the principle of detailed balance[3] from the measured absorption spectrum in the same sample (Fig. 2, curves *1*, *4*, and *5*). As the temperature decreases, this line shifts in the direction of high energies in accordance with the change in the band gap $E_g=(0.824-2.3\times10^{-4}T-2.39\times10^{-7}T^2)$ eV.[4]

2. The width at half maximum of the line L_1, amounting to 1.5 kT, increases with temperature, and the short-wavelength edge of the line falls off exponentially as $I\propto\exp[(h\nu_{\max}-h\nu)/kT]$ (Figs. 2 and 3), corresponding to a Boltzmann distribution for free nonequilibrium carriers.

The properties 1 and 2 attest to the fact that the L_1 line is due to the characteristic PL of InGaAs.

3. The line L_2 is separated from the L_1 line by an amount $\Delta=50$ meV for p-type

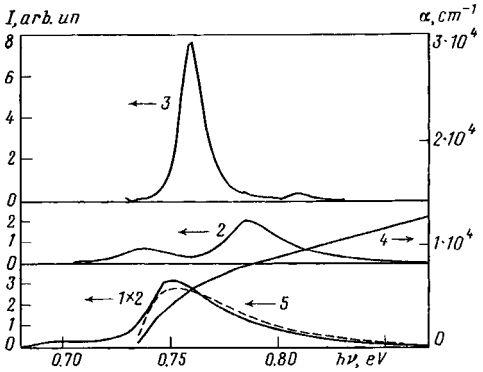

FIG. 2. PL spectra of the HS (*p*)InP/(*p*)InGaAs at $T=295$ K — curve *1*, 183 K (curve *2*), 77 K (curve *3*), absorption coefficient α at $T=295$ K (curve *4*) and computed PL (curve *5*).

InGaAs layers and 70 meV for *n*-type layers (Figs. 2 and 3). These separations vary for different samples within ± 3 meV.

4. The spectral shapes of both lines are identical to within the limits of the experimental accuracy (± 0.5 meV) at all temperatures (Figs. 2 and 3).

5. The quantum yield of the PL of both lines, defined in relation to the number of

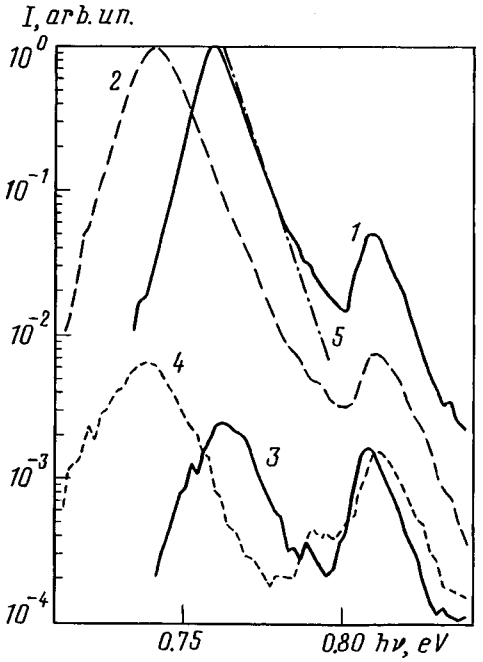

FIG. 3. PL spectra at $T=77$ K of the HSs (*p*)InP/(*p*)InGaAs (curve *1*) and (*p*)InP/(*n*)InGaAs (curve *2*), and the layers (*p*)InGaAs (curve *3*), and (*n*)InGaA (curve *4*), after removal of the top (*p*)InP layer; $I \propto \exp[(h\nu_{\max} - h\nu)/k \cdot 77\ \mathrm{K}]$ (curve *5*).

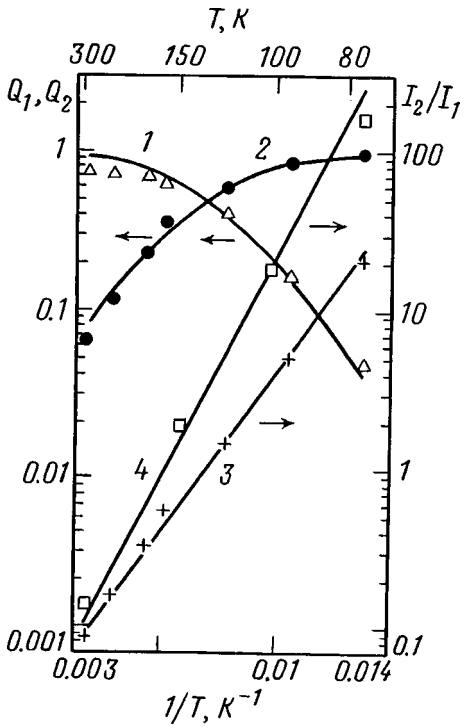

FIG. 4. Quantum yields of the intensities of the lines of the intersubband PL (Q_1, points on curve *1*) and from the TQW (Q_2, points on curve *2*) versus the reciprocal of the temperature for the HS (*p*)InP/(*p*)InGaAs. Curves *1* and *2* are the values of Q_1 and Q_2 computed from expressions (1) for the parameters $a=80$ and $\Delta=50$ meV. Ratios of the intensities of these lines I_2/I_1 for (*p*)InP/(*p*)InGaAs (straight line *3*, with slope corresponding to $\Delta=50$ meV) and for (*p*)InP/(*n*)InGaAs (straight line *4*, with slope corresponding to $\Delta=70$ meV).

exciting photons absorbed in the InP, had the values $Q'=0.13$ at $T=295$ K, 0.15 at 183 K, and 0.17 at 77 K.

6. The intensity ratio of the PL lines $I_2/I_1 \propto \exp(\Delta/kT)$ (Fig. 4).

7. At low temperatures $T \approx 77-150$ K the intensity of the L_1 line increases (the PL rises) with temperature as $I_1 \propto \exp(-\Delta/kT)$ and saturates at room temperature. The intensity of the PL of the L_2 line decreases (is quenched) with increasing T as $I_2 \propto \exp(\Delta/kT)$, while at low temperatures its intensity is independent of T (Fig. 4).

8. When the top InP layer is etched off, the PL intensity decreases strongly (approximately by a factor of 400) at both 77 K (Fig. 3) and 295 K, despite the fact that the InGaAs layer is excited directly. The spectrum of the interband PL line (L_1 line) does not change, while the spectrum of the long-wavelength PL does change (Fig. 3). The properties of the L_2 line differ sharply from the properties of the relatively weak ''interfacial'' PL line observed earlier at low temperatures $T \leqslant 15$ K in ordinary heterostructures[5] corresponding to our samples with the top InP layer removed.

Since the spectral shape of the L_2 line which we observed is similar to the spectrum

of the interband PL (L_1 line) of free nonequilibrium electrons Δn and holes Δp, the L_2 line is likewise due to the PL of free Δn and Δp. It is not a phonon replica of the L_1 line, since Δ does not equal the LO-phonon energy (32 meV).[4] The L_2 line is explained by the PL from the bottom subband of the TQW, formed for minority carriers, apparently, in the transition region at the HS interface during growth (Fig. 1). The TQW is due to the variable-gap $In_xGa_{1-x}P_yAs_{1-y}$ layer with an excess of In ($x \approx 0.8$), which ordinarily settles on the surface, at the interface and a deficit of P ($y \approx 0.2$), which ordinarily evaporates from the surface. This causes E_g to decrease by an amount equal to the well depth $E_w \approx 0.1$ eV. (Fig. 1). For the effective masses in InGaAs $m_e = 0.14\ m_0$ and $m_h = 0.33\ m_0$ (Ref. 6), the computed depths E_0 of the bottom level for electrons and holes in the TQW according to the formula $E_i = (\hbar^2/2m_{e,h})^{1/3}[1.5\pi E_w(i+3/4)/t_w]^{2/3}$, $i = 0, 1, 2, \ldots$, agree with the experimental values $\Delta_e = 50$ meV and $\Delta_h = 70$ meV for a well depth $E_w = 80-100$ meV and width of the TQW base $t_w = 300-700$ Å.

The properties 6 and 7 attest to the fact that the excited minority carriers in the conduction band with density of states N_C and in the TQW subband with density N_Z are in a quasi-equilibrium state, and the quantum yields Q_1 and Q_2 of the PL of the lines L_1 and L_2 are given by the relations

$$Q_1 = [1 + a^{-1}\exp(\Delta/kT)]^{-1}, \quad Q_2 = [1 + a\exp(-\Delta/kT)]^{-1}, \quad Q_1 + Q_2 = Q \equiv 1, \tag{1}$$

where $a = \gamma_1 N_C/(\gamma_2 N_Z)$ and γ_1 and γ_2 are, respectively, the coefficients of interband recombination and recombination from the TQW.

As one can see from Fig. 4, the experimental temperature dependences $Q_1(T)$ and $Q_2(T)$ are close to those calculated from expressions (1), attesting to the fact that the quantum yield relative to the number of electron–hole pairs reaching InGaAs is close to 1. The experimental values of $Q_1(T)$ for $T \geqslant 150$ K are somewhat smaller than the computed values, and as a result one has $Q = 0.75-0.8$ at $T = 295$ K. This is explained by the fact that at high temperatures T the nonequilibrium electrons thermally ejected from the TQW spread out over a large distance, as a result of which the probability of their nonradiative recombination at recombination centers increases. The rise of the characteristic luminescence with increasing temperature was not observed in previous works on recombination luminescence in crystals because of the dominance of nonradiative recombination of nonequilibrium electrons and holes, which are thermally ejected from the luminescence centers into the allowed bands.

It follows from the experiments that the TQW formed during growth of the HS under more nearly equilibrium conditions than, for example, in the case of molecular-beam epitaxy and therefore with a smaller number of defects makes possible intense trapping of nonequilibrium carriers and the subsequent radiative recombination of these carriers. It was determined from Fig. 4 and expressions (1) that for electrons in the TQW the ratio $\gamma_1 N_C/(\gamma_2 N_Z) = 80$, while for holes $\gamma_1 N_v/(\gamma_2 N_Z) = 120$. The feature that distinguishes the TQW from a square well[6] is intense luminescence occurring near the well as a result of the gentle slope of the potential of one of its edges. The results obtained can be used in low-brightness light sources as well as for lowering laser thresholds.

This work was supported by the Russian Fund for Fundamental Research under Grant 96-02-18151.

[a)]e-mail: nolle@ran.gpi.ru

[1] V. S. Vavilov, É. L. Nolle, and S. N. Maksimovskiĭ, Fiz. Tverd. Tela (Leningrad) **7,** 1558 (1965) [Sov. Phys. Solid State **7**, 1253 (1965)].
[2] A. Yu. Egorov, A. E. Zhukov, P. S. Kop'ev *et al.*, Fiz. Tekh. Poluprovodn. **30,** 1345 (1996) [Semiconductors **30**, 707 (1996)].
[3] W. van Roosbroeck and W. Shockley, Phys. Rev. **94**, 1558 (1954).
[4] P. K. Bhatacharya, M. V. Rao, and M. J. Tsai, J. Appl. Phys. **54**, 5096 (1983).
[5] P. W. Yu, C. K. Peng, and H. Morkoc, Appl. Phys. Lett. **54**, 1546 (1989).
[6] E. Tournie, K. H. Ploog, and C. Albert, Appl. Phys. Lett. **61**, 2808 (1992).

Translated by M. E. Alferieff

On the nature of the influence of an electric current on the magnetically stimulated microplasticity of Al single crystals

V. I. Al'shits,[a)] E. V. Darinskaya, E. Yu. Mikhina, and E. A. Petrzhik
Institute of Crystallography, Russian Academy of Sciences, 117333 Moscow, Russia

(Submitted 9 April 1998)
Pis'ma Zh. Éksp. Teor. Fiz. **67**, No. 10, 788–793 (25 May 1998)

A large increase in dislocation mobility in Al single crystals in a static magnetic field in the absence of mechanical loading of the samples is observed when a dc electric current of low density (10^5–10^6 A/m^2) is additionally passed through the samples. Apparently, the role of the current reduces to depinning of dislocations from strong pinning centers on the surface of the crystal as a result of surface electromigration of defects. This interpretation is supported by the fact that in samples whose surface is insulated by a layer of lacquer the passage of a current through the volume of the crystal does not change the ordinary dislocation mobility level in a magnetic field. It is hypothesized that surface electromigration of defects, which frees dislocations and unblocks dislocation sources, also plays a key role in the physical mechanism of the long-ago discovered macroplastification of metals upon the passage of an electric current through them. © *1998 American Institute of Physics.* [S0021-3640(98)01410-8]

PACS numbers: 62.20.Fe, 61.72.Lk, 66.30.Qa

As is well known, in the absence of external perturbations the position of dislocations in a crystal is determined by a complicated balance between the long-range internal stresses engendered by the dislocations themselves and the short-range barriers due to the potential relief of the lattice (Peierls–Nabarro relief), impurity centers, and other defects. One of the most widely used methods for lowering the internal stresses in crystals is annealing — holding at a high temperature. As a result, dislocations which overcome short-range barriers by thermal activation move so as to decrease the stored elastic energy and hence the average level of internal stresses.

There are alternative methods of bringing about relaxation of a dislocation structure. One such method is the relatively recently discovered magnetoplastic effect (MPE) in nonmagnetic crystals, which consists of depinning of dislocations from paramagnetic obstacles in a static magnetic field.[1] It is believed[2–4] that depinning occurs as a result of the evolution of the spin subsystem of dislocation–paramagnetic center interacting pairs, which occurs by a spin-dependent transition[5] that breaks down a local barrier. The MPE is manifested experimentally as a relaxation of the dislocation structure in samples placed

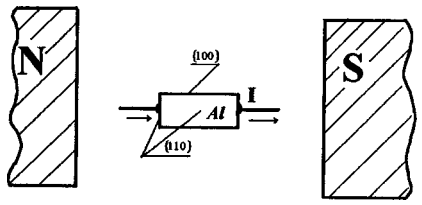

FIG. 1. Diagram of the experiment.

in a static magnetic field and as a substantial magnetosensitivity of the magnetoplasticity,[6,7] microhardness,[8] etc.

Significantly, the MPE is also observed in nonmagnetic metals, specifically, in zinc[9] and aluminum[10,11] single crystals. At the same time, there is also the well-known so-called ''electron–plastic'' effect,[12–16] which consists in the plastification of nonmagnetic metals when a pulsed electric current is passed through them. Unfortunately, the nature of this effect has never been convincingly interpreted. We shall return to this problem below at the level of individual dislocations within the framework of an investigation of dislocation travel distances in Al single crystals in the presence of both a static magnetic field and an electric current. As we shall see, such an unconventional approach in which two different effects are ''mixed'' not only does not confuse the picture but, on the contrary, it makes it possible to separate their contributions and to advance a substantiated hypothesis about the nature of the effect of an electric current on dislocation mobility.

The experiments were performed on spectrally pure (99.999%) Al samples cut in the form of approximately $3\times3\times8$ mm rectangular prisms from the same single crystal. The orientation of one pair of faces was chosen parallel to the system of {100} planes; the two other pairs of faces belonged to the system {110} (see Fig. 1). After the samples were cut out, their surfaces were chemically polished. Next, leads were soldered to their end faces. The positions of the edge dislocations, parallel to the $\langle 112\rangle$ direction with Burgers vector oriented along $\langle 110\rangle$, were fixed by means of selective chemical etching of the {100} faces in the samples to which leads had already been soldered. After the first etching a sample was placed in a static magnetic field $B=0.1-0.6$ T for a time t ranging from 10 min to 6 h. An electric current $I=2-9$ A was passed through the sample at the same time. Next, the {100} working surfaces of the sample were etched once again. This made it possible to reveal the dislocation travel distances and to determine according to their histogram the average dislocation travel distance under given conditions. The method for measuring dislocation travel distances is described in greater detail in Ref. 10.

The experiments showed that passing a dc current with density 10^5-10^6 A/m^2 through the Al samples appreciably increases the dislocation mobility in a magnetic field. Figure 2 displays two curves showing how the normalized average dislocation travel distance depends on the magnetic induction B and the holding time t of the samples in the magnetic field. The curves correspond to the case when an electric current $I=3$ A is passed through the sample during the holding time (curve *1*) and to the absence of such a current (curve *2*, points $\bigcirc$, $\triangle$, $\square$). Just as in previous investigations of the magnetoplastic effect in Al single crystals,[10] these curves turned out to be linear in B^2t, followed by saturation of the average travel distance at a level corresponding to the characteristic distance between dislocations ($\sim 1/\sqrt{\rho}$). One can see that even a weak (3 A) dc current

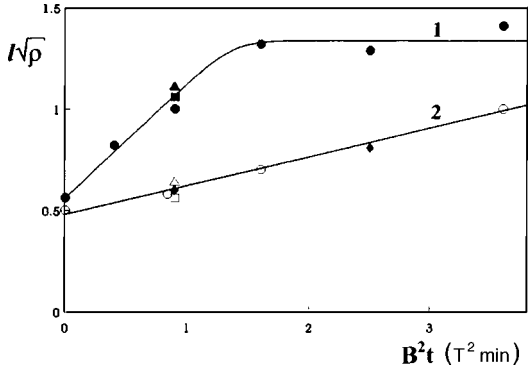

FIG. 2. Normalized average dislocation travel distance $l\sqrt{\rho}$ (ρ is the dislocation density) versus the magnetic induction B and the holding time t of the samples in a magnetic field with simultaneous passage of an electric current $I=3$ A (●, ▲, ■) and 5 A (♦) and in the absence of current (○, △, □); the experimental points ■, □ and ▲, △ correspond, respectively, to ''floating'' contacts and leads secured rigidly to the sample in a wooden retainer; the points ♦ refer to samples whose surface is coated with electrical insulation.

has a radical effect on the dislocation mobility. The background average travel distance l_0 for $B=0$ is due, as usual, to the relaxation of the dislocation structure as a result of the etching away surface or subsurface obstacles to the motion of the dislocations.[17] The relatively high level of l_0 in these experiments as compared with our data in Ref. 10 could be due to the more nonequilibrium dislocation structure formed as a result of the introduction of new dislocations into the sample in the process of soldering the leads. Moreover, it should be noted that the Al crystals used here were not the same ones as before, and also that a ''faster'' etchant was used in the present study.

Figure 3 shows the dependence of the same normalized average travel distance $l\sqrt{\rho}$ of dislocations on the current I in a fixed magnetic field $B=0.3$ T and with a fixed magnetic ''treatment'' time of the crystal $t=10$ min. A quasilinear increase of the travel

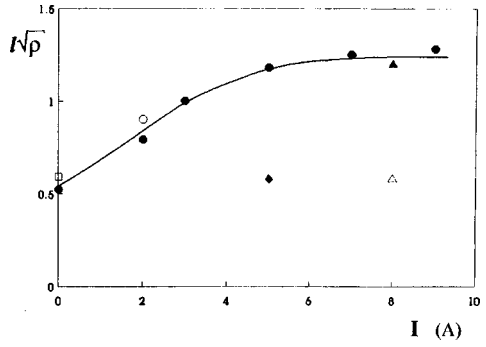

FIG. 3. Normalized average dislocation travel distance $l\sqrt{\rho}$ versus the electric current I for $B=0.3$ T (●, ○, ▲, □, ■) and $B=0$ (△) at temperatures of 293 K (●, ○, □, ♦) and 77 K (▲, △); the experimental points ●, ▲, △, ♦ correspond to the orientation $I \| B$, while the point ○ corresponds to $I \perp B$; the point □ corresponds to application of an additional mechanical load of 26 g/mm^2 (with $I=0$, $B=0.3$ T); the point ♦ refers to samples whose surface is coated with electrical insulation.

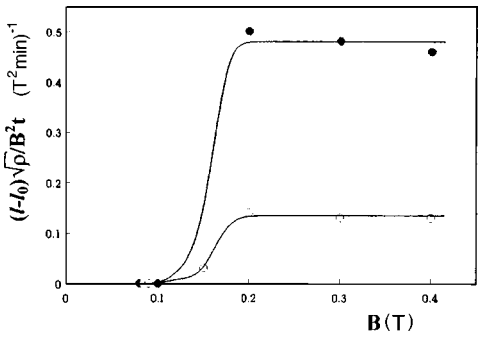

FIG. 4. $(l-l_0)\sqrt{\rho}/B^2t$ versus the magnetic induction B in the presence of electric currents of 3 A (●) and 6 A (○) and in the absence of current (○) (the points ○ are the data of Ref. 18).

distances, with a tendency toward saturation at approximately the same level as in Fig. 2, is observed. Significantly, the measured dependence is found to be practically insensitive to the relative orientation of the magnetic field and the electric current (to within the experimental error $\sim 15\%$, the points ● and ○ lie on the same curve). The observed effect is equally insensitive to a decrease of a temperature from room temperature to 77 K (the point ▲ in Fig. 3). We note that in the absence of a magnetic field on the crystal the passage of the same 8 A electric current at the same temperature 77 K has no effect on dislocation mobility — the average travel distance remains at the background level (the point △ in Fig. 3).

Actually, to eliminate the current-induced growth of the dislocation mobility it is not necessary to remove the magnetic field completely — it is sufficient to switch off the magnetoplastic effect, i.e., to decrease the magnetic induction B below a certain threshold value B_c. According to Ref. 18, for $B<B_c$ the spin–lattice relaxation processes, which randomize the spins, occur more efficiently than does the spin evolution in the magnetic field. As a result, the spin-dependent transitions in the magnetic field in the paramagnetic center–dislocation system are suppressed, and the magnetically stimulated depinning of dislocations ceases. The threshold field B_c is sensitive to the state of the paramagnetic centers. For example, x-ray irradiation decreases B_c.[18] It is of interest to determine whether or not an electric current influences the threshold field B_c. Our experimental check gives a definite ''no'' for the answer to this question. Figure 4 shows the step-like dependence of the slope of the linear part of the curves $l(B^2t)$ on the magnetic field (see Fig. 2) for $I=0$ (○) and $I=3$ A (●). As one can see from the figure, an electric current only increases the step height substantially in the region $B>B_c$, while leaving the position of the threshold field unchanged. Apparently, an electric current does not appreciably affect the elementary act of depinning of dislocations from paramagnetic centers in a magnetic field.

Let us now turn to the analysis of the possible mechanisms leading to the observed effect of an electric current on dislocation mobility. Judging from the observed temperature insensitivity of this effect (see Fig. 3), the reason cannot reduce to a direct thermal action of the current, which under our experimental conditions results in a slight heating of the samples (by 1–2°C at 3–4 A). However, such a heating could have an indirect effect, engendering contact stresses at the soldering location as a result of the difference

between the thermal expansion coefficients of tin and aluminum. An estimate shows that for a 3–4 A current the stresses are of the order of 10 g/mm^2, which according to our data is much too low to increase dislocation mobility appreciably. The experimental point □ in Fig. 3, corresponding to an additional mechanical load of 26 g/mm^2 applied to the sample simultaneously with a magnetic field $B=0.3$ T but no current $I=0$, attests to this.

Another possible source of additional current-induced parasitic loading of the sample is due to the torques arising at the soldering locations as a result of the force exerted by the magnetic field on the current-carrying leads. Of course, we endeavored to reduce these forces to a minimum by orienting the leads parallel to the magnetic field (Fig. 1). However, to eliminate completely the possible influence of the factor under study two other schemes for supplying current to the sample were also employed. In the first scheme the leads and the sample together were rigidly secured in a wooden retainer (see the experimental points ▲ and △ in Fig. 2), while the second scheme employed ''floating'' contacts between the leads and the sample through a conducting emulsion (the points ■ and □ in Fig. 2). It is easy to see that the average dislocation travel distance l is practically independent of the method by which current is supplied to the sample.

As it turned out, the nature of the observed effect of an electric current on dislocation mobility by no means reduces to instrumental effects. Our old data from a study of the MPE in NaCl crystals during continuous etching prompted an idea for solving the riddle.[2] According to our observations, under conditions of continuous dissolution of the surface the average delay time that the dislocations remain at the ''start'' after a magnetic field is switched on is an order of magnitude shorter than in the ordinary experimental method where etching is conducted before and after magnetic ''treatment'' of the sample. It is natural to assume that constant etching eliminates strong pinning of dislocations by highly mobile surface defects which quickly accumulate on the crystal surface from the surrounding medium. On the other hand, in the standard method of visualizing dislocations many dislocations are held back at the ''start'' by strong obstacles on the surface, waiting until other dislocations approach and forcefully detach the first dislocations from surface defects. This process can be of a relay-race character and can be very prolonged.

Let us assume that in our experiments the role of the electric current reduces to depinning dislocations from surface defects as a result of, for example, electromigration of the latter. Then, on the one hand, all the experimental data presented above appear obvious. On the other hand, we now have a simple method for eliminating the influence of an electric current without actually switching the current off. For this it is sufficient to block the surface component of the current. An experiment to verify this was performed as follows. After the first etching, which fixes the initial positions of the dislocations, the surface of the sample was covered with a layer of lacquer. Then the sample was placed in a magnetic field $B=0.3$ or 0.5 T and a current $I=5$ A was passed through the sample for 10 min. Subsequently the lacquer was removed with a solvent and the {100} surface was etched again. The corresponding experimental points ◆ in Figs. 2 and 3, as expected, fall at the same level as the average dislocation travel distance in samples through which no current was passed at all.

Therefore the observed effect of an electric field on dislocation mobility in a magnetic field apparently has no direct relation to the MPE. However, the fact that in our experiments this effect is observed only in the existence region of the MPE ($B>B_c$) is very important evidence. It reflects the fact that an electric current itself does not promote

detachment of dislocations from point defects in the bulk of the crystal, but it can effectively influence dislocation mobility when combined with other actions, including, for example, a mechanical load. This particular combination was used in the experiments performed by Troitskiĭ *et al.*[12–15] while they were observing the plasticizing effect of an electric field in the macrostraining of metal samples. They employed current pulses with density 10^8-10^9 A/m^2, duration $\sim 10^{-4}$ s, and repetition frequency 2–400 Hz, which was chosen so as to optimize the effect without allowing appreciable electric heating of the samples. The effect was observed in regimes of stress relaxation,[13] creep,[14] and active loading.[15] The attempts made in Refs. 12 and 16 to explain it involve in one way or another the concept of dislocation drag in a metal by a directed electron flux. Meanwhile, the existing theory of such drag effects[19,20] predicts their onset at current densities two to three orders of magnitude higher than that in the experiments of Refs. 12–15. Moreover, direct dislocation drag by an electric current in copper has indeed been directly observed visually[21] in an electron microscope at current densities above a threshold of the order of 10^{11}A/m^2.

In summary, the nature of the ''electron–plastic'' effect is unlikely to have any relation to the electron drag of dislocations. In the light of our data it is natural to conjecture that the effect is due to depinning of dislocations from surface defects and unblocking of surface sources of dislocations as a result of electromigration of defects along the surface. This hypothesis correlates well with the strong influence of surface factors, which has been reliably established, on the macroplastic properties of metals.[22] It is not difficult to check this conjecture directly in exactly the same way that we did in the present work: by electrically insulating the surface of the samples.

We are grateful to B. I. Smirnov and O. V. Klyavin for a helpful discussion of the results and N. I. Noskova for assisting in the work. This work was supported by the Russian Fund for Fundamental Research under Grant 97-02-16327.

[a)]e-mail: alshits@mechan.incr.msk.su

[1] V. I. Al'shits, E. V. Darinskaya, T. M. Perekalina, and A. A. Urusovskaya, Fiz. Tverd. Tela (Leningrad) **29**, 467 (1987) [Sov. Phys. Solid State **29**, 265 (1987)].
[2] V. I. Al'shits, E. V. Darinskaya, and E. A. Petrzhik, Fiz. Tverd. Tela (Leningrad) **33**, 3001 (1991) [Sov. Phys. Solid State **33**, 1694 (1991)].
[3] M. Molotskii and V. Fleurov, Phys. Rev. Lett. **78**, 2779 (1997).
[4] V. I. Al'shits, E. V. Darinskaya, and O. L. Kazakova, Zh. Éksp. Teor. Fiz. **111**, 615 (1997) [JETP **84**, 338 (1997)].
[5] Ya. B. Zel'dovich, A. L. Buchachenko, and E. L. Frankevich, Usp. Fiz. Nauk **155**, 3 (1988) [Sov. Phys. Usp. **31**, 385 (1988)].
[6] Yu. I. Golovin and R. B. Morgunov, JETP Lett. **61**, 596 (1995).
[7] A. A. Urusovskaya, V. I. Al'shits, A. E. Smirnov, and N. N. Bekkauer, JETP Lett. **65**, 497 (1997).
[8] Yu. I. Golovin, R. B. Morgunov, D. V. Lopatin, and A. A. Baskakov, Phys. Status Solidi A **160**, R3 (1997).
[9] V. I. Al'shits, E. V. Darinskaya, I. V. Gektina, and F. F. Lavrent'ev, Kristallografiya **35**, 1014 (1990) [Sov. Phys. Crystallogr. **35**, 597 (1990)].
[10] V. I. Al'shits, E. V. Darinskaya, and E. A. Petrzhik, Fiz. Tverd. Tela (Leningrad) **34**, 155 (1992) [Sov. Phys. Solid State **34**, 81 (1992)].
[11] V. I. Al'shits, R. Voska, E. V. Darinskaya, and E. A. Petrzhik, Fiz. Tverd. Tela (St. Petersburg) **35**, 70 (1993) [Phys. Solid State **35**, 37 (1993)].
[12] O. A. Troitskiĭ, JETP Lett. **10**, 11 (1969).
[13] O. A. Troitskiĭ and P. U. Kalymbetov, Fiz. Met. Metalloved. **51**, 1056 (1981).
[14] V. I. Stachenko, O. A. Troitskii, and V. I. Spitsyn, Phys. Status Solidi A **79**, 549 (1983).

[15] O. A. Troitskiĭ, M. M. Moiseenko, and V. I. Spitsin, Dokl. Akad. Nauk SSSR **274**, 587 (1984) [Sov. Phys. Dokl. **29**, 71 (1984)].
[16] O. A. Troitskiĭ, A. M. Roshchupkin, V. I. Stashenko *et al.*, Fiz. Met. Metalloved. **61**, 990 (1986).
[17] V. B. Pariĭskiĭ, A. I. Landau, and V. I. Startsev, Fiz. Tverd. Tela (Leningrad) **5**, 1377 (1963) [Sov. Phys. Solid State **5**, 1002 (1963)].
[18] V. I. Al'shits, E. V. Dariņskaya, O. L. Kazakova *et al.*, JETP Lett. **63**, 668 (1996).
[19] V. Ya. Kravchenko, Zh. Éksp. Teor. Fiz. **51**, 1676 (1966) [Sov. Phys. JETP **24**, 1135 (1967)].
[20] V. B. Fiks, Zh. Éksp. Teor. Fiz. **80**, 2313 (1981) [Sov. Phys. JETP **53**, 1209 (1981)].
[21] E. E. Vdovin and A. Yu. Kasumov, Fiz. Tverd. Tela (Leningrad) **30**, 311 (1988) [Sov. Phys. Solid State **30**, 180 (1988)].
[22] V. P. Alekhin, *Physics of Strength and Plasticity of the Surface Layers of Materials* [in Russian], Nauka, Moscow, 1983.

Translated by M. E. Alferieff

Discrete tunneling of holes in porous silicon

E. S. Demidov, V. V. Karzanov, and V. G. Shengurov
N. I. Lobachevskiĭ Nizhniĭ Novgorod State University,[a] 603600 Nizhniĭ Novgorod, Russia

(Submitted 13 April 1998)
Pis'ma Zh. Éksp. Teor. Fiz. **67**, No. 10, 794–797 (25 May 1998)

It is pointed out that in the partial oxidation of porous silicon (PS) formed on heavily doped crystals, the topology of the pores can result in the formation of an anisotropic material with strings of nanometer-sized silicon granules embedded in insulating silicon dioxide SiO_2. In this range of granule sizes the correlation effects in the tunneling of electrons (holes) are strong on account of their Coulomb interaction. This should be manifested as discrete electron and hole tunneling at temperatures comparable to room temperature. The room-temperature current–voltage characteristics of $n^+-PSp^+-p^+$ diode structures with a PS interlayer on p^+-Si, which exhibit current steps on the forward and reverse branches, are presented. The current steps are attributed to discrete hole tunneling along the silicon strings in SiO_2. © *1998 American Institute of Physics.* [S0021-3640(98)01510-2]

PACS numbers: 72.80.Ng, 72.80.Cw, 72.20.Jv

Most of the interest in porous silicon (PS) centers on the possibility of obtaining red-yellow and even blue luminescence, which is attributed to nanosize quantum constraints on the band states of electrons.[1,2] In the case when the PS is formed on heavily doped *n*- or *p*-type crystals a surprising, as yet incomprehensible, mechanism of self-organization accompanying anodic dissolution of silicon can lead to the formation of an ordered system of pores approximately 10 nm in diameter, which at $\sim 50\%$ porosity are separated by a distance of almost the same length. This can be seen in an electron micrograph of a cleaved surface of a PS layer on n^+-Si (KÉS-0.01), presented in Ref. 3. A similar picture was later observed in our PS layers formed on p^+-Si (KDB-0.01, KDB-0.005) crystals. In the present letter we call attention to the fact that because of the topology of the pores, partial oxidation of PS can lead to the formation of an anisotropic material with strings consisting of silicon granules with a diameter of several nanometers embedded in insulating silicon dioxide SiO_2. On account of the low electrical capacitance between the strings a Coulomb blockade of electron or hole tunneling should appear along the strings at temperatures of the order of room temperature. Here we present room-temperature current–voltage characteristics (IVCs) for diode structures with a PS interlayer, which exhibit the current steps that are characteristic for discrete tunneling. Such porous silicon could be of practical interest for single-electron electronics with a maximum working frequency of up to 10^{13} Hz, as was shown by Likharev.[4]

Let us clarify the proposed mechanism of string formation. Experiments show that a 2–3 nm thick SiO_2 layer forms on a silicon surface during a simple holding period of

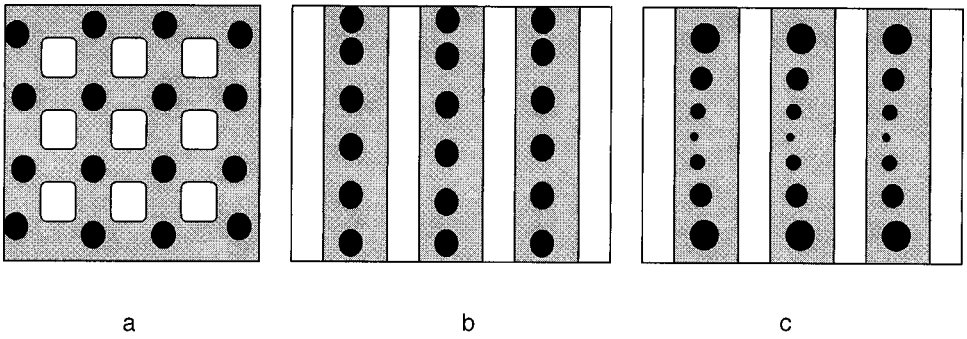

FIG. 1. Schematic representation of porous silicon: a — top view, b — side view in the case of uniform pores (strings of identical granules), c — side view in the case of nonuniform pores (strings consisting of granules with different diameters). Gray background — SiO_2, black circles — silicon granules.

several hours in air at room temperature. If the pores were uniform in cross section, then silicon filaments approximately 5 nm in diameter would evidently form, as shown schematically in Fig. 1a. But, according to the electron micrographs mentioned above, the pores are modulated in diameter with a step length less than or of the order of this diameter. A silicon filament is transformed into a string (or ''garland'') of silicon granules, each with a diameter of the order of the diameter of the filament (see Fig. 1b), possibly because the narrow places are oxidized completely through or because the narrow places are broken by mechanical stresses at the $Si–SiO_2$ boundary and the breaks are filled in by silicon dioxide through diffusion. An estimate of the electrical capacitance C between 5 nm granules with a SiO_2 insulating barrier with dielectric constant $\epsilon=4$ and the same thickness gives the value 1.5×10^{19}F, which corresponds to a Coulomb barrier $e^2/2C=0.5$ eV. This is 20 times greater than kT at $T=290$ K and, according to Fig. 1 in Ref. 4, should cause an appreciable nonlinearity of the room-temperature IVC of a tunneling contact. Moreover, the filaments are likely to be nonuniform over long distances. At some distance from the surface of the PS the weakest spot will contain several granules with the smallest diameter, as shown in Fig. 1c. This can be stimulated by a change in current during anodization of the silicon. Such a weak spot will largely determine the IVC of a string.

Figure 2 shows the IVCs of one of the $n^+–PSp^+–p^+$ diode structures with a transverse diameter of 0.5 mm. A $2–3\,\mu$m thick layer of PS was formed on p^+-Si (KDB-0.01) and allowed to stand in air at room temperature for one day. Next, an n^+-Si layer with resistivity $\sim0.01\ \Omega\cdot$cm was grown on it epitaxially by the technology of Ref. 5. The details of the technology will be described in greater detail elsewhere. For comparison, the IVC of an identical $n^+–p^+$ diode but without the PS interlayer is displayed in Fig. 2. It exhibits the standard asymmetric form with high currents on the reverse branch on account of tunneling of charge carriers through the $p–n$ junction.

As one would expect, all the diodes with a PS interlayer had lower currents at a given voltage than ordinary diodes in both the forward and reverse directions. They exhibited a large variance, evidently because of the different density of the PS at different locations on the surface of the crystal. The most pronounced current steps occurred on the diodes with the highest resistance in the forward and reverse directions, as in Fig. 2. They

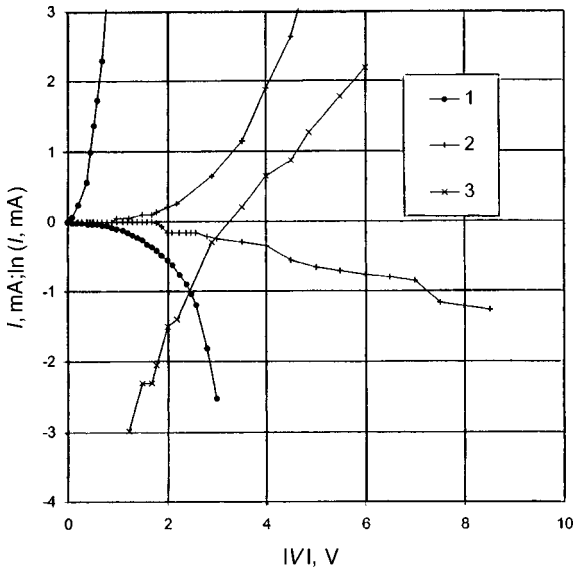

FIG. 2. IVCs of diodes: ● — n^+-p^+ diodes, × — $n^+-\mathrm{PS}p^+-p^+$ diodes, + — forward branch of the IVC on a semilogarithmic scale for an $n^+-\mathrm{PS}p^+-p^+$ diode.

are seen more clearly on the reverse branch of the IVC of the diodes, where the processes are not complicated by electron injection from the n^+ layer. As one can see from Fig. 2, this branch is on the average close to a linear dependence, as should be the case for electron or hole tunneling through insulating barriers. Several current steps, each 150–300 μA high, are observed. The current steps are not due to irreversible changes in the PS, since the IVCs are nonhysteretic. According to the estimates presented above, the first current jump on the reverse branch near 2 V could signify that at a weak spot of each string tunneling occurs through one granule with a diameter of ~ 1 nm or through three or four granules with diameters of 5 nm, with a Coulomb barrier e^2/C_Σ and a series capacitance C_Σ, and from behind a likely barrier of about 2 eV at the boundary between the n^+-Si layer and the PS layer. The fact that current steps start at lower voltages on the forward branch attests to the latter possibility. The intervals between the first steps equal about 0.5 V, which agrees with the above estimate of a Coulomb blockade for 5 nm in diameter granules. The subsequent current steps on the forward branch of the IVC for diodes with a PS layer occur at approximately the same voltages as on the reverse branch. This is seen more clearly in the curve of the logarithm of the current versus the voltage in Fig. 2.

At present it is difficult to relate position of the current steps to the characteristics of tunneling in partially oxidized PS, which is more complicated than the systems analyzed quantitatively thus far, with one or two metal granules between metal ''plates,''[4,6] more complicated both with respect to the number of intercoupled conducting granules and on account of their semiconductor nature. It is natural to expect both short- and long-range coupling between the strings on account of the lateral (weaker than the longitudinal) tunneling exchange of electrons between granules in neighboring strings and lateral electric-field interaction as well as on account of the exchange of electromagnetic quanta

with energy $\nu = I_g/e$, where I_g is the current in a string. The role of doping with shallow impurities is not completely understood, though the asymmetric form of the IVCs in Fig. 2 for the diodes containing PS attests to the fact that boron, a shallow acceptor impurity, in nanosize silicon granules possesses a sufficiently low ionization energy to determine the type of conductivity in the granules. The fact that shallow impurities remain electrically active agrees with the observation made in Ref. 7 that the ESR of PS is influenced by the type of impurity. The known acceptor levels at a $Si-SiO_2$ interface, which play an increasingly larger role with decreasing granule size, and the field-induced ''doping'' due to the proximity of the n^+ region in our diodes also promote hole conduction. For this reason, and also on account of the asymmetry of the IVC for diodes with a PS layer, we conjecture that discrete tunneling occurs. The situation here is also more complicated than in the metal version because of the large value of the Debye screening length. Finally, it should be noted that although the correlation effects of the Coulomb interaction of electrons or holes ''overtake'' the quantum size effects in the electron spectrum, for granule sizes of several nanometers both are very likely to influence the IVCs of diodes containing PS. In any case, the presence of well-expressed current steps attests not only to the small variance in the parameters of a large number of tunneling contacts connected in parallel but also to a kind of self-organization in a system of active oscillators, similar to the self-organization occurring in lasers. It is likely that future investigations at different temperatures and attempts to observe the emission spectrum of diodes containing PS will elucidate the nature of the current steps and the possibility of microwave generation.

We are grateful to S. A. Gusev for the electron mictrographs of our samples, which were taken at the Institute of Metal Phyiscs of the Russian Academy of Sciences.

This work was supported by the Interdisciplinary Science and Technology Program ''Electronic Materials'' under Grant 223–MP15.

[a)]e-mail: ett@phys.unn.runnet.ru

---

[1] P. K. Kashkarov and V. Yu. Timoshenko, Priroda, No. 12, 12 (1995).
[2] R. T. Collins, P. M. Fauchet, and M. A. Tischler, Phys. Today **50**(1), 24 (January 1997).
[3] S. A. Gusev, N. A. Korotkova, D. B. Rozenshteĭn *et al.*, Pis'ma Zh. Tekh. Fiz. **20,** 50 (1994) [Tech. Phys. Lett. **20**, 450 (1994)].
[4] K. K. Likharev, Mikroelektronika **16**, 195 (1987).
[5] V. G. Shengurov, V. N. Shabanov, N. V. Gudkova, and B. Ya. Tkach, Mikroelektronika **22**, 19 (1993).
[6] I. M. Ruzin, V. Chandrasekhar, E. I. Levin, and L. I. Glazman, Phys. Rev. B **45**, 13469 (1992).
[7] E. S. Demidov, V. G. Shengurov, N. E. Demidov, and V. N. Shabanov, Fiz. Tekh. Poluprovodn. **28,** 701 (1994); **28**, 1503 (1994) [Semiconductors **28**, 417 (1994); **28**, 841 (1994)].

Translated by M. E. Alferieff

Investigations of the magnetic structure of the surface and volume of aluminum-substituted Sr–*M* type hexaferrites

A. S. Kamzin[a)] and V. L. Rozenbaum
A. F. Ioffe Physicotechnical Institute, Russian Academy of Sciences, 194021 St. Petersburg, Russia

L. P. Ol'khovik
Kharkov State University, 310077 Kharkov, Ukraine

(Submitted 13 April 1998)
Pis'ma Zh. Éksp. Teor. Fiz. **67**, No. 10, 798–802 (25 May 1998)

The magnetic structure of the surface layer of single crystals of hexagonal ferrites of the type Sr–*M* ($SrFe_{12}O_{19}$) in which some iron ions are replaced by diamagnetic Al ions is investigated, in direct comparison with the magnetic structure in the bulk of the sample, by the method of simultaneous gamma, x-ray, and electron Mössbauer spectroscopy. It is found that under conditions of diamagnetic dilution of the magnetic lattice of hexagonal ferrites of the type Sr–*M* by Al ions, a layer ~200 nm thick in which the orientation of the magnetic moments is not collinear with the direction of the moments in the bulk of the sample is observed on the surface of $SrFe_{10.2}Al_{1.8}O_{19}$ crystals. Thus a ''transitional'' surface layer has been observed on macroscopic ferromagnetic crystals. © *1998 American Institute of Physics.* [S0021-3640(98)01610-7]

PACS numbers: 75.70.Ak, 75.50.Dd

Since the beginning of the 1970s, investigators have been devoting increasing attention to the study of the magnetic properties of surfaces. This is due to a need to understand the influence of a ''defect'' such as a surface on the formation of the properties of the surface layer and on the processes occurring in the surface layer in the presence of fundamental phenomena in the volume of the crystal. These investigations are important from the applied standpoint because, for example, an understanding of the mechanisms responsible for the formation of the magnetic properties of nanosize crystallites will make it possible to produce magnetic information storage media with ultrahigh writing density.

The existence of surface anisotropy was predicted theoretically by Néel in 1954.[1] To interpret the experimental results the concept of the influence of the surface was invoked to explain the fact that the saturation magnetization of fine γ-Fe_2O_3 powders[2] is less than that of macroscopic samples. It was suggested in Ref. 2 that a nonmagnetic (magnetically dead) surface layer ~6 Å thick exists on crystallite faces, while in Ref. 3 similar data on γ-Fe_2O_3 were explained by a change in the magnetic structure of crystallite surfaces. A ''shell'' model[6,7] was proposed to describe the experimental data obtained on fine

α-Fe_2O_3,[4] $CrFe_2O_4$,[5] γ-Fe_2O_4, $NiFe_2O_4$, CrO_2, $Dy_2BiFe_5O_{19}$, and $BaFe_{12}O_{19}$ powders (see Refs. 6 and 7 and the references cited therein), specifically, the magnetic structure of the interior of a crystallite is similar to that of a bulk sample, while the distribution of the magnetic moments in a thin surface layer is noncollinear.

However, other models are also used to explain the experimental data on powders. For example, it is supposed that angular ordering of spins with many stable configurations which transforms into a spin-glass state as temperature decreases exists on the surface of $NiFe_2O_4$ particles; a disordered shell is present in $CoFe_2O_4$ and Fe_3O_4 crystallites; a noncollinear arrangement of the spins in γ-Fe_2O_3 particles occurs not only on the surface (see Ref. 8 and the references cited therein).

It should noted that superparamagnetic phenomena, the strong dependence of the properties of fine powders on the preparation technology, and so on make it much more difficult to interpret surface phenomena for such objects. The situation simplifies substantially in the case of the surface properties of macroscopic crystals.

In 1972 Krinchik *et al.*[9] showed that surface anisotropy can be observed experimentally in macrocrystals of antiferromagnets with weak ferromagnetism (AWF). In Ref. 10 it was proposed that a ''transition layer'' where the orientation of the magnetic moments changes as the surface is approached exists on the surface of hematite. Later, a transition layer $\sim$500 nm thick was discovered in the AWFs $FeBO_3$,[11,12] $ErFeO_3$ and $TbFeO_3$.[13]

A substantial step in investigations of the surface properties of crystals was made with the aid of a new method of simultaneous gamma, x-ray, and electron Mössbauer spectroscopy (SGXEMS), proposed in Ref. 14 and described in Ref. 15. The uniqueness of the SGXEMS method lies in the fact that information about the state of the surface layer and the volume of the crystal is extracted simultaneously.

The SGXEMS method has been used to obtain direct experimental confirmation of the existence of a $\sim$400 nm thick ''transitional'' surface layer in the AWF Fe_3BO_6.[16] However, a ''transitional'' surface layer has not been observed, within the limits of the experimental accuracy ($\sim$10 nm), in the hexagonal ferrites $BaFe_{12}O_{19}$, $SrFe_{12}O_{19}$, and $PbFe_{12}O_{19}$.[17]

In the present work we investigated the magnetic structure of the surface layer of macroscopic crystals (in direct comparison with the structure of the volume of the sample) of Sr-*M* type hexagonal ferrites in which some iron atoms are replaced by diamagnetic Al ions. Ferrites with the chemical formula $SrFe_{10.2}Al_{1.8}O_{19}$, which were synthesized by spontaneous crystallization from a fluxed solution of $NaFeO_2$, were chosen for the investigations. The fact that the crystals are type-M ferrites with a hexagonal structure and the chemical formula were confirmed by x-ray and Mössbauer investigations, chemical analysis, and the value of the Curie temperature. Wafers in the form of disks $\sim$80 μm thick and $\sim$8 mm in diameter were prepared from the single crystals. The crystallographic *C* axis was directed perpendicular to the plane of wafers. The surface properties were investigated on $SrFe_{10.2}Al_{1.8}O_{19}$ and $SrFe_{12}O_{19}$ single crystals with a natural, highly reflecting face, which were boiled in nitric acid or chemically polished by etching in orthophosphoric acid for 1 min at 90 °C.

The measurements were performed by the SGXEMS method[14,15] based on simultaneous detection of the Mössbauer spectra in radiations possessing different ranges in the material, namely, gamma rays (GRs), characteristic x rays (XRs), and secondary (con-

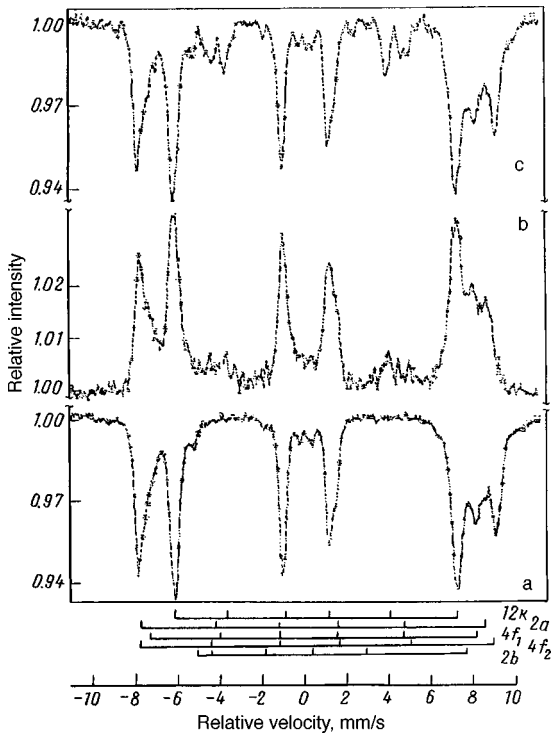

FIG. 1. Room-temperature Mössbauer spectra of single crystal hexaferrite $SrFe_{10.2}Al_{1.8}O_{19}$: a and c — with detection of γ rays carrying information about the volume of the crystal; b — with detection of secondary electrons from a surface layer from 0 to 200 nm. For a and b the wave vector of the γ rays is parallel to the crystalline *C* axis, while for c the wave vector of the γ rays makes an angle of 28° with the crystallographic *C* axis.

version and Auger) electrons (SEs), which carry information about the properties of the volume, surface layers with a thickness of several μm and with thickness up to 300 nm of a bulk crystal, respectively, was used for the measurements.

Figure 1 shows the Mössbauer spectra obtained by the SGXEMS method at room temperature with GR and SE detection in the case when the wave vector of the γ rays was oriented parallel to the crystallographic *C* axis. One can see that the spectral lines are well resolved. This makes it possible to calculate with a high degree of accuracy the tilt angle (θ) of the magnetic moments with respect to the wave vector of the γ rays from the ratio of the intensities of the first and second (as well as fifth and sixth) lines of the Zeeman sextuplets using the formula

$$A_{1.6}/A_{2.5}=3(1+\cos^2\theta)/(4\sin^2\theta). \quad (1)$$

Analysis of the Mössbauer spectra obtained by detecting GRs (Fig. 1a) showed that in the Zeeman sextuplets of each nonequivalent position of the iron ion the intensities of the first and fifth lines, corresponding to transitions with $\Delta m=0$ equal zero. Therefore the magnetic moments of the iron ions occupying positions in the volume of the crystal

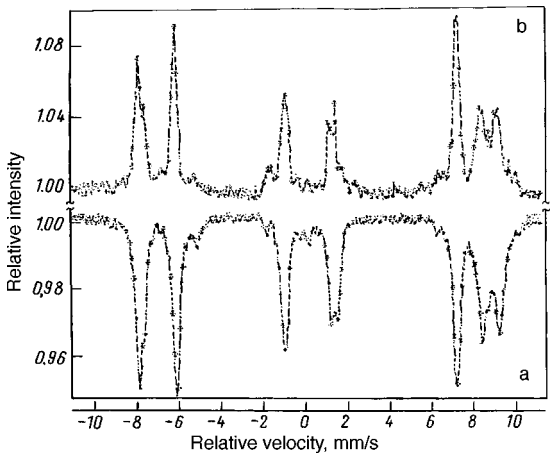

FIG. 2. Room-temperature Mössbauer spectra obtained from a $SrFe_{12}O_{19}$ single crystal by detecting: a — γ rays carrying information about the volume of the crystal and b — secondary electrons from a surface layer from 0 to 200 nm. The wave vector of the γ rays is parallel to the crystallographic C axis.

are parallel to both the wave vector of the γ rays and the crystallographic C axis. This agrees well with the published data on the volume properties of these crystals (see, for example, Ref. 18 and references cited therein).

Weak lines are observed in the spectra obtained by detecting SEs (Fig. 1b) on the sections corresponding to velocities ± 4 and ± 5 mm/s. Analysis showed that these are the second and fifth lines of the Zeeman sextuplets. This means that the magnetic moments of the iron ions occupying sites in a ~ 200 nm thick surface layer are tilted away from both the direction of the wave vector of the γ rays and the crystallographic C axis. Calculations performed using Eq. (1) showed that this tilt angle equals $\theta = 23 \pm 2°$.

To check this conclusion we performed the following experiment. Mössbauer spectra of $SrFe_{10.2}Al_{1.8}O_{19}$ single crystals, inclined so that the crystallographic C axis made an angle α with the wave vector of the γ rays, were obtained. As one can see from Fig. 1c, the second and fifth lines appeared in the spectrum obtained by detecting γ rays for $\alpha = 28 \pm 2°$, and in addition they are observed in the same velocity intervals ± 4 and ± 5 mm/s as in Fig. 1b. The angle θ calculated from Eq. (1) using the ratios of the line intensities in the spectrum obtained with an inclined sample (Fig. 1b) equals $29 \pm 2°$ and is the same as the angle α fixed by the experimental conditions.

The results obtained prove convincingly that the magnetic moments of iron atoms located in a ~ 200 nm thick surface layer are tilted away from the direction of both the crystallographic C axis and the spins of the iron ions occupying positions in the volume of the crystal.

It can be conjectured that the observed tilting of the magnetic moments is due to the fact that during the chemical polishing of the crystals magnetic ions are ''etched out'' of the surface layer and the exchange interaction energy in this layer decreases. To check this conjecture Mössbauer spectra of $SrFe_{12}O_{19}$ single crystals prepared by the same chemical-polishing technology simultaneously with the $SrFe_{10.2}Al_{1.8}O_{19}$ crystals investigated were obtained. One can see from Fig. 2 that the second and fifth lines of the

Zeeman sextuplets are absent in the spectrum obtained by detecting both electrons and γ rays. Therefore our surface preparation technology cannot lead to the observed spin noncollinearity.

The tilting of the orientation of the magnetic moments in the surface layer away from the direction in the volume can be explained as follows. It is well known (see Refs. 18–20 and the references cited therein) that the substitution of diamagnetic ions for iron ions in type-M hexaferrites results in (when a certain density of diamagnetic ions is reached) the formation of a noncollinear magnetic structure in the crystal. The Al ion content in our $SrFe_{10.2}Al_{1.8}O_{19}$ crystals was too low to destroy the collinearity in the volume. However, the exchange interaction energy in the surface layer of the crystals investigated decreases not only because magnetic bonds are broken by the diamagnetic ions which are introduced but apparently also because of the presence of the surface. Thus, it was shown in Ref. 21 that the replacement of only 9% of the iron ions in Fe_3BO_6 with diamagnetic Ga ions increases by an order of magnitude the thickness of the ''transitional'' surface layer. On the basis of what we have said above we assume that the noncollinear magnetic structure in the surface layer of $SrFe_{10.2}Al_{1.8}O_{19}$ crystals arises because of an additional decrease of the exchange interaction energy near the surface.

In summary, it was shown experimentally that a $\sim$200 nm thick surface layer in which the direction of the magnetic moments of the iron ions is not collinear with the crystallographic *C* axis, while the magnetic moments of ions located in the volume of the crystal are oriented parallel to the *C* axis, exists in Sr-*M* type hexagonal ferrites with diamagnetic substitution. An anisotropic surface layer, whose existence was predicted theoretically by L. Néel in 1954,[1] was observed in ferrites.

This work was supported by the Russian Fund for Fundamental Research under Grant 98-02-18279.

[a)]e-mail: kamzin@kas.ioffe.rssi.ru

[1] L. Neel, J. Phys. Radium **15**, 225 (1954).
[2] A. E. Berkowitz, W. J. Schuele, and P. J. Flanders, J. Appl. Phys. **39**, 1261 (1968).
[3] J. M. D. Coey, Phys. Rev. Lett. **27**, 1140 (1971).
[4] A. M. van der Kraan, Phys. Status Solidi A **18**, 215 (1973).
[5] A. E. Berkowitz, J. A. Lahut, and C. E. van Buren, IEEE Trans. Magn. **MAG-16**, 184 (1980).
[6] K. Haneda, Can. J. Phys. **65**, 1233 (1987).
[7] K. Haneda and A. H. Morrish, Nucl. Instrum. Methods Phys. Res. B **76**, 132 (1993).
[8] D. Lin, A. C. Nunes, C. F. Majkrzak *et al.*, J. Magn. Magn. Mater. **45**, 343 (1995).
[9] G. S. Krinchik, A. P. Khrebtov, A. A. Askochenskiĭ, and V. E. Zubov, JETP Lett. **17**, 335 (1973).
[10] G. S. Krinchik and V. E. Zubov, Zh. Éksp. Teor. Fiz. **69**, 707 (1975) [Sov. Phys. JETP **42**, 359 (1976)].
[11] V. G. Labushkin, V. V. Rudenko, É. R. Sarkisov *et al.*, JETP Lett. **34**, 544 (1981).
[12] V. E. Zubov, G. S. Krinchik, V. N. Seleznev, and M. B. Strugatsky, J. Magn. Magn. Mater. **86**, 105 (1990).
[13] E. A. Balykina, E. A. Gan'shina, and G. S. Krinchik, Zh. Éksp. Teor. Fiz. **93**, 1879 (1987) [Sov. Phys. JETP **66**, 1073 (1987)]; Fiz. Tverd. Tela (Leningrad) **30**, 570 (1988) [Sov. Phys. Solid State **30**, 326 (1988)].
[14] A. S. Kamzin, V. P. Rusakov, and L. A. Grigoriev, in *Proceedings of the International Conference on the Physics of Transition Metals*, USSR, 1988, Part II, p. 271.
[15] A. S. Kamzin and L. A. Grigor'ev, Pis'ma Zh. Tekh. Fiz. **16**, 38 (1990) [Sov. Tech. Phys. Lett. **16**, 616 (1990)].
[16] A. S. Kamzin and L. A. Grigor'ev, JETP Lett. **57**, 557 (1993); Zh. Éksp. Teor. Fiz. **104**, 3489 (1993) [JETP **77**, 658 (1993)].
[17] A. S. Kamzin, L. P. Ol'khovik, and V. L. Rozenbaum, JETP Lett. **61**, 936 (1995); Zh. Éksp. Teor. Fiz. **111**, 1426 (1997) [JETP **84**, 788 (1997)].

[18] O. P. Aleshko-Ozhevskiĭ, Ya. Litsievich, A. Murasik, and I. I. Yamzin, Kristallografiya **19**, 391 (1974) [Sov. Phys. Crystallogr. **19**, 240 (1974)].
[19] G. Albanese, A. Deriu, L. Lucchini, and G. Slokar, Appl. Phys. A **26**, 45 (1981).
[20] A. Collomb, X. Obrados, and D. Fruchart, J. Magn. Magn. Mater. **69**, 317 (1987).
[21] A. S. Kamzin, L. A. Grigor'ev, and S. A. Kamzin, Fiz. Tverd. Tela (St. Petersburg) **36**, 1399 (1994) [Phys. Solid State **36**, 765 (1994)].

Translated by M. E. Alferieff

Periodic character of the phase transformation in steel accompanying reflection of converging shock waves from the center of focusing

A. É. Kheĭfets,[a)] N. Yu. Frolova, and V. I. Zel'dovich
Institute of Metal Physics, Ural Branch of the Russian Academy of Sciences, 620219 Ekaterinburg, Russia

B. V. Litvinov and N. P. Purygin
Russian Federal Nuclear Center, 454070 Snezhinsk, Russia

(Submitted 14 April 1998)
Pis'ma Zh. Éksp. Teor. Fiz. **67**, No. 10, 803–807 (25 May 1998)

Special conditions in an experiment on the loading of low-carbon steel by converging shock waves made it possible to obtain residual microstructural changes of a periodic character, with a period of the order of 0.2 mm, which are associated with a phase transformation caused by waves reflected from the center of focusing. A model explaining the periodicity of the microstructure and making it possible to predict the behavior of materials under similar conditions is proposed. © *1998 American Institute of Physics.* [S0021-3640(98)01710-1]

PACS numbers: 81.40.Vw, 62.50.+p, 64.70.Kb

An St3 steel sphere 60 mm in diameter was subjected to the action of the explosion of a spherical explosive charge 5 mm thick. The explosion was initiated at 12 points uniformly distributed on the surface of the sphere. To preserve the sample, a massive metallic case with an inner diameter of 80 mm,[1] which slowed down the unloading process, was used in the experiment. After loading, the sample was cut in half in order to perform metallographic investigations.

Figure 1 displays the surface of a diametral cross section of the sample. The presence of an air gap between the explosive and the case resulted in the formation of a cavity with an average diameter ~ 10 mm at the center of the sphere. A cavity did not appear in similar experiments performed without an air gap.[2] Chemical etching of the surface revealed figures of different etchability (Al'tshuler figures), which inherited the dodecahedral symmetry of the shock-wave loading. In these figures the properties of the sample are altered by the action of a dodecahedral converging shock wave moving away from the surface of the sphere (Fig. 1). Besides the Al'tshuler figures, radially arranged stripes of altered structure (Fig. 2) with period ~ 0.2 mm are also seen. The spherically symmetric arrangement of the stripes attests to the fact that they were formed by the ''reflected'' shock wave diverging away from the center of the sphere. The reflected compression wave is spherically symmetric, since the initial conditions of the shock-wave motion are ''forgotten'' by the time the converging shock wave is focused.

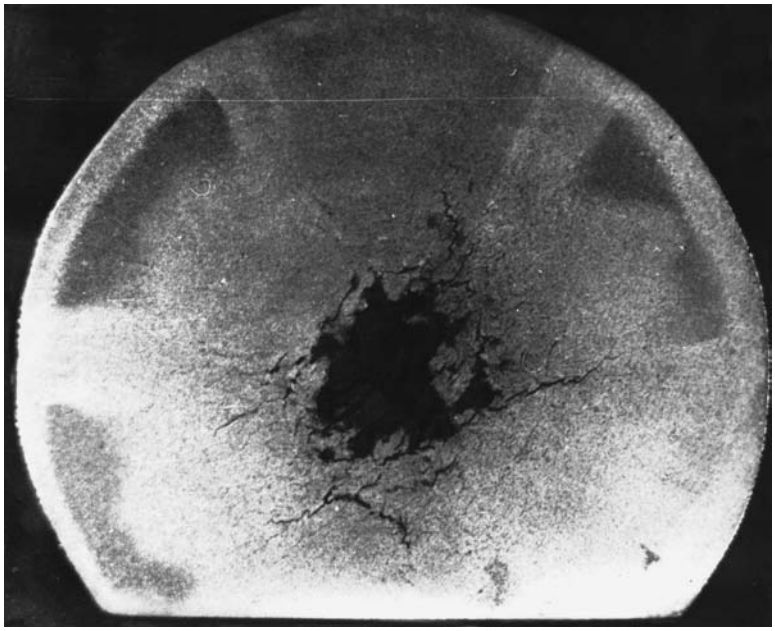

FIG. 1. Diametral section of the sample. Cavity and Al'tshuler figures ($\times 1.65$).

Metallographic and electron microscopic investigations of the striped structure showed that under the action of the shock wave $\alpha \rightarrow \epsilon \rightarrow \alpha$ transformation cycles occurred in the dark-etching stripes, i.e., formation a high-pressure ϵ phase accompanied by a jump in molar volume $\Delta V = 0.38$ cm^3/mole with the density of the initial α phase $\rho_\alpha = 7.86$ g/cm^3 occurred.[3] There are no traces of $\alpha \rightarrow \epsilon \rightarrow \alpha$ transformations in the light-colored stripes. The periodic character of the phase transformations under shock-wave loading is quite unusual and merits a more detailed study.

The effect of an air gap in the experiment is that the pressure profile of the converging shock wave becomes peaked and the wave of unloading moving away from the surface of the sphere lags behind the shock front by a distance that is much shorter than the radius of the sample. This is why the wave reflected from the center starts to play a more important role in the formation of the final structure of the sample and can be studied independently of the converging wave, since it moves along the unloaded material.

Let us consider a small volume element V of the sphere bounded by radii r_2 and r_1 within a solid angle Ω (Fig. 3). Let $r_2 \approx r_1 \approx r$. Evidently, $V \approx lS$, where $l = r_2 - r_1$, while $S = r^2\Omega$. Since the shock wave diverging from the center is damped, while $r_2 > r_1$, for mass velocities $u_1 = u(r_1)$ and $u_2 = u(r_2)$ at distances r_1 and r_2, respectively, from the center of the sphere we have $u_1 > u_2$. The mass velocity decreases with time as a result of the deceleration of the moving material of the sphere by stresses arising in the process of isentropic deformation of the sample after the passage of the shock wave. The isentropic deformation is quite slow compared with the shock-wave process, so that to a first approximation the mass velocity can be assumed to depend only on the radius provided

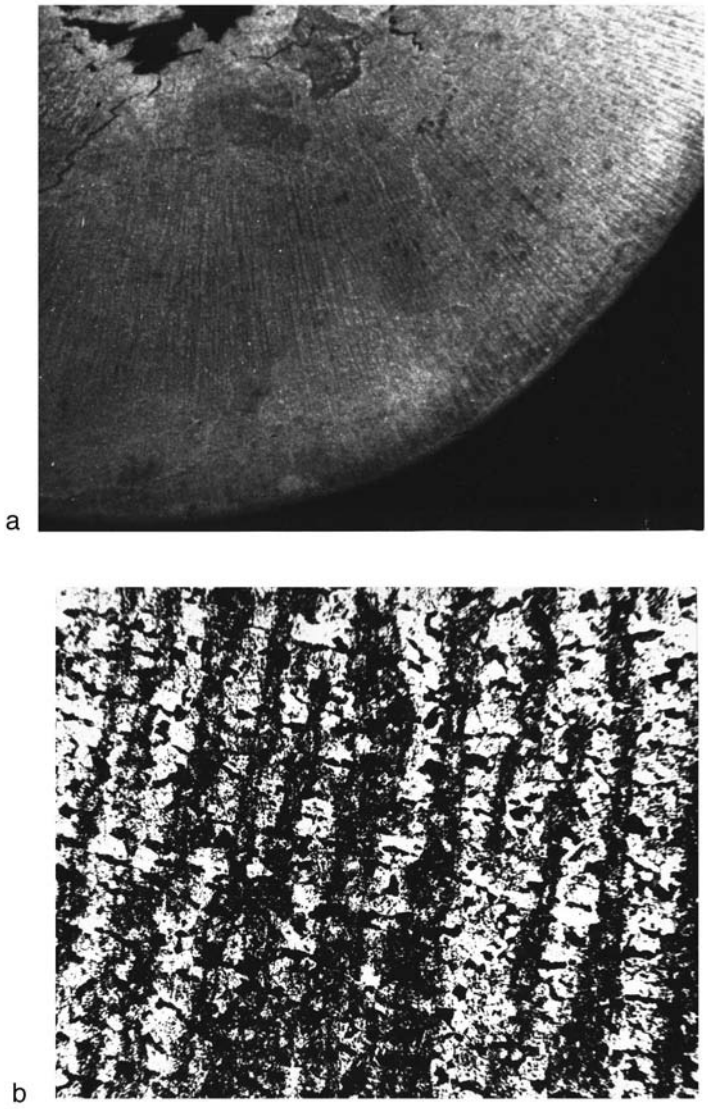

FIG. 2. Radial stripes: a — macrostructure (×2.8); b — microstructure (×50).

that the time interval considered is short, i.e., $du/dt \cong 0$ and $dr/dt = u(r)$. Under the condition that the derivative du/dt is small, the value of u can be related with the radial deformation Δr as $\Delta r \cong u\tau$, where τ is the duration of the flow. The deformation Δr is related with the cavity size r_0 by the conservation of the volume of the material in the sample: $(r+\Delta r)^3 - r_0^3 = r^3$.

Let us calculate the change in the volume V with time. Evidently, the following relations hold:

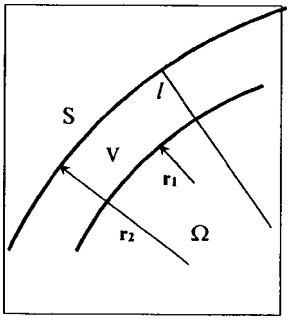

FIG. 3. A volume element of the sphere (see text for explanation).

$$\frac{dl}{dt}=u_2-u_1\cong u_r l<0, \quad \frac{dS}{dt}=2r\Omega\frac{dr}{dt}=2ru(r)\Omega>0,$$

i.e.,

$$\frac{dV}{dt}=r^2\Omega u_r l+2ru\Omega l, \quad \frac{1}{V}\frac{dV}{dt}=u_r+\frac{2u}{r},$$

$$V=V_0\exp\left[\left(u_r+\frac{2u}{r}\right)t\right]=V_0 f(t,r). \tag{1}$$

The terms $u_r t$ and $2ut/r$ appearing in the exponential are responsible for, respectively, the radial compression of matter and the stretching of an element S of the surface of the sphere. Since the ϵ phase in iron is a high-pressure phase, compression of the volume V is a necessary condition for the ϵ phase to appear in the experiment. This condition is equivalent to the assertion $u_r+2u/r<0$, which is valid in the present experiment. The formation of a region with an ϵ phase as the more dense phase in the initial α matrix results in partial relaxation of the stresses responsible for the radial compression of the material, and this is why the radial growth of the region is energetically favored. However, as the size of the region in its section by the surface of the sphere increases, the stresses due to the stretching of the spherical layer of matter and retarding the growth of the ϵ phase both in the region under study and in the surrounding environment increase. Therefore the formation of the observed striped structure can be explained qualitatively by self-consistent growth of the ϵ phase under the conditions of competing (promoting and suppressing) stimuli. The question of the continuity of the ϵ-phase stripes in the radial direction falls outside the scope of the present work, though it is quite obvious that the stripes should be interrupted in a manner so as to ensure the same total deformation of the material as a result of the phase transformation along any radius of the sphere. The characteristic length of a stripe in this case can be comparable to the dimensions of the sample. We shall confine our analysis to a small volume of the striped structure whose linear dimensions are comparable to the period of the stripes.

Information transfer between the ϵ-phase stripes in a spherical layer at a distance r from the center of the sphere occurs by means of elastic disturbances of the matrix which propagate with the speed of sound c. We shall label quantities corresponding to the α and

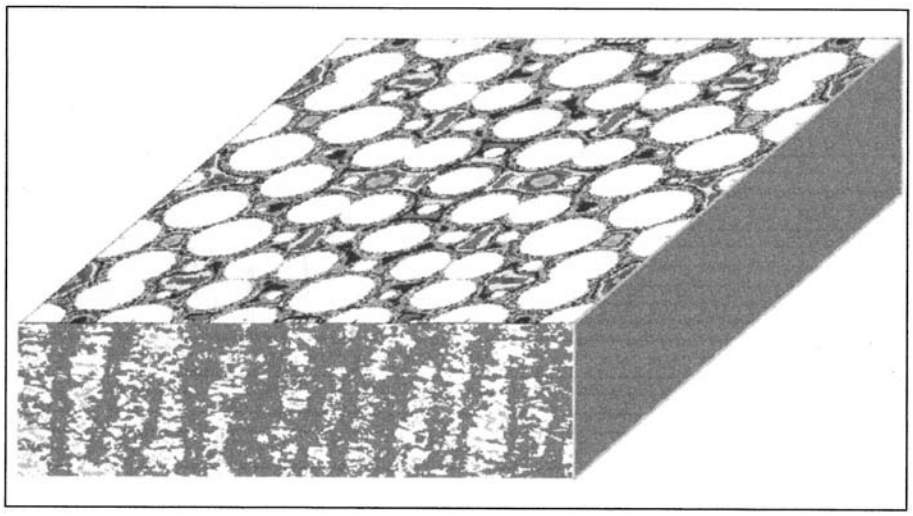

FIG. 4. Simulation results (top face of a parallelepiped) compared with the real striped structure (lateral face). White sections — ϵ phase. Regions of equal deformation of the matrix are marked by the same color. The distance from the center of the sample is 15 mm.

ϵ phases by indices α and ϵ. We call the surface density $\sigma=\rho l$, l being the thickness of the spherical layer and ρ the conventional density. We denote by β the quantity

$$\beta=\frac{\rho_\alpha}{\rho_\epsilon}=\frac{\sigma_\alpha/l}{\sigma_\epsilon/l}=\frac{\sigma_\alpha}{\sigma_\epsilon}.$$

Since $\rho=m/V=m/Sl$ and $\sigma=m/S\sim 1/S$, we have $\beta=S_\epsilon/S_\alpha$. Let an ϵ-phase section with area S_ϵ form at the point $\mathbf{r}_0$ on the surface of the sphere. The ''gain'' in the area will be $\Delta S=(1/\beta-1)S_\epsilon$. The surface density $\sigma_\alpha(t,\mathbf{r})$ at the point $\mathbf{r}$ will change by a factor of approximately $\pi|\mathbf{r}-\mathbf{r}_0|^2/(\pi|\mathbf{r}-\mathbf{r}_0|^2+\Delta S)$ in a time $\Delta t=|\mathbf{r}-\mathbf{r}_0|/c$. If n stripes centered at r_i, $i=1, 2, \ldots, n$, arise and start to grow on the section of the spherical surface that we are studying, then the surface density of matter at the point r will change in time by a factor of η:

$$\eta=\frac{\sigma_\alpha(\mathbf{r},t)}{\sigma_0(\mathbf{r},t)}=\prod_{i=1}^{n}\left\{1+\frac{(1-\beta)}{\beta\pi|\mathbf{r}-\mathbf{r}_i|^2}S_\epsilon\left(t-\frac{|\mathbf{r}_i-\mathbf{r}|^2}{c}\right)\right\}^{-1}, \tag{2}$$

where $\sigma_0(\mathbf{r},t)$ is the surface density neglecting the effect of the stripes but taking into account the radial stretching.

Let us examine the evolution of the striped structure in a cellular space with cell volume V_s and an element of area S_v on the surface of the sphere. Let m_v be the mass of the matter in a cell, V_α and V_ϵ the volumes occupied by the α and ϵ phases, respectively, and

$$m_v=V_s\rho=V_\alpha\rho_\alpha+V_\epsilon\rho_\epsilon, \quad V_\alpha+V_\epsilon=V_s.$$

Since $\sigma_\alpha/\sigma_0=\rho_\alpha(\mathbf{r},t)/\rho_0$, and taking account of Eq. (1), we obtain $\rho/\rho_\alpha=n/f$. Bearing in mind that $V_{\alpha,\epsilon}=S_{\alpha,\epsilon}l$, we obtain

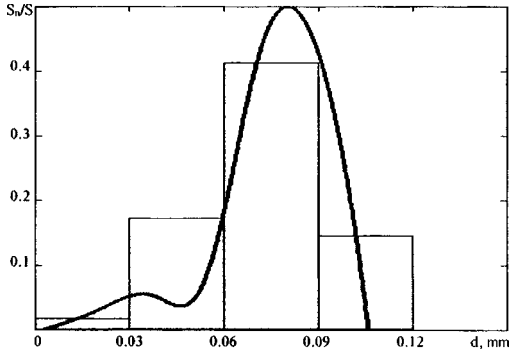

FIG. 5. Computed distribution function of the area occupied by ϵ-phase particles on the surface of the sphere over the sizes of these particles in comparison with the experimental histogram of the striped structure. The distance from the center of the sample equals 15 mm.

$$\frac{S_\epsilon}{S_\nu} = \frac{(\eta - f)\beta}{(1-\beta)f}. \tag{3}$$

The relations (1)–(3) formed the basis of a model that makes it possible to follow the evolution of the striped structure at an arbitrary point of the sphere. The period of the lattice in the cellular space was set at a value that is certainly less than the distance between the stripes. It was assumed that the section of a stripe by the surface of the sphere is a circle. This made it possible to simplify the calculations without substantial loss of generality of the model.

The simulation shows rapid growth of the ''selected'' ϵ-phase regions, while the growth of all other nuclei is suppressed. The distance between the large nuclei increases with time. The process stops when the computed period equals the experimentally observed value (Fig. 4). At this moment the isentropic flow of the sphere stops, and therefore the flow duration τ can be estimated. At a distance 15 mm from the center of the sphere $\tau \cong 30$ μs.

Figure 5 shows the computed distribution function of the area occupied by ϵ-phase particles over the sizes of these particles in comparison with the experimental histogram of the striped structure. The sharp maximum in the function corresponds to the average width of a stripe in the photograph of the microstructure (Fig. 2).

In summary, a periodic structure was observed to arise in steel when a spherical sample was loaded by converging shock waves. A model explaining the formation of the periodic striped structure and making it possible to follow its evolution in an arbitrary region of the sample as well as to estimate the isentropic flow time of the material of the sphere was proposed. This model can be used to predict the behavior of other materials possessing a high-pressure phase and to select shock-wave loading conditions under which periodic structural changes will appear in such materials.

[a)]e-mail: physmet@ifm.e-burg.su

[1] V. I. Buzanov and N. P. Purygin, in *Proceedings of the 10th Symposium on Combustion and Explosion* [in Russian], Chernogolovka, 1992, p. 131.
[2] B. V. Litvinov, V. I. Zeldovich, O. S. Rinkevich *et al.*, J. Phys. IV Coll. C8, Suppl. J. Phys. III **4**, 399 (1994).
[3] E. Yu. Tonkov, *Phase Transformations of Compounds at High Pressure*, Vol. 1 [in Russian], Metallurgiya, Moscow, 1988.

Translated by M. E. Alferieff

Nonchiral ferroelectric smectic-*C* films

P. O. Andreeva, V. K. Dolganov[a)]
Institute of Solid State Physics, Russian Academy of Sciences, 142432 Chernogolovka, Moscow Region, Russia

C. Gors and R. Fouret
Laboratoire de Dynamique et Structure des Materiaux Moleculaires, Universite de Lille 1, UFR de Physique, 59655 Villeneuve d'Ascq, France

E. I. Kats
Laboratoire de Spectrometrie Physique, Universite Joseph-Fourier Grenoble 1, BP87-Saint-Martine D'Heres, Cedex, France; Landau Institute for Theoretical Physics, Russian Acadmy of Sciences, 117940 Moscow, Russia

(Submitted 16 April 1998)
Pis'ma Zh. Éksp. Teor. Fiz. **67**, No. 10, 808–813 (25 May 1998)

Free-standing films of nonchiral liquid crystal compound are studied by optical reflectivity measurements. The existence of macroscopic ferroelectric properties and orientation of the tilt plane parallel to an electric field in the temperature range above the smectic-*C*–smectic-*A* bulk transition is demonstrated. © *1998 American Institute of Physics.* [S0021-3640(98)01801-5]

PACS numbers: 77.84.Nh, 77.80.Dj

Since the discovery of ferroelectric liquid crystals by Meyer *et al.*[1] it is usually assumed that the phenomenon (ferroelectricity) is possible only in the chiral smectic-*C** phase (Sm*C**), which has the polar symmetry group C_2. In this case the polarization can be written as $\mathbf{P}=P[\mathbf{n}\times\mathbf{z}]$, where $\mathbf{n}$ is the director[2] and $\mathbf{z}$ is a unit vector orthogonal to smectic layers (Fig. 1). Thus the necessary conditions for $\mathbf{P}\neq 0$ are a finite tilt angle ($\theta \neq 0$) and the presence of a molecular dipole perpendicular to the long axis of molecules.

Orientational order in tilted smectic phases (Sm*C** and Sm*C*) can be characterized by a two-component order parameter $\psi=\theta\exp(i\varphi)$ or equivalently by a vector $\mathbf{c}$ (the so-called $\mathbf{c}$-director[2]) determining the preferred (due to the tilt) direction in a layer. In the Sm*C** phase, each successive layer is rotated through a certain angle relative to the preceding one, so that a twisted structure with a certain pitch (determined by chirality) is formed. Therefore as one goes along the z coordinate, the director $\mathbf{n}$ (as well as the $\mathbf{c}$-director) and the polarization vector, which is directed along the C_2 axis (i.e., orthogonal to the tilt plane), rotate.

Note, however, that there is no direct correspondence between the chirality of the molecules and the existence of macroscopic ferroelectric properties or structures formed by them. For example, nonchiral and nonferroelectric smectic-*A* structures in chiral materials are well known. The search of for examples of the opposite situation (namely,

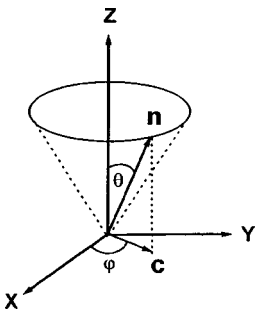

FIG. 1. Schematic structure of the Sm*C* phase; **z** is the unit vector of the layer normal, **n** is the director, **c** is the **c**-director.

nonchiral analogs of ferroelectric liquid crystals) is ''still a challenge to researchers'' (Ref. 3).

In this paper we demonstrate the existence of a simple nonchiral smectic-*C* structure possessing ferroelectric properties, e.g., having a macroscopic polarization **P** which (unlike the case of Sm*C**) is parallel to the tilt plane. Let us imagine that due to certain specific conditions (see below) the modulus $|\mathbf{c}|$ of the **c**-director varies continuously from layer to layer, while the orientation of **c** does not rotate (since we have no chirality). In such a structure a ferroelectric polarization **P** parallel to the tilt plane should appear. Surprisingly the structure can be realized easily in freely suspended smectic films.

Freely suspended films consist of an integer number of smectic layers. The planes of the smectic layers are aligned parallel to the film surface. Usually due to surface tension and specific interactions on the surface, large surface-ordering effects are observed above the bulk Sm*C*–Sm*A* transition temperature T_c (Refs. 4–8). The surface tilt appears at a temperature of about 20 °C above the bulk transition temperature.[4,5] It has also been shown that above T_c the Sm*C* phase occurs in the films.[4,6] In this temperature range the tilt is a function of the distance from the surface.

Figure 2a illustrates the essential features of freely suspended Sm*C* films above T_c.

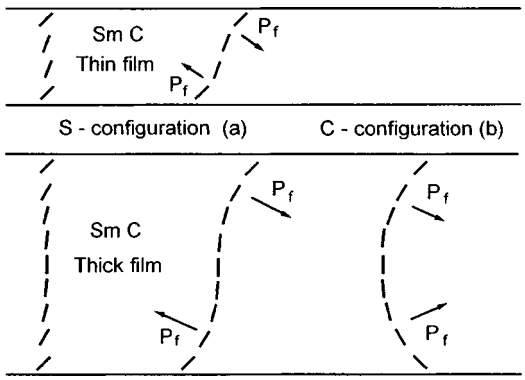

FIG. 2. Orientation of the molecules in thin and thick Sm*C* films above the bulk transition temperature. *S*-like and *C*-like configurations are shown for a thick film. **P** is the ferroelectric polarization.

Let us note that it is exactly the same structure as we need for our model of nonchiral ferroelectric smectics. The symmetry of the structure allows the existence of ferroelectric polarization **P** parallel (!) to the tilt plane. For an *S*-like configuration the direction of **P** is different at the top and at the bottom of the film. Above the bulk transition temperature the tilt angle θ decays with distance from the surface and becomes very small (nearly zero) for distances larger than bulk correlation length (at the center of the film, if the film thickness is larger than this correlation length). As a result the orientations of the **c**-director in the layers of the top part of the film are not coupled (or are only negligibly coupled) with the orientations of the **c**-director for the layers of the bottom part of the film.

In the presence of an electric field **E**, the two parts of the film can be oriented independently. Consequently, for thick films a *C*-like configuration is favored in the electric field above the bulk transition temperature. The tilt arrangement of *C*-like configuration is anticlinic (see also Ref. 9), i.e., the top and the bottom of the film are tilted in opposite directions. The net polarization **P** is parallel to the tilt plane (and to the vector **c**). In thin films (with thickness less than the bulk correlation length) there is a tilt at the center of the film (Fig. 2), and in this case *C*-like configuration can not be realized.

Our model was tested with optical reflectivity measurements. The experimental techniques have been described elsewhere.[9,10] Optical reflection from the film was measured in the ''backward'' geometry. The incident light was linearly polarized. An electric field from 3 to 20 V/cm was applied in the plane of the film. Our sample was the compound p-decyloxybenzoic acid-p-n-hexyloxyphenyl ester (DOBHOP). In optical measurements bulk samples exhibited the following phase transitions: Sm*C* (78 °C) – Sm*A* (83 °C) – nematic (89 °C) – isotropic. Free-standing films were spread across a 6 mm hole in a glass holder. The bulk Sm*A*–nematic transition temperature and the step-by-step thinning of the film[11,12] determine the stability limit of thick films. So, for thick films (several tens of layers) the maximum temperature of the measurements was restricted to about 83 °C. X-ray diffraction measurements of θ on a bulk sample were made using a curved linear position-sensitive multidetector and a curved quartz monochromator ($\lambda = 1.5406$ Å).

When the light is normally incident on the film, the reflection intensity is given by[13]

$$I(\lambda) = \frac{(n^2-1)^2 \sin^2(2\pi n N d/\lambda)}{4n^2 + (n^2-1)^2 \sin^2(2\pi n N d/\lambda)}, \tag{1}$$

where d is the interlayer distance ($d \simeq 3$ nm in the Sm*A* phase), n is the index of refraction and N is the number of layers. In the Sm*C* films with an in-plane anisotropy of the reflectivity index, two reflection spectra can be measured (for the plane of polarization of the light oriented parallel and orthogonal to the tilt plane). The reflected intensity and the wavelength of the reflectivity minimum for a thick film ($\lambda_{\min} = 2nNd/k$, $k = 1,2,3,\ldots$) depend on the index of refraction and should differ for the two polarizations. The reflection spectra were measured in electric fields oriented parallel ($\mathbf{E}_{||}$) and perpendicular ($\mathbf{E}_{\perp}$) to the plane of polarization of the light. This method enabled us to investigate the orientation of the tilt plane and the behavior of the average tilt angle θ.

We found that above T_c, thick films are oriented by a weak electric field ($\simeq 3$ V/cm). Figure 3 provides evidence for the field–induced orientation. The wave-

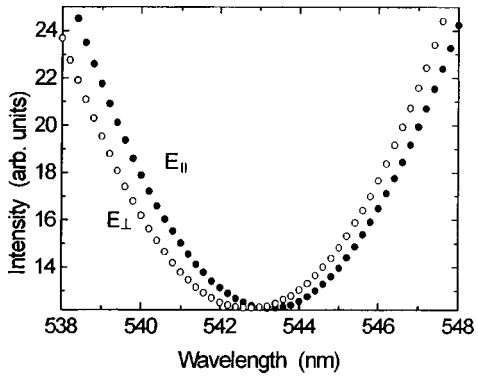

FIG. 3. Field induced tilt plane orientation in a SmC film ($N \simeq 60$, $T = 81.2$ °C). The wavelengths of the reflectivity minima λ_{min} differ for two directions of the electric field **E**, parallel ($\mathbf{E}_{||}$) and perpendicular ($\mathbf{E}_{\perp}$) to the plane of polarization of light.

lengths of the reflectivity minima λ_{min} are different for the two polarizations of the light. That means orientation of the tilt planes. When the direction of the electric field is switched ($\mathbf{E}_{||} \rightarrow \mathbf{E}_{\perp}$) the reflection spectra exchange theirs positions. Figure 4a shows the response of the optical reflection intensity when the direction of the electric field is switched.

Let us stress that the electrooptic response was observed above the bulk transition temperature T_c. Near the phase transition we observed that the orientation of the film differed from the orientation at high temperature. This behavior of DOBHOP is connected with deformation of the $S-$configuration in an electric field. Below T_c at low temperature uniformly oriented films could not be obtained in a weak electric field for the

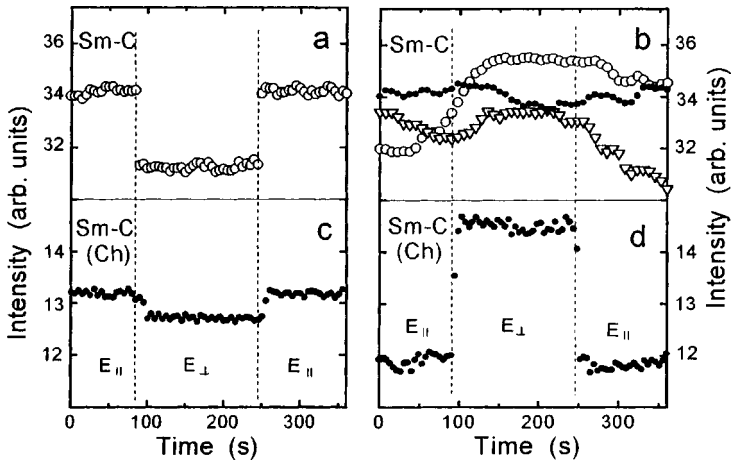

FIG. 4. Optical reflectivity intensities for nonchiral smectic film (DOBHOP) at temperatures above (80 °C (a)) and below (77 °C (b)) the bulk Sm$C-$SmA transition temperature ($\lambda_{min} - \lambda \simeq 20$ nm). Smectic liquid crystal DOBHOP with chiral component above (78.3 °C (c)) and below (72.3 °C (d)) the bulk transition temperature ($N \simeq 60$). The electric field is applied parallel ($\mathbf{E}_{||}$) and perpendicular ($\mathbf{E}_{\perp}$) to the light polarization plane.

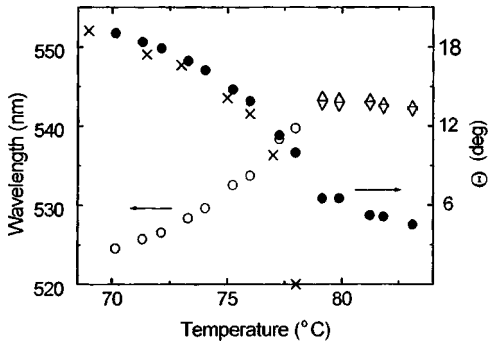

FIG. 5. Temperature dependence of the reflectivity minimum λ_{min} in the electric field applied parallel ($\mathbf{E}_{||}$, upright triangles) and perpendicular ($\mathbf{E}_{\perp}$, inverted triangles) to the direction of the light polarization ($N \simeq 60$). The open circles show averaged data for the reflectivity minimum at the temperature below the bulk transition. The temperature dependence of θ for the film (closed circles, optical reflectivity data) and for the bulk sample ($\times$).

DOBHOP molecules, with a small dipole. Figure 4b shows typical results (three runs) at low temperatures. The time dependence of the reflected intensity is related to a change with time of the tilt plane direction. The orientation in a weak field was not observed for thin films ($N < 20$) both below and above T_c. This kind of behavior correlates with our model.

Let us now consider the results for thick films above the bulk transition temperature (Fig. 3). The wavelength λ_{min} of the reflectivity minimum for the field $\mathbf{E}_{||}$ is larger than λ_{min} for $\mathbf{E}_{\perp}$. The refraction index for the polarization of the light along the tilt plane is larger than the ordinary refraction index n_o (i.e., perpendicular to the tilt plane). From this fact it follows (see Eq. (1), $\lambda_{min} = 2nNd$) that the orientation of the tilt plane and **c**-director are parallel to the electric field.

Figure 5 shows the temperature dependence of λ_{min}. Below T_c the average data for the two light polarizations are shown. To find the tilt angle from the optical spectra one should calculate θ from the positions of the reflectivity minima λ_{min} using Eq. (1) and the known relation[13] between the reflectivity indices and the tilt angle (details are described in Ref. 10). Figure 5 shows also the temperature dependence of θ taken from our x-ray measurements on a bulk sample. Below T_c the magnitude of θ in the bulk sample is slightly smaller, it is indicated also the additional surface ordering in the film.

For thick films, nonzero tilt first appears at the surface for temperatures about 20 °C above the bulk transition temperature.[4,5] When the temperature is only few degrees above T_c the surface layers already exhibit a tilt angle of the order of 20–30° (Refs. 4 and 5). In the temperature range (79–83 °C) the average tilt angle is about 4–6° (see Fig. 5). Since it is clear that the tilt angle has to be very small (practically zero) at the center of the film, the C-like configuration takes place in the electric field.

Let us estimate now the magnitude of the ferroelectric polarization. Note that the change of the tilt angle in our model implies bending of the director **n**. It is well known (see, e.g., Refs. 2 and 14) that in nematics splay and bending deformations of the director field induce a polarization by the so−called flexoelectric effect. In ideal bulk smectics,

deformations leading to the flexoelectric polarizations are strongly suppressed by the layer structures. However, that is not the case in our model, where the tilt angle is not a constant. The dependence of θ on the distance from surface even in the framework of the Landau theory may be quite sophisticated.[15,16] Moreover the spatial variation of θ and of the polarization may result in a space charge and polarization contribution to the elastic constants.[1,17] However in any case the relevant space scale is the bulk correlation length, and the integrated polarization density of the film depends only on the difference between the surface tilt angle θ_s and the tilt angle at the center of the film θ_c. Using the natural estimate for the flexoelectric coefficients $e \simeq 10^{-11}$ C/cm (Ref. 2), $\theta_s = 20°$, and $\theta_c = 0$, we get, using the standard expression for the flexoelectric polarization,[2,14] $P \simeq 0.4 \times 10^{-4}$ C/m^2 for $N = 60$. So this polarization P found for nonchiral free-standing SmC films is fairly large (of the order of spontaneous polarization for chiral smectics).

Thus in our model the ferroelectric polarization is parallel to the tilt plane, whereas for chiral smectics it is perpendicular to this plane. To study the competition of both mechanisms, we investigated the mixture of DOBHOP with chiral component (Looch 15, NIOPIC, 10%). Below T_c, in contrast to pure DOBHOP, free-standing films of the mixture are oriented by a weak field electric field (Fig. 4d) and, as in the case of a classical chiral ferroelectric, the tilt plane is oriented perpendicular to the electric field. However above T_c the tilt plane is oriented parallel to **E** (Fig. 4c). That confirms that for small tilt (recall that $T > T_c$) our mechanism of nonchiral polarization dominates.

The main conclusion we draw is that under appropriate conditions a nonchiral SmC structure displaying ferroelectric properties may exist in free-standing films. The most distinctive feature of this structure is that the polarization is parallel to the tilt plane. The physical mechanism responsible for ferroelectricity of nonchiral smectics is the surface ordering and phase transition leading to spatial variation of the tilt angle.

The research described in this publication was made possible in part by RFFR Grant 98-02-16639, the Russian State Program ''Statistical Physics,'' by Grant 94-4078 from INTAS and from French National Education Ministry. E. K. thanks Prof. M. Vallade (Lab. Spectro. Phys., University J. F., Grenoble-1) for supporting his stay at this Laboratory and Prof. J. Lajzerowicz for fruitful discussions. The Laboratoire de Dynamique et Structure des Materiaux Moleculaires is Unite de Recherche Associee au CNRS No. 801.

[a)]e-mail: dolganov@issp.ac.ru

[1] R. B. Meyer, L. Liebert, L. Strzelecki, and P. Keller, J. Phys. Lett. **36**, L69 (1975).
[2] P. G. de Gennes, *The Physics of Liquid Crystals*, Clarendon Press, Oxford, 1974.
[3] L. M. Blinov, Liq. Cryst. **24**, 143 (1998).
[4] S. Henekamp, R. A. Pelcovits, E. Fontes *et al.*, Phys. Rev. Lett. **52**, 1017 (1984).
[5] S. M. Amador and P. S. Pershan, Phys. Rev. A **41**, 4326 (1990).
[6] Ch. Bahr and D. Fleigner, Phys. Rev. A **46**, 7663 (1992).
[7] T. Stoebe and C. C. Huang, Int. J. Mod. Phys. B **9**, 2285 (1995).
[8] D. Schlauf, Ch. Bahr, and C. C. Huang, Phys. Rev. E **55**, R4885 (1997).
[9] P. O. Andreeva, V. K. Dolganov, and K. P. Meletov, JETP Lett. **66**, 442 (1997).
[10] P. O. Andreeva, V. K. Dolganov, R. Fouret, and C. Gors, Phys. Rev. E (to be published).
[11] T. Stoebe, P. Mach, and C. C. Huang, Phys. Rev. Lett. **73**, 1384 (1994).
[12] E. I. Demikhov, V. V. Dolganov, and K. P. Meletov, Phys. Rev. E **52**, R1285 (1995).
[13] M. Born and E. Wolf, *Principles of Optics*, Pergamon Press, New York, 1964.
[14] R. B. Mayer, Phys. Rev. Lett. **22**, 918 (1969).

[15] M. E. Fisher and P. G. de Gennes, C. R. Acad. Sci. Ser. B **287**, 207 (1978).
[16] K. Binder, in *Phase Transitions and Critical Phenomena*, Vol. 8, edited by. C. Domb and J. L. Leibowitz, Academic Press, London, 1986.
[17] C. Y. Young, R. Pindak, N. A. Clark, and R. B. Meyer, Phys. Rev. Lett. **40**, 773 (1969).

Published in English in the original Russian journal. Edited by Steve Torstveit.

Tunneling resonances in structures with a two-step barrier

Yu. N. Khanin, E. E. Vdovin, Yu. V. Dubrovskiĭ, and K. S. Novoselov
Institute of Microelectronics and Ultrapure Materials Technology, Russian Academy of Sciences, 142432 Chernogolovka, Moscow Region, Russia

T. G. Andersson
Department of Physics, Chalmers University of Technology and Göteborg University, S-412 96 Göteborg, Sweden

(Submitted 5 February 1998; resubmitted 20 April 1998)
Pis'ma Zh. Éksp. Teor. Fiz. **67**, No. 10, 814–819 (25 May 1998)

Electron transport through an asymmetric heterostructure with a two-step barrier $N^+GaAs/N^-GaAs/Al_{0.4}Ga_{0.6}As/Al_{0.03}Ga_{0.97}As/N^-GaAs/N^+GaAs$ was investigated. Features due to resonance tunneling both through a size-quantization level in a triangular quantum well, induced by an external electric field in the region of the bottom step of the barrier ($Al_{0.03}Ga_{0.97}As$ layer), and through virtual levels in two quantum pseudowells of different width are observed in the tunneling current. The virtual levels form above the bottom step or above one of the spacers (N^-GaAs layer) as a result of interference of electrons, in the first case on account of reflection from the $Al_{0.4}Ga_{0.6}As$ barrier and a potential jump at the $Al_{0.03}Ga_{0.97}As/N^-GaAs$ interface and in the second case — from the $Al_{0.4}Ga_{0.6}As$ barrier and the potential gradient at the N^-GaAs/N^+GaAs junction, reflection from which is likewise coherent. © *1998 American Institute of Physics.*
[S0021-3640(98)01910-0]

PACS numbers: 73.40.Kp, 73.20.Dx

Resonance tunneling in systems based on semiconductor heterostructures is of interest because there is a possibility that this physical phenomenon can be used as a tool for investigating a wide spectrum of quantum-mechanical processes and objects. Specifically, resonance tunneling in heterosystems makes it possible to study the energy spectra and nature of the states in quantum objects of different configuration and dimension (from quantum wells to quantum dots). Among works on resonance-tunneling spectroscopy, we call attention to experiments in which so-called virtual states, formed as a result of the interference of electron waves reflecting from a real potential wall on one side and from a potential gradient, having a nonzero reflection coefficient for an electron propagating above it, on the other, were detected. Systems with such a configuration are called quantum pseudowells[1] and, besides the case mentioned, they have been realized in experiments on the observation of above-barrier resonances in wide quantum wells[2] and resonances accompanying tunneling in the Fowler–Nordheim regime.[3] In the latter case

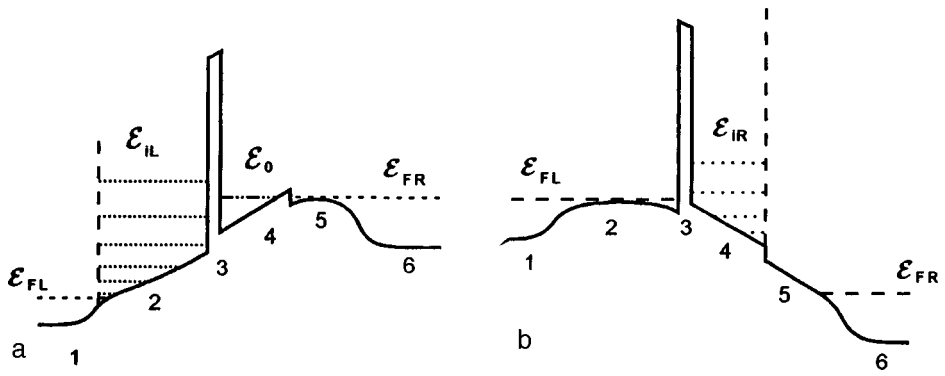

FIG. 1. Schematic band diagram of a heterostructure with a step barrier a) with a negative bias, b) with a positive bias; ϵ_F — Fermi energy in the 3D edges, ϵ_0 — size-quantization level in the electric-field-induced triangular well, ϵ_{iL} and ϵ_{iR} — size-quantization levels in the pseudowells. The numbers 1–6 denote different layers of the structure, as described in the text.

an asymmetric triangular pseudowell is formed above a tunneling barrier when an external electric field is applied to the barrier. The possibility of the formation of a real triangular quantum well in the region of the lower-energy step of a biased two-step potential barrier has been studied theoretically.[4,5] Calculations of the current-voltage characteristics, taking account of resonance tunneling through size-quantization levels in an electric-field-induced quantum well, have been performed for such barriers. As far as we know, electron tunneling through heterostructures with a two-step barrier has thus far not been investigated experimentally. Moreover, it should be noted that biasing a two-step barrier in a direction opposite to that required for the formation of a triangular quantum well should lead to the formation of a trapezoidal quantum pseudowell near the bottom step (see region 4 in Fig. 1b); this was neglected in Refs. 4 and 5. Therefore a system with a two-step potential barrier makes it possible to investigate both states in an induced triangular quantum well and virtual levels in a quantum pseudowell.

In the present work electron tunneling in the asymmetric $GaAs/Al_{0.4}Ga_{0.6}As/Al_{0.03}Ga_{0.97}As/GaAs$ heterostructure with a two-step barrier produced by two $Al_xGa_{1-x}As$ layers with different Al content and spacers (i.e., lightly doped N^-GaAs layers) (Fig. 1) was investigated experimentally. Features were detected in the tunneling current which are due to resonance tunneling through a size-quantization level in an induced triangular quantum well (ϵ_0 in Fig. 1a) and through virtual levels (ϵ_{iL} and ϵ_{iR} in Figs. 1a and 1b, respectively) in two quantum pseudowells of different width, one of which is formed near the bottom step of the barrier, as described above, and the other in the region of the ''long'' spacer on account of reflection from the GaAs N^-/GaAs N^+ interface.[1]

The samples were grown by molecular-beam epitaxy on a highly doped N^+-GaAs substrate and possessed the following sequence of layers: buffer layer – N^+ - GaAs 2×10^{18} cm^{-3} – thickness 500 Å (region 1 in Fig. 1), spacer – 2×10^{16} cm^{-3} N^--GaAs – 500 Å and undoped GaAs – 100 Å (region 2 in Fig. 1), barrier – undoped $Al_{0.4}Ga_{0.6}As$ – 50 Å (region 3 in Fig. 1) and undoped $Al_{0.03}Ga_{0.97}As$ – 300 Å (region 4 in Fig. 1), spacer – 2×10^{16} cm^{-3} N^--GaAs – 300 Å (region 5 in Fig. 1), contact layer –

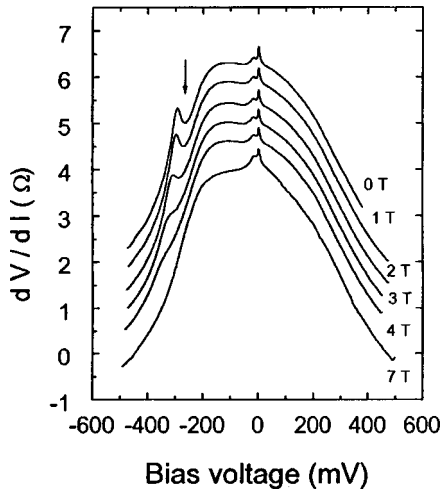

FIG. 2. Differential resistance of the structure versus the bias voltage V in a magnetic field oriented perpendicular to the current: $B \perp J$. The parameter is the magnitude of the magnetic field. The curves for $B > 0$ are shifted arbitrarily downwards in the vertical direction. The arrow marks the position of the resonance.

3×10^{18} cm^{-3} N^+-GaAs – 250 Å (region 6 in Fig. 1). Silicon was used as the dopant. Ohmic contacts were prepared by deposition followed by thermal annealing of the system Ni–Ge–Au. The standard chemical etching technology was used to produce a mesa structure 100 μm in diameter.

The measurements of the curves of the differential resistance dV/dI and the second derivative of the current d^2V/dI^2 versus the bias voltage were performed at a temperature of 4.2 K by a modulation method.

Figure 2 shows the experimental dependence of the differential resistance on the bias voltage and its evolution in a magnetic field oriented perpendicular to the current. The region near zero bias voltage, where a zero anomaly is observed, is not discussed in the present work. In the absence of a magnetic field, a feature (minimum of the resistance), corresponding to resonance tunneling through a size-quantization level in the triangular quantum well formed near the bottom step of the barrier when a negative voltage is applied to it, is observed on this dependence at the voltage $V_b = -260$ mV. The position of this feature is the same as the computed value of the bias voltage for which the energy ϵ_0 of the size-quantization level in the induced triangular well equals the Fermi energy ϵ_F at the right-hand contact (see Fig. 1a). The distribution of the potential along the heterostructure was taken into account in the calculation, the only stipulation being that the electric field in the barrier was assumed to be constant. As one can see in Fig. 2, the application of a magnetic field perpendicular to the current suppresses the minimum of the resistance and shifts it in the direction of high voltages, which should be observed under the conditions of tunneling through a two-dimensional state in a quantum well as a result of a change in the transverse moment transfer of eBl on tunneling on account of the Lorentz force,[6] where l is the effective distance over which the vector potential of the magnetic field acts during tunneling. As was shown in Ref. 7,

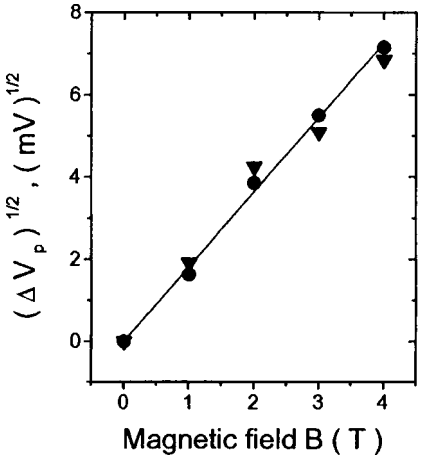

FIG. 3. $(\Delta V_p)^{1/2}$ versus the magnetic field perpendicular to the current, where ΔV_p is the displacement of the position of the minimum of the differential resistance (circles) and minimum of the second voltage derivative of the current $\partial^2 I/\partial V^2$ (triangles) relative to their positions in the absence of a magnetic field.

$$\alpha \Delta V_p = m^* \omega_c^2 l^2 / e,$$

where ΔV_p is the displacement of the position of the resonance in a magnetic field, m^* is the effective mass, $\omega_c = eB/m^*$ is the cyclotron frequency, and the coefficient $\alpha = 0.31$ takes account of the distribution of the voltage drop across the structure.

From the slope of the straight line in Fig. 3 we obtain $l \sim 27.7$ nm, which corresponds to the computed distance from the two-dimensional gas in the accumulation layer near the GaAs/$Al_{0.03}Ga_{0.97}As$ heterointerface to the centroid of the wave function in a triangular well in resonance for $B = 0$. Thus the behavior of the resonance in a magnetic field oriented perpendicular to the current confirms that we are observing resonance tunneling through a level in a triangular well formed above the bottom step of the barrier.

Figure 4 shows the experimental curve of the oscillating component of the second current derivative of the voltage $\Delta(d^2V/dI^2)$ versus the bias voltage in the absence of a magnetic field at $T = 4.2$ K. The ''frequency'' (or average period in the range of bias voltages studied) of these aperiodic oscillations differs significantly in the region of positive and negative bias voltages. We believe that these oscillations are caused by resonance tunneling of electrons through virtual states in quantum pseudowells, formed with a negative voltage of the wall of the top step of the barrier ($N^-Al_{0.4}Ga_{0.6}As$) and a gradient of the potential of the conduction-band bottom in the N^-GaAs/N^+GaAs region (region 2 in Fig. 1a), while with a positive voltage they are formed by the wall of the top step ($Al_{0.4}Ga_{0.6}As/Al_{0.03}Ga_{0.97}As$) and a jump of the potential at the $Al_{0.03}Ga_{0.97}As$/GaAs heterointerface (region 4 in Fig. 1b). The threshold for tunneling through the level ϵ_i in the quantum well is determined by the equality $\epsilon_F = \epsilon_i$ and corresponds to the minimum of the experimental curve d^2V/dI^2.[8] Just as in Ref. 9, we calculated the voltages corresponding to the tunneling threshold for quantum wells with infinite walls 300 Å and 600 Å wide assuming the distribution factor of the voltage on the structure (i.e., the ratio of the voltage drop across the entire structure to the voltage drop across the width of the

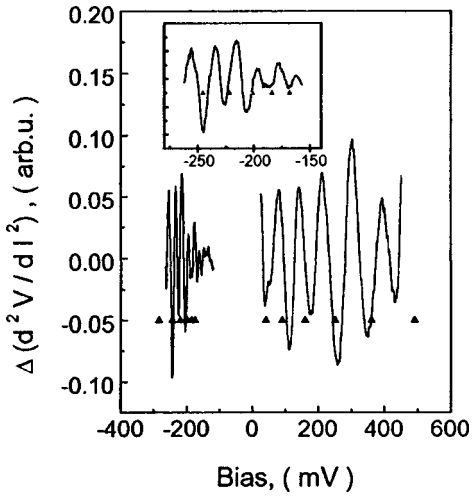

FIG. 4. Second voltage derivative of the current $\partial^2 I/\partial V^2$ minus the monotonic component versus the bias voltage V. The triangles show the computational results for the positions of the tunneling thresholds (see text). Inset: resonances with a negative bias.

quantum well) to be constant, and the results are displayed in Fig. 4. The small discrepancy between the computed and experimentally measured positions of the resonances is explained, first and foremost, by the fact that the distribution factor in the real structure is a function of the bias voltage.

It should be noted that in the analysis of tunneling through a level in a triangular quantum well we compared the computed threshold voltage of tunneling both with the minimum differential resistance and with the minimum of d^2V/dI^2 (see Fig. 3). However, for greater clarity, here we present only the experimental bias voltage dependence of the differential resistance and its evolution in a magnetic field perpendicular to the current.

The contribution of a resonance component to the total current in the case of tunneling through electron states in both quantum pseudowells was equal to $\sim 0.5\%$. The closeness of the amplitudes of the oscillations associated with the reflection from the smooth potential gradient across the N^-GaAs/N^+GaAs interface and from the jump of the potential at the $Al_{0.03}Ga_{0.97}As$/GaAs interface can be explained by the nonuniformity of the bottom step of the barrier and the natural, on account of this, broadening of the corresponding resonances. The magnitude of this effect equals that observed earlier in the study and analysis of tunneling through virtual states in a similar heterostructure with the conventional single (nonstep) barrier.[1] The behavior of the aperiodic oscillations in a magnetic field corresponds to the behavior observed earlier[1,6] and confirms the two-dimensional nature of the states through which tunneling occurs.

It should be noted that in the region of negative bias voltages there are no resonances corresponding to interference states because of reflection from the N^-GaAs/N^+GaAs junction. This can be explained by a natural decrease in the probability of structural interference on the length of the quantum well in the case when its bottom is strongly nonmonotonic (jump of the potential). Estimates showed that the

magnitude of the effect corresponding to these states falls below the limit of sensitivity of our apparatus.

In conclusion, we underscore that the correspondence obtained between the positions of the oscillations of the tunneling current and the computed values of the tunneling thresholds for quantum wells of different width, the magnitude of the effect, and the behavior of the experimental features in a magnetic field enable us to assert that these oscillations are caused by resonance tunneling through virtual states in quantum pseudowells, formed on account of reflection of electrons not only from a sharp potential gradient but also from the smooth N^-GaAs/N^+GaAs junction.

In summary, in the present work we observed a feature corresponding to resonance tunneling through a size-quantization level in a triangular well, formed when a bias voltage is applied above the bottom step of the barrier ($Al_{0.03}Ga_{0.97}As$), and current oscillations as a function of the applied voltage, which are associated with tunneling through virtual levels in pseudowells located to the right and left of the top step of the barrier ($Al_{0.4}Ga_{0.6}As$).

We thank Professor V. A. Tulin and S. V. Morozov for fruitful discussions and interest in this work. This work was supported in part by the State Science and Technology Program ''Physics of Solid-State Nanostructures'' (97-1057), ''Statistical Physics'' (V.3), and ''Surface atomic structures'' (97-3.19), as well as the Russian Fund for Fundamental Research (95-02-06310), INTAS-RFFI (95-0849), and CRDF (RC1-220).

[1] E. E. Vdovin, Yu. V. Dubrovskiĭ, Yu. N. Khanin *et al.*, JETP Lett. **61**, 576 (1995).
[2] A. F. J. Levi, R. J. Spah, and J. H. English, Phys. Rev. B **36**, 9402 (1987).
[3] T. W. Hickmott, Phys. Rev. B **40**, 11683 (1989).
[4] P. A. Shulz and C. E. T. Gonsalves da Silva, Appl. Phys. Lett. **52**, 960 (1988).
[5] M. Di Ventra, G. Papp, C. Coluzza, and A. Baldereschi, *22nd International Conference on the Physics of Semiconductor*, Vancouver, Canada, August 15–19, 1994, p. 1600.
[6] M. Helm, F. M. Peeters, P. England *et al.*, Phys. Rev. B **39**, 3427 (1989).
[7] P. Gueret, C. Rossel, E. Marclay, and H. Meier, J. Appl. Phys. **66**, 278 (1989).
[8] M. Tsuchiya and H. Sakaki, Jpn. J. Appl. Phys. **30**, 1164 (1991).
[9] Yu. V. Dubrovskii, I. A. Larkin, V. V. Vdovin, and Yu. N. Khanin, *23rd International Conference on the Physics of Semiconductor*, Berlin, Germany, July 21–26, 1996, p. 2387.

Translated by M. E. Alferieff

Anharmonicity of Bloch oscillations in GaAs/AlAs superlattices in the case of inhomogeneously broadened excitonic states in a weak electric field

K. L. Litvinenko[a)] and I. Okhrimenko
Institute of Microelectronics Technology and Ultrapure Materials, Russian Academy of Sciences, 142432 Chernogolovka, Moscow Region, Russia

K. Köhler and V. G. Lysenko
Fraunhofer-Institute für Angewandte Fsetkörperphysik, Freiburg, Germany

K. Leo and F. Löser
Institute für Angewandte Photophysik, Technische Universität Dresden, 01062 Dresden, Germany

(Submitted 23 April 1998)
Pis'ma Zh. Éksp. Teor. Fiz. **67**, No. 10, 820–825 (25 May 1998)

The variation of the spectral shape of the four-wave mixing signal in GaAs/AlGaAs superlattices was studied experimentally and theoretically. It was shown that in an external electric field, leading to anticrossing of the levels of heavy and light excitons, sawtooth oscillations of the energy position of the levels are observed. These oscillations are due to the inhomogeneous broadening of the states participating in the Bloch oscillations. © *1998 American Institute of Physics.* [S0021-3640(98)02010-6]

PACS numbers: 71.35.Cc, 78.66.Fd, 42.65.Hw

More than a half century ago Bloch[1] and Zener[2] showed theoretically that an electron in a medium with a spatially periodic potential in a constant electric field F should not be uniformly accelerated but rather it should undergo spatial oscillations near an average position. This occurs because the direction of the quasimomentum of the electron reverses at the edges of the Brillouin zone. The period of such harmonic oscillations, later called Bloch oscillations, equals

$$\tau_B = h/eFd, \tag{1}$$

where h is Planck's constant, e is the electron charge, and d is the period of the potential in the medium where the electron propagates. Bloch oscillations of electrons can be observed only if the phase interruption time of the electrons is much greater than τ_B.[3] In bulk semiconductors the lattice constant d is too small for this condition to be satisfied. However, it has turned out that Bloch oscillations can be observed experimentally in artificial periodic structures — multilayer quantum wells and superlattices (SLs), whose period d equals not several but rather tens or even hundreds of angstroms, while τ_B is much shorter than the phase interruption time. For this, diverse experimental methods have been used.[4–10] The most informative one is the method of spectrally resolved four-

wave mixing (FWM). In Ref. 11 it was shown that for certain directions of bias applied to a SL not only the intensity but also the spectral positions of certain lines oscillate in the FWM spectra because of weak periodic local oscillations of the electric field which are caused by Bloch oscillations of the macroscopic dipole moment. This made it possible not only to determine the period τ_B of Bloch oscillations but also to estimate the amplitude of the spatial oscillations of the electronic wave packet. In strong fields F (>20 keV/cm) damped *harmonic* oscillations of the spectral position of the excitonic lines are observed.[11] However, in a small interval of intermediate and weak electric fields (0.5–2 keV/cm) reproducible sawtooth oscillations with unexpectedly large amplitude at double or triple the frequency are observed.

The anharmonicity of Bloch oscillations in III–V semiconductor SLs is due mainly to the existence of (besides transitions between electronic states and heavy holes) transitions involving the participation of light holes, whose oscillator strength is comparable to that of the heavy excitons. When such SLs are excited by wide-band femtosecond laser radiation, transitions with the participation of both heavy and light excitons can be excited simultaneously. For certain electric fields F the energies of transitions with the participation of heavy and light excitons are equal (for example, $E_0^{hh}-E_0^{hhex}=E_0^{lh}-eFd-E_{-1}^{lhex}$), while their wave functions mix. The oscillator strengths and the differential shift dE/dF of the excitonic lines vary: The intensities of the weak absorption lines (for example, lh_{-1} or lh_{-2}) increase, while the shift of the strong absorption line (for example, hh_0) increases substantially as the electric field varies and moreover the character of the function dE/dF becomes strongly nonlinear, which is what leads to the anharmonicity of the experimentally observed variations in the spectral position of excitonic resonances in FWM signals. The effect due to mixing of the wave functions, called anticrossing of the states of heavy and light excitons, and its influence on the FWM spectra are analyzed in detail in Ref. 12.

To investigate the Bloch oscillations by (nonlinearly) optical methods and to interpret the experimental results, it is important that the quantum-mechanical equivalent of the quasiclassical Bloch representation is a Wannier–Stark (WS) ladder. If a constant electric field F is applied to a semiconductor SL, then the energy states of each electron and hole miniband transform into a ''WS ladder,''[13,14] which is described by the following function:

$$E_l=E_0+leFd; \quad l=0,\pm 1,\pm 2,\ldots, \tag{2}$$

where E_0 is the electron or hole energy in the absence of a field. Optical transitions between a hole localized in one of the quantum wells of the SL and electrons with energies satisfying the relation (2) likewise should be described by the relation (2), where now E_0 is the energy of a transition between an electron and a hole in the same quantum well. In this case a ''fan'' of equidistant levels satisfying Eq. (2) should be observed in the optical spectra. In real semiconductor structures the energy spectrum of the excited states is different from Eq. (2) for many reasons. First and foremost, the Coulomb interaction between photoexcited electrons and holes leads to the formation of bound excitonic states.[15] In the general case the exciton binding energy E_l^{ex} should depend on the parameter l, decreasing as l increases, as a result of which optical transitions become nonequidistant and should be described by a somewhat more complicated relation

$$E_l=E_0+leFd+E_l^{ex}, \quad l=0,\pm 1,\pm 2,\ldots, \tag{3}$$

and instead of one main frequency eFd the Bloch oscillations should be observed at different frequencies of the form $(m-n)eFd+E_m^{ex}-E_n^{ex}$, i.e., the sum oscillation of the electronic wave packet becomes *anharmonic*.

Inhomogeneous broadening of the excitonic lines likewise leads to the existence of a set of slightly different Bloch frequencies, which leads to the appearance of a sum *anharmonic* oscillation of the electronic wave packet. In contrast to homogeneous broadening, which is a consequence of different scattering processes, inhomogeneous broadening is a fluctuation-induced change in the resonance position of an excitonic state. In other words, in the case of inhomogeneous broadening the observed excitonic line consists of a superposition of a set of independent, homogeneously broadened, excitonic lines, whose intensity is determined by the deviation of their resonance position from some average value according to a Gaussian distribution. The factors giving rise to the appearance of inhomogeneous broadening and its influence on the spectrum of excitonic states have been examined in Ref. 16. For us it is important to note that quantum beats of inhomogeneously broadened excitonic lines, which are a more general case of Bloch oscillations, will consist of the interference of quantum beats between different parts of excitonic lines. Therefore in the present letter it will be shown that inhomogeneously broadened excitonic states strongly influence the anharmonicity of Bloch oscillations in the region of anticrossing of the states of light and heavy excitons.

To investigate anharmonic oscillations of the energy position of excitonic lines in the FWM spectra experimentally, we employed GaAs/$Al_{0.3}Ga_{0.7}$As SL samples with 97 and 17 Å wide quantum wells and barriers, built into a p–i–n structure 1 μm thick to which an external bias voltage ranging from $+2$ to -7 V was applied. Radiation with a duration of 150 fs from a tunable titanium-sapphire laser was used in a two-beam arrangement to excite states of heavy and light excitons simultaneously and to observe a spectrally resolved FWM signal. The sample was located in an optical helium cryostat at a temperature of about 10 K. The transmission and FWM spectra with different time delays τ between two laser pulses were detected with an interval of 50 fs with a spectrometer and an OMA multichannel optical detector with a resolution of 0.1 meV.

Figure 1a displays experimentally measured FWM spectra for the experimental superlattice with a bias voltage of -1.7 V for different delays τ ranging from -0.5 to $+2$ ps. The energy of the laser pulse was equal to approximately 1 pJ (which corresponded to electron density $\approx 10^8$ cm^{-2}), and the maximum of the wide-band laser radiation was $h\nu_{las}\approx 1.555$ eV. As one can see from the figure, three states each of heavy and light excitons were excited simultaneously. The intensity of all lines oscillates as a function of τ with period 0.33 ps (Fig. 2a), which corresponds to the splitting between the hh_{-1}, hh_0, and hh_{+1} lines and $eFd\approx 14$ meV. Two quite deep dips between the hh_{-1} and lh_{-2} lines and between the lh_{-1} and hh_{+1} lines are observed in the FWM spectra. The dips cannot be approximated by a sum of Lorentzian or Gaussian lines and are a consequence of the initial phase difference of the wave functions describing heavy and light holes. The experimental dependence of the position of the maximum of the hh_0 line (1.552 eV) line on the delay τ is shown in Fig. 2b (dots). One can see that periodic oscillations are observed, but they are sawtoothed and not sinusoidal.

We calculated the kinetics of the FWM signal spectra by analogy to Refs. 17 and 18. The following conclusions can be drawn from an analysis of the calculations: Quantum beats of homogeneously broadened WS states *from the same* miniband lead to oscilla-

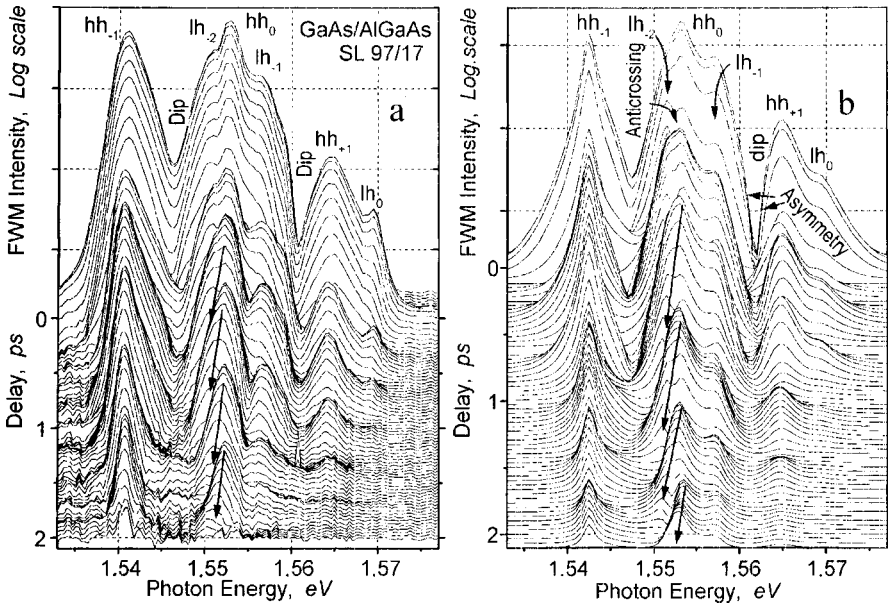

FIG. 1. a) Variation of the shape of the experimental FWM signal spectrum accompanying application of an external constant electric field $F=1.6$ kV/cm. b) Variation of the shape of the FWM signal spectrum obtained using the proposed model for the following parameters: $E_1=1.5425$ eV, $\gamma_1=0.7$ meV, $M_1=1.5$ (hh_{-1}); $E_2=1.553$ eV, $\gamma_2=1.1$ meV, $M_2=1.2$ (hh_0); $E_3=1.5575$ eV, $\gamma_3=1.4$ meV, $M_3=0.7\cdot i$ (lh_{-1}); $E_4=1.5645$ eV, $\gamma_4=1.8$ meV, $M_4=1$ (hh_{+1}); $E_5=1.56$ eV, $\gamma_5=1.8$ eV, $M_5=0.3$ (lh_0); $M_6=1.5515$ eV, $\gamma_6=0.9$ meV, $M_6=1.35\exp(\pi/6\cdot i)(lh_{-2})$, where E_i, γ_i, and M_i are, respectively, the resonance position, homogeneous broadening parameter, and dipole moment of the ith excitonic transition.

tions of only the intensity of the FWM signal with the same period for all lines. The shape of the FWM signal spectrum is absolutely independent of the delay τ. Simultaneous laser excitation of homogeneously broadened states of heavy and light holes with negative indices (for example, lh_{-1} or lh_{-2}) leads to interference of the polarizations of these states. As a result, additional *harmonic* oscillations of the spectral position and shape of the FWM lines are superposed on the harmonic oscillations of the intensity and shape of the FWM signal which are caused by the Bloch spatial oscillations of the macroscopic dipole moment. However, for reasonable values of the oscillator strengths and dampings of the light-exciton states the oscillations of the spectral position of the FWM lines do not exceed 0.2 meV. The most complete agreement between the theoretical calculations of the shape and kinetics of the FWM signal spectrum and the experimental observations obtains in the case of quantum beats of inhomogeneously broadened excitonic lines. Even quantum beats of only two inhomogeneously broadened levels can lead to sawtooth oscillations of the resonance position of the excitonic states. In addition, the sawtooth character of the spectral oscillations depends on the correlation parameter λ, which shows the extent to which the distributions describing inhomogeneous broadening of interacting excitonic states are coupled with one another.[18] In the case of total correlation ($\lambda=1$) these distributions can be uniquely expressed in terms of one another. The result is that the effects of the interference of the polarization of different parts of the excitonic lines compensate one another completely and in consequence oscillations of the

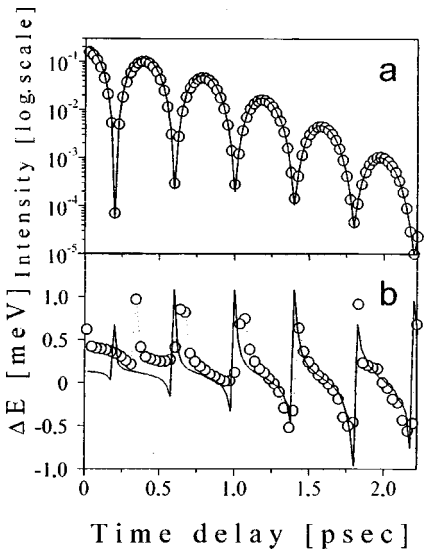

FIG. 2. Comparison of the experimental (circles) behavior of the maximum (a) and resonance position (b) of the hh_0 line with theoretical calculations. The best agreement is shown in the figure by solid lines and is obtained for the following values of the parameters: $E_1=1.541778$ eV, $\gamma_1=0.52$ meV, $\Gamma_1=3\gamma_1$; $E_2=1.552114$ eV, $\gamma_2=0.74$ meV, $\Gamma_2=\Gamma_1$, $\lambda=0.72$, where Γ_i is the inhomogeneous-broadening parameter.

position or shape of the FWM lines are not observed. In the case when the factors giving rise to inhomogeneous broadening are completely independent of one another ($\lambda=0$), the interference of polarization has a large effect. In real SLs the parameter λ varies from 0.6 to 0.9, so that anharmonic variations of the position of the excitonic lines can be observed experimentally. The intensity of the anharmonic spectral oscillations caused by quantum beats of inhomogeneously broadened levels depends on the splitting between the levels and decreases rapidly with increasing splitting of the fan of states of the SW ladder.

Figures 2a and 2b show the experimentally measured oscillations (dots) of the intensity and spectral position of the hh_0 line with a bias voltage of -1.6 V and the computational results (solid lines) obtained for the case of quantum beats of inhomogeneously broadened levels hh_0 and hh_{-1} (the parameters employed in the calculations are indicated in the figure caption). The good agreement between the theoretical and experimental variations in the position of the hh_0 line confirms the correctness of choosing Bloch oscillations of the macroscopic dipole, taking account of inhomogeneous broadening, as a theoretical model. The change in the resonance position of the line studied is different from the theoretical predictions only for small delays. This is due to the fact that the theoretical model employed neglected completely the effect of the finite duration of the exciting laser pulse as well as other states of light and heavy excitons which result in additional anharmonicity of the oscillations of the FWM signal.

Figure 1b shows the FWM signal spectra computed on the basis of the proposed model for resonance energies, relative amplitudes, and decay parameters of the states of heavy and light excitons, presented in the figure caption, which participate in the Bloch oscillations. As follows from a comparison of the experimental (Fig. 1a) and theoretical

(Fig. 1b) spectra and the kinetics of the FWM signal, they agree not only in overall features, but also in many details.

In summary, we have shown that quantum beats of inhomogeneously broadened states of heavy excitons in GaAs/AlGaAs superlattices in a weak external electric field lead to anharmonicity of Bloch oscillations. The model proposed makes it possible to describe quite completely the FWM signal spectra and the kinetics of Bloch oscillations in weak fields and to determine the parameters characterizing them.

This work was supported by the Russian Fund for Fundamental Research (97-02-16833), the State Committee on Science and Technology (97-1058), and INTAS (94-324 and 95-0576).

[a)]e-mail: kostja@ipmt-hpm.ac.ru

---

[1] F. Bloch, Z. Phys. **52**, 555 (1928).
[2] C. Zener, Proc. R. Soc. London, Ser. A **145**, 523 (1932).
[3] N. W. Ashcroft and N. D. Mermin, *Solid State Physics*, Holt-Saunder Int. Ed., Philadelphia, 1981.
[4] J. Feldmann *et al.*, Phys. Rev. B **46**, 7252 (1992).
[5] K. Leo *et al.*, Solid State Commun. **84**, 943 (1992).
[6] P. Leisvhing *et al.*, Phys. Rev. B **50**, 14389 (1994).
[7] R. Martini *et al.*, Phys. Rev. B **54**, R14325 (1996).
[8] T. Dekorsy *et al.*, Phys. Rev. B **50**, 8106 (1994).
[9] K. Unterrainer *et al.*, Phys. Rev. Lett. **76**, 2973 (1996).
[10] M. Ben Dahan *et al.*, Phys. Rev. Lett. **76**, 4508 (1996).
[11] V. G. Lyssenko, G. Valusis, F. Loser *et al.*, Phys. Rev. Lett. **79**, 301 (1997).
[12] F. Loser, M. Sudzius, V. Lyssenko *et al.*, Phys. Status Solidi B **206**, 445 (1998).
[13] E. E. Mendez, F. Agullo-Rueda, and J. M. Hong, Phys. Rev. Lett. **60**, 2426 (1988).
[14] P. Voisin *et al.*, Phys. Rev. Lett. **61**, 1639 (1988).
[15] M. M. Digman and J. E. Sipe, Phys. Rev. Lett. **64**, 1797 (1990).
[16] K.L. Litvinenko, A. Gorshunov, V. I. Grinev *et al.*, Zh. Éksp. Teor. Fiz. **109**(2), 665 (1996) [JETP **82**, 356 (1996)].
[17] T. Yajima and Y. Taira, J. Phys. Soc. Jpn. **47**, 1620 (1979).
[18] J. Erland *et al.*, Phys. Rev. B **50**, 15047 (1994).

Translated by M. E. Alferieff